On the Nucleation, Evolution and Overgrowth of InAs/GaAs(001) Quantum Dots

Über Nukleation, Entwicklung und Überwachsen der InAs/GaAs(001) Quantum Punkte

Dissertation zur Erlangung des akademischen Grades
des Doktors der Naturwissenschaften (Dr. rer. nat.)
an der Universität Konstanz
Fachbereich Physik

vorgelegt von

Paola Alejandra Acosta-Díaz

Dissertation der Universität Konstanz
Tag der mündlichen Prüfung: 16 Juli 2008
Referenten: Prof. Dr. Klaus Kern
Prof. Dr. Günter Schatz

Zusammenfassung

Die vorliegende Arbeit behandelt die mikroskopischen Mechanismen der Keimbildung, des Wachstums und des Überwachsens von selbstorganisierten Quantenpunkten auf Halbleiteroberflächen.

Ausgelöst durch Verspannungen beim Wachstum von Materialien mit Gitterfehlpassung bilden sich spontan Inseln im Grössenbereich von Nanometern. Bedingt durch die vollständige Quantisierung der elektronischen Zustände auf dieser Längenskala, ergibt sich eine Vielzahl von Anwendungsmöglichkeiten im Bereich der Optoelektronik, etwa in Halbleiterlasern, Quantencomputern oder in Einzelelektronen-Bauelementen.

Um die fundamentalen Prozesse der Heteroepitaxie und ihren Einfluss auf die Eigenschaften der Quantenpunkte zu untersuchen wurde die Morphologie von selbstorganisierten InAs/GaAs (001) Quantenpunkten systematisch studiert. Quantenpunkte, die sich in diesem System nah am thermodynamischen Gleichgewicht bilden sind der Ausgangspunkt der Untersuchungen. Rastertunnelmikroskopie wurde verwendet um den Ausgangspunkt der Keimbildung von Quantenpunkten mit hoher atomarer Auflösung zu untersuchen. Die Bildung von kleinen Clustern auf einer verspannten Benetzungschicht ist der Ausgangspunkt des Wachstums. Mit zunehmender Grosse kann eine teilweise Facettierung der Inseln beobachtet werden, bis schliessich pyramidenförmige Inseln mit vier vollständigen $\{137\}$ Facetten beobachtet werden können.

Weitere Stadien des Wachstums sind charakterisiert durch die morphologische Transformation in vielfach facettierte Inseln, sogenannte Kuppeln. Die thermodynamische Stabilität dieser Inseln wurde unter Hinzunahme von theoretischen Betrachtungen untersucht. Die beobachtete Koexistenz verschiedener Formen kann damit als struktureller Phasenübergang interpretiert werden, wobei das chemische Potential eine Diskontinuität aufweist.

Um letztlich eine räumliche Einschränkung der Wellenfunktion und damit die Quantisierung der elektronischen Zustände zu erreichen, müssen die Inseln mit ein Material mit GröSSerer Bandlücke Überwachsen werden. Eine drastische Änderung der Form wie auch der Höhe ist nach diesem Prozess zu beobachten. Zwei Regimes, abhängig von der Dicke der überwachsenen Schicht, konnten identifiziert werden. Im ersten Fall, in dem eine wesentlich Höhenänderung beobachtet werden kann, ändert sich die form der Inseln, was als umgekehrte Pyramiden-Kuppel Transformation beschrieben werden kann. Vollständiges Überwachsen kann im zweiten

Regime beobachtet werden. Die Beobachteten Strukturen werden hier als Funktion der Wachstumsrate diskutiert.

Table of Contents

Abbreviations and Common Symbols

STM	Scanning Tunneling Microscope
QDs	Quantum Dots
$1D/2D/3D$	One/ Two/ Three Dimensions
λ	de Broglie wavelength
m_{eff}	Effective mass
h	Planck's constant
DOS	Density of States
θ_c	Critical thickness
SK	Stranski-Krastanow
RT	Room Temperature
HR	High Resolution
MBE	Molecular Beam Epitaxy
LT	Low Temperature
STS	Scanning Tunneling Spectroscopy
TEM	Transmission Electron Microscope
V_B	Bias Voltage
I	Tunneling current
d	Tip-sample separation distance
T	Transmission probability
ϕ	Work function
$H_{L/R}$	Left/Right Electrode hamiltonian
H_T	Transfer hamiltonian
$\psi_{L/R}$	Left/Right Electrode wavefunction
M_{LR}	Tunneling Matrix Element
$f(E)$	Fermi distribution function
ρ	Density of states
TH	Tersoff and Hamann
$LDOS$	Local Density of States
WKB	Wentzel-Kramers-Brillouin

j	Current density
$N(E_z)$	Normal energy distribution
dI/dV	Differential conductance
AFM	Atomic Force Microscopy
SPM	Scanning Probe Microscope
UHV	Ultra-High Vacuum
$RHEED$	Reflected High Energy Electron Beam
BEP	Beam Equivalent Pressure
HF	Hydrofluoric acid
SEM	Scanning Electron Microscope
$FvdM$	Frank-van der Merwe
VW	Volmer-Weber
γ	Surface energy
ε	Strain
r_c	Critical Radius
XPS	X-ray Photoemission Spectroscopy
XRD	X-ray Difraction
WL	Wetting Layer
θ_c	Critical coverage
RAS	Reflectance Anisotropy Spectroscopy
ECR	Electron Counting Rule
DFT	Density Functional Theory
FP	Facet Plot
LSS	Local Surface Slope
SET	Single Electron Transistor
a	Lattice constant
μ	Chemical potential
kMC	Kinetic Monte Carlo

Chapter 1

Introduction

Since the beginning of history, men astonished by the captivating spell of Nature, have tried to understand what he sees. Through observation, scientific fields like astronomy were developed, and with it the advent of complex sciences as mathematics and physics (where logic and reasoning is required) took place. Aware of the power of Nature, men did not limit to be a passive member of his surroundings, and within his eternal quest of dominance, he started making use of the acquired knowledge for practical purposes, opening the gate towards machines. Inasmuch, the fabrication of new and better instrumentation, such as the telescope used by Galileo Galilei in 1609, was the preamble of a change of paradigm that ended with the scientific revolution of the 16th century and Newton's mechanics.

At the dawn of the 20th century, discrepancies between experimental observations and the existing theory, gave birth to Quantum mechanics. Men's capability of changing his environment, enriched not only with the study of celestial bodies of gigantic proportions, but also, with the study of minuscule ones: the atoms (Fig. 1.1). Now more than ever, we know that „small is different “.

Quantum Mechanics, Many Body Theory or Particle Physics have posed many questions whose answers are far from our understanding. There is more than meet the eye.

The telescopes of former times have evolved into microscopes. Some of the most powerful tools of our time is the Scanning Tunneling Microscope (STM). The working principle of the STM is quantum in its nature and among its outstanding achievements lies the individual manipulation of atoms. The ability to design complex devices on ever–smaller scale is now revolutionizing established fields like medicine diagnostics [1], drug delivery [2], electronics or structural materials [3], arising new fields such as quantum information processing [4] and nanobiotechnology [5, 6]. Working at the nanometer length scale (< 100 nm) implies to deal with new size–dependent properties (Fig. 1.2), that provide a great toolbox to bridge fundamental science with a wide variety of every day applications.

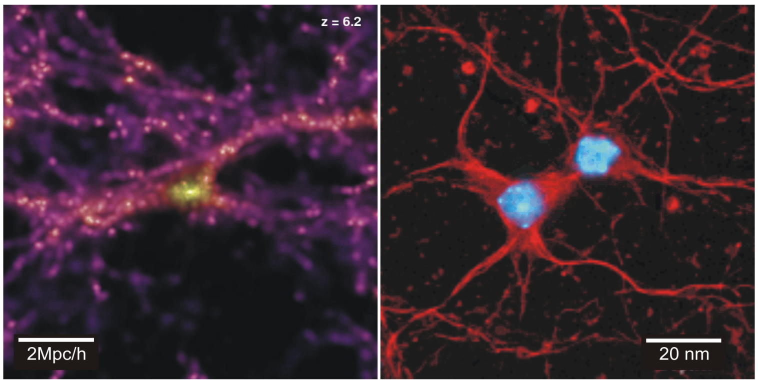

Fig. 1.1: Same universe different scales. On the left, a snapshot of a simulation of the formation, evolution and clustering of galaxies and quasars. Image taken from [7]. On the right fluorescence image of nerve cells in primaryculture labeled with biotinylated nanocrystals. Image taken from [8]

Nonetheless, no matter how far man's acumen can reach or how sophisticated our tools and methods become, Nature's wit can not be surpassed. Self–assembly stands as the most effective route to create nanostructures, not only size–wise but cost–wise as well. Among the most studied offsprings of self–assembly are semiconductor Quantum Dots (QDs), commonly known as self–organized QDs.

Quantum Dots refer to nanometer–sized structures (10^3–10^5 atoms) characterized by a relative small number of electrons and holes confined in all three dimensions (3D). Quantization effects arise in a structure when its dimension becomes comparable to its de Broglie wavelength λ, which depends on the temperature and in the effective mass m_{eff} of the carrier as

$$\lambda = \frac{h}{p} = \frac{h}{\sqrt{3m_{eff}K_BT}} \tag{1.1}$$

where h is Planck's constant, p correspond to the carrier momentum and K_B is Boltzman's constant. For semiconductors, the effective mass is such ($\sim$ 0.01–0.1 m_o) that confinement effects start to appear for structures down to nanometers, like those produced by self–assembly.

Three–dimensional confinement breaks up the energy bands of the host material into a set of discrete levels, narrowing drastically the density of states (DOS). For this resemblance with the atomic spectra, QDs are often dubbed as „artificial atoms “.

Semiconductor QDs can be produced by different techniques, namely by colloidal chemistry [10], by lithographic patterning [11], by size fluctuations in conventional quantum wells [12], or by the epitaxial growth of lattice-mismatched materials [13].

Although colloidal QDs have proven their worth by in-vivo cellular imaging, thanks to their easy chemical manipulation after synthesis [14, 15] (Fig. 1.1), in nanotechnology, self–organized QDs are a cornerstone due to their excellent optical properties, particulary their high

Fig. 1.2: CdSe nanocrystals emitting at different wavelengths as an example of the size-effect phenomena observed in QDs [9].

radiative efficiency, large confinement energies and large energy separation, essential features for many optoelectronic devices (QD laser, far infra–red detectors, single–photon emitters, etc. [16, 13, 17]) and the potential use in quantum computing [4]. Compared to the electrostatically defined QDs or the quantum–well dots, self–organized QDs exhibit larger confinement and offer the possibility to tune their response by band structure engineering. Therefore, self–organization is the most prominent growth method for semiconductors QDs.

Self–organized QDs are spontaneously formed under vacuum growth conditions as a consequence of the lattice mismatch between the deposited material and the underlying substrate. The formation of 3D islands is driven by the strain field induced by the deposition of a few monolayers of a highly strained material on the substrate (wetting layer). Once the deposited layer exceeds a critical layer thickness (θ_c), a transition from a 2D to a 3D growth is prompted as a means to relax strain. This process is known as islanding or Stranski–Krastanow (SK) growth.

The overgrowth of the resulting 3D islands by a larger band gap material (usually the same used as the substrate) leads to coherent inclusions in a semiconductor matrix, with quasi–zero dimensional electronic properties persisting up to room temperature (RT) and that are less sensitive to the environment. It is noteworthy to underline that just as–grown islands or 3D islands should not be confused with capped islands refer hereinafter as QDs.

SK growth allows the realization of semiconductor QDs of excellent structural quality with an atomically continuous interface, since the overgrowth of the defect–free 3D islands eliminates the existence of interface states or surface defects, enhancing coherent charge transport and high recombination efficiency.

This growth method applies for systems with lattice mismatched $\geq 2\%$, enabling the combination of numerous semiconductor materials, such as Ge/Si, InAs/GaAs, InP/GaAs, CdSe/ZnSe, etc. [13] The foremost studied and applied systems are Ge/Si(001), for its compatibility with all the Si–based technology and InAs/GaAs(001), for its optoelectronic capabilities.

InAs/GaAs(001) QDs offer the advantage that both materials are direct band gap semiconductors, confining both electron and holes alike. Another advantage is the possibility of „wavefunction engineering “. At room temperature, InAs/GaAs(001) QDs generally emit in the 1.05–1.18 μm range, but by modulation of the growth conditions, the emission wavelength can be driven towards the 1.3 μm range, close to the silica fiber optic communication wavelength [18].

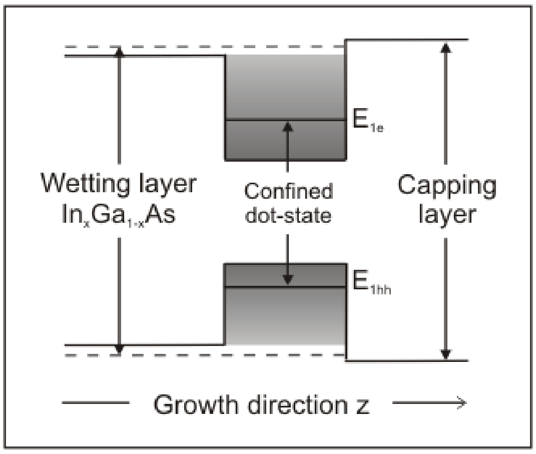

Fig. 1.3: Schematic band diagram of a confined dot–state surrounded by the wetting layer quantum well and the capping layer.

In a very simplified manner, the QDs confinement potential can be thought of as a particle in a box. In this case, the barriers of the confining potential will be given on one side by the band gap energy of the wetting layer and, on the other side, by the band gap of the capping layer, as represented schematically in Fig. 1.3. The characteristics of the electronic properties of electrons and holes depend on the QDs confining potential. The confining potential depth is related with the QD composition, since any incorporation of Ga in the deposited InAs layer modifies the band gap energy, and therefore the band offsets, according to Vegard's law [19]. The confining potential also varies according to size, thus, the QDs atomic–like properties can be fully exploited by changes in their geometry (size and shape), composition and strain.

Additionally, when decreasing the energy of the band gap of the capping layer, for instance by using $In_xGa_{1-x}As$ instead of GaAs, the band offsets are reduced and the recombination energy is shifted to lower energies with respect to that of GaAs/InAs/GaAs structures. This may as well, affect the strain distribution within the dot, since the lattice constant and thus the mismatch is also regulated by modulating the $In_xGa_{1-x}As$ stoichiometry. Furthermore, the composition of the wetting layer and of the QDs depend on factors such as the deposition flux rate, the growth temperature, the As back pressure during growth, etc.

Intense research made over more than fifteen years has produced great advances in the engineering of QDs and QDs arrays [20]. Some applications such as Fabry-Perot Diode Lasers and Optical amplifiers working at 1.3 μm wavelength are about to be commercially available (QD Laser Inc.), and many other application patents are awaiting for commercialization [21].

However, the achievements in this field are a result of observation and experimentation, not merely of intention. There is still much to be done in the understanding of the atomistic mechanism governing the nucleation, evolution and overgrowth of self-organized QDs, in order to have control of the geometrical and compositional characteristics of the resulting nanostructure, and thus to manipulate its electronic spectra at will.

Such degree of control requires a deeper comprehension of the influence of the growth parameters and the role of the different atomistic process at play during the self–organization process.

In the present work, high resolution STM (HR-STM) has been used to investigate the morphology of InAs nanostructures grown by Molecular Beam Epitaxy (MBE), close to the thermodynamic equilibrium regime. A thorough characterization of the structures at the nanometer scale was performed, with the aim to decode the relation between the observed features, the underlaying growth mechanisms and to certain extent to their dependance on the growth conditions.

The output of this investigation is presented in the next five chapters and it is organized as follows:

Chapter 2 contains a summary of the experimental employed techniques, the corresponding underlying theory and the experimental set up. A description of the sample preparation is also included.

In Chapter 3 an overview of the growth modes observed for thin film growth is given, with particular interest in the InAs/GaAs(001) system. The role of strain and intermixing in the morphological evolution at the 2D to 3D transition is discussed. High resolution STM images of the early stages of dot nucleation revealed the formation of very small precursors and partially faceted islands before the onset of well–defined equilibrium shaped islands. The effect of In segregation and the wetting layer structure in the 2D to 3D transition is reviewed.

The posterior structural phase transition that small islands undergo when evolving into bigger and multifaceted islands is presented in Chapter 4. STM images in combination with calculations of the thermodynamical stability of the islands provide a microscopic description of the evolution of islands, reaching out towards the understanding of one of the fundamental process of island growth, the anomalous observed ripening.

Chapter 5 is devoted to the effects of the mandatory overgrowth process of the as–grown islands. Two capping regimes are identified as a function of the capping layer thickness. A reverse phase transition is observed for the first regime, resembling thermodynamic equilibrium shapes observed during growth. A true overgrowth occurs during the second regime. The influence of kinetics on the morphological changes of the capped islands is revised.

Based on the experimental results obtained in the course of this investigation, it was possible to formulate a unified morphological picture of the self–organized 3D islands, before and after the transformation by capping of the QDs.

Chapter 6 displays some preliminary results of low–temperature scanning tunneling spectroscopy (LT–STS) studies performed to the as–grown islands with the intention of realize a systematic characterization of the electronic nature of the confined dot states. As well, some initial results of etching experiments are included. These experiments are intended as a means of revealing the compositional profiles of buried islands, as a complementary study of the self–organized QDs characteristics.

Chapter 2

Experimental Methods

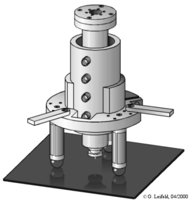

2.1 Scanning Probe Microscopy

No doubt, the Scanning Tunneling Microscope (STM) has become an essential tool for scientists to disclose phenomena from a nanoscopic standpoint. Its working principle is not only very simple, but it is a plain example of the quantum properties of matter. Ever since the birth of quantum theory, tunneling has been regarded as a fascinating classically forbidden effect, that merely relies on the wave nature of electrons.

In 1931, Ernst Ruska and Max Knoll built the first Transmission Electron Microscope (TEM) [22] leading the development of electron microscopies. The use of high–energy electrons beams came up as an alternative to the limitation in magnification of light for microscopy.

Separately, the idea of obtaining microscopical information by scanning a sharp probe at close distance across a sample, was introduced by Synge [23] in 1928 and by O'Keefe in 1956 [24] in order to study near–field effects. But it was not until 1972, that Young managed to combine the resolution capability of electron microscopies with the advantage of a scanning probe [25]. In the Topografiner, piezoelectric actuators where used for sweeping and positioning a metal tip above a sample's surface. By applying a voltage between tip and sample, Young used the field emission signal to control the tip–sample separation, achieving in this way a resolution of 4000 Å laterally and 30 Å vertically. The Topografiner set in the basic principles of the STM and opened the door to one of the most valuable surface science tools.

In the late 70s, Gerd Binning and Heinrich Rohrer aimed for a better understanding of the effect of local inhomogeneities of the surfaces involved in tunneling spectroscopy. Moreover, they realized that in order to have access to a metal–vacuum–metal tunnel junction, which allowed systematic investigation of its properties, a new approach was needed. They turned to vacuum tunneling. Their approach was a microscope, similar to the Topografiner, but instead of using field emission current, they measured current from tunneling.

In 1983, the first paper showing an atomically resolved image of the (7x7) reconstruction of the Si(111) surface was published [26]. For their invention, Binning and Rohrer merited the 1986 Nobel prize in Physics. The prize was shared with Ernst Ruska for his contribution to Electron Microscopy [27].

2.2 Basic Principles of Tunneling

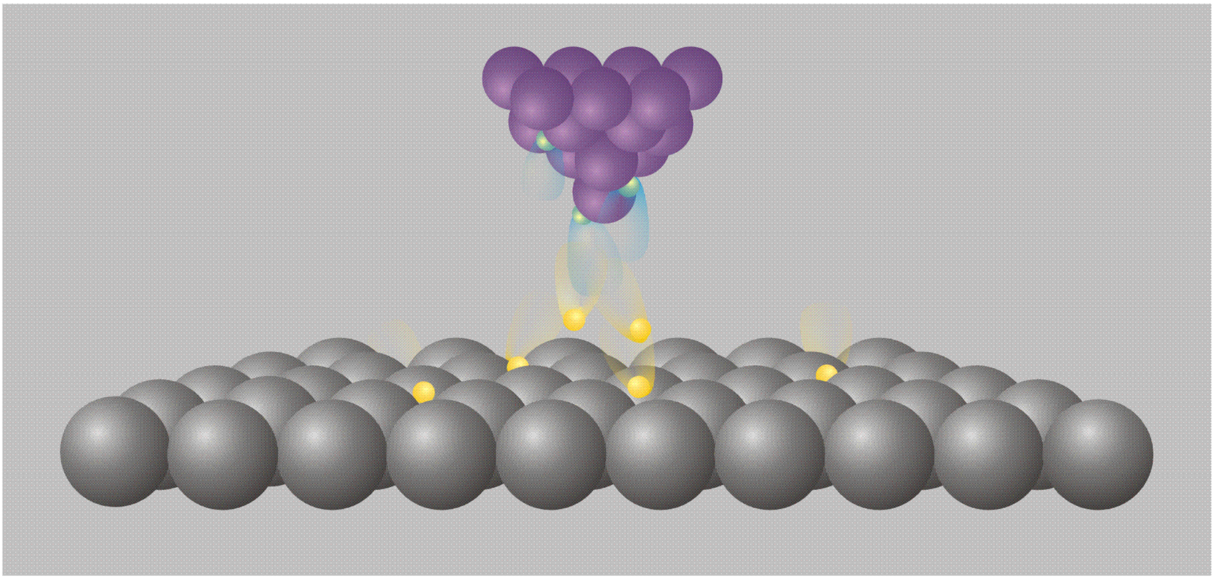

Fig. 2.1: Schematic representation of the tip and sample wavefunction overlap.

The underlying principle of STM relies on the ability of electrons to tunnel beyond the surface boundary. If a sharp metallic tip is approached to the surface of a conductive sample, close enough for the wavefunction of the tip and the sample to start overlapping ($\sim$ 5–10 Å), electron tunneling is produced.

The electron transfer will occur from the electrode with higher Fermi energy to the one with lower Fermi energy, similarly to the case of two metals brought into contact [28]. This electron transfer creates an excess of positive charge in one metal and an excess of negative charge in the other, generating an electric field. The electric field provides with potential energy to the electrons in the metal with lower Fermi energy, leading to an alignment of the Fermi levels and hence stoping further electron transfer. If additionally an external potential difference (bias voltage) is applied between the tip and the sample, the Fermi energy levels will be shifted accordingly generating a steady tunneling current (Fig. 2.2). The tunneling current (I), together with the bias voltage (V_B) constitute the fundamental parameters when working with STM.

The tunneling current depends strongly on the tip–sample separation distance, since it is directly related to the tunneling probability. From quantum mechanics it is known that a particle with mass m and energy E, moving across a square potential barrier of height V_B and width d,

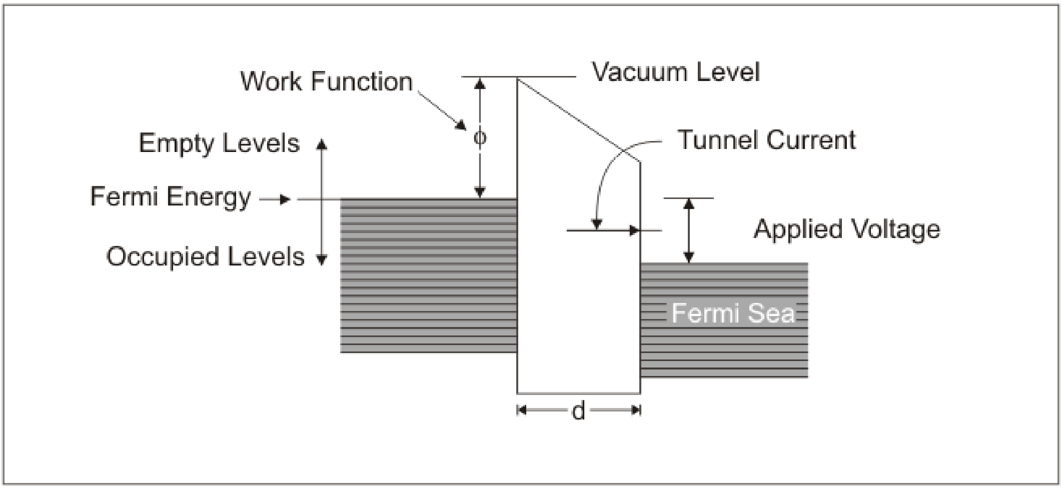

Fig. 2.2: Schematic representation of the potential barrier for tunneling of an arrangement of two metals separated by a thin vacuum region.

has a finite probability to tunnel when E <V_B [29]. The transmission probability T in this case is equal to

$$T = [1 + \frac{V_B^2}{4E(V_B - E)} \sinh^2(\frac{d}{\hbar}\sqrt{2m(V_B - E)})]^{-1} \tag{2.1}$$

In the special case when E ≪V_B, the transmission probability can be rewritten as

$$T = [\frac{16E}{V_B}(1 - \frac{E}{V_B})e^{-2\frac{d}{\hbar}\sqrt{2m(V_B - E)}}] \tag{2.2}$$

For electronic states at the Fermi level, the surface represents a potential barrier whose height is equal to the work function ϕ. In the case of vacuum tunneling, the potential in the vacuum region acts as a barrier to electrons between the tip and the metal sample. The width of this barrier is given by the tip–sample separation distance *d*. In the most simple case, the work function of the tip and the sample can be considered to be comparable. Thus, for states at the Fermi level, (V_B- E) will be just the work function ϕ.

From this simple 1D model it can be seen that the transmission probability and hence, the tunneling current, decays exponentially with the separation distance *d* as

$$I \, \alpha \, e^{-2\sqrt{\frac{2m\phi}{\hbar^2}}d} \tag{2.3}$$

It is precisely this dependance on the distance that makes STM a highly sensitive technique. Taking into account that for metals surfaces work function values are around 4 eV, Eq. 2.3 tells us that if the separation separation distance *d* is increased by 1 Å, the value of the tunneling current decreases by an order of magnitude. Nowadays, a vertical resolution of 2 pm has been achieved with STM at low temperatures.

A schematic representation of a STM is depicted in Fig. 2.3. Two modes of operation are possible while working with STM: the constant current mode and the constant height mode.

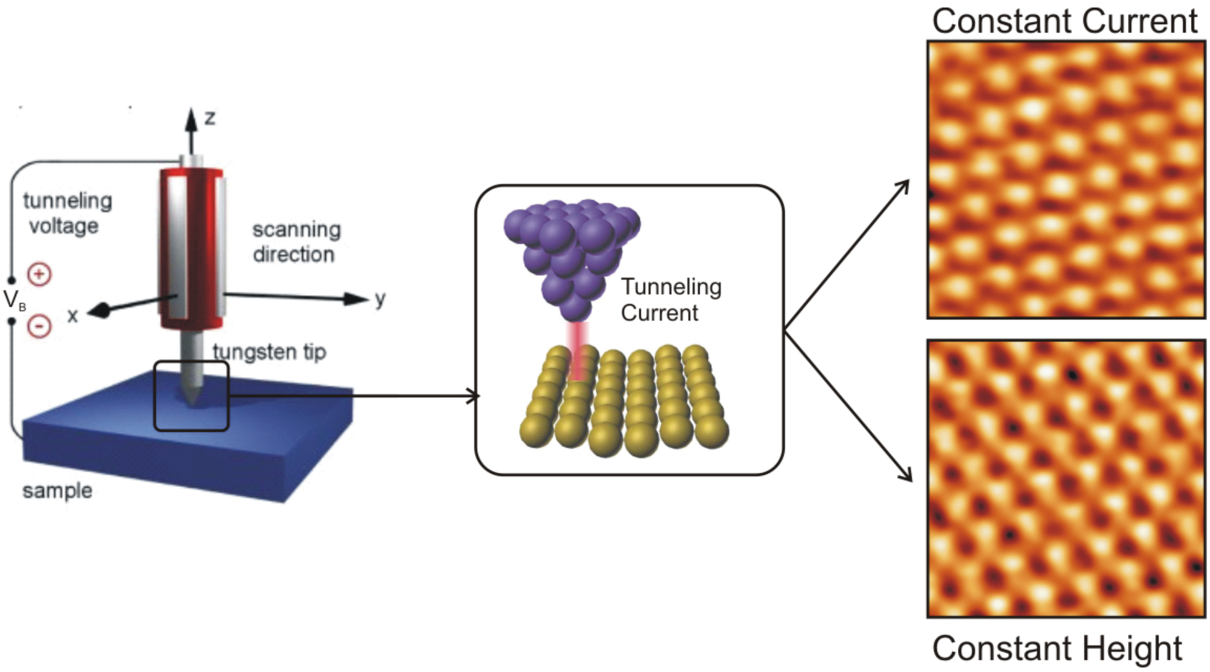

Fig. 2.3: Schematic diagram of a STM head. On the right: STM images of graphite at constant current (above) and at constant height (below). The images size is 1.5 nm x 1.5 nm. Images taken from [30].

In the constant current mode, the tip is raster–scanned across the sample surface, while keeping the value of the tunneling current constant. The tunneling current is monitored for every single image point and is kept constant by adjusting the separation distance by means of piezoelectric actuators. The voltage needed for controlling the piezoelectric actuators are generated by a feedback system and recorder as a function of the in–plane tip position. Because of the linearity of the piezos, these voltages can be used to trace the surface topography.

In the constant height mode, the absolute vertical separation between tip and sample remains constant, and changes in the tunneling current are recorded. This mode offers the advantage of high scan rates in order to minimize distortions by, e.g., thermal drifts, since a feedback controller is not required. However, this mode is only useful for extremely flat surfaces, where the risk of tip–sample crashes is low. All the images presented in this work, were acquired in constant current mode.

Besides resolution, two of the biggest merits of STM are that: a) the recorded tunneling current signal provides local information about the surface and b) the topological information can be obtained in real space. Albeit the tunneling current depends on both the geometry and the electronic structure of the tip and sample surfaces [31]. Determination of the contributions of electronic structure versus topographical features is necessary for the correct interpretation of STM images. A realistic depiction requires more accurate approximations for describing the tunneling process.

2.2.1 Electron tunneling models

Independent electrode approximation

The starting point for many of the theoretical approaches for studying the tunneling process is the time–dependent perturbation theory developed by Bardeen [32].

Instead of introducing states which are the exact solutions of an approximate Hamiltonian, Bardeen introduced approximate solutions of the exact Hamiltonian. Starting with two subsystems, he calculated the tunneling current through the overlap of the wavefunctions of the unperturbed systems using Fermi's golden rule.

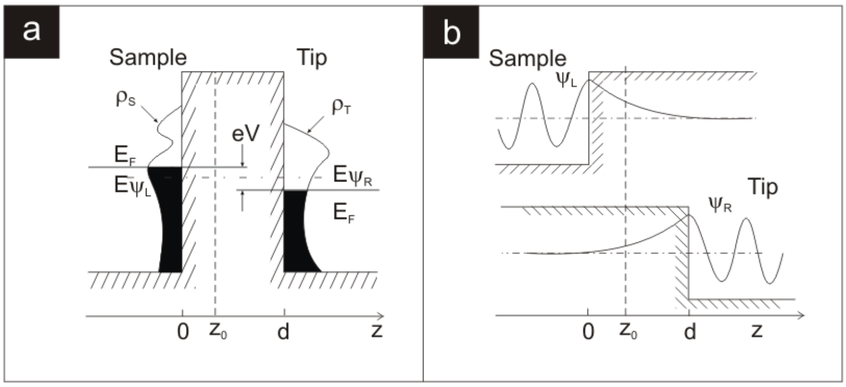

Fig. 2.4: a) Diagram of the energy levels of a tip and sample, for a negative-biased sample (Tunneling from the occupied states of the sample into the unoccupied states of the tip). b) Scheme of the overlapping of the two unperturbed wavefunctions of the tip and sample.

The basic assumption of Bardeen's formalism is that the two electrodes can be described as independent systems. The tunneling process is regarded as a small coupling that does not significatively perturb the electrodes wavefunctions. Hence, the Hamiltonian can be written as a sum of three terms

$$H = H_L + H_R + H_T \tag{2.4}$$

where H_L and H_R are the Hamiltonians that describe the electrons on the left and right metal electrodes (see Fig. 2.4) . The wavefunctions for electrons in each electrode are solutions of H_L and H_R respectively. H_T is the „tunneling perturbation“ or the so called transfer Hamiltonian, that describes the tunneling of electrons from one electrode to the other. The process of tunneling is then thought as a transition between two weakly overlapping unperturbed states, from an initial state in the left electrode to a final state in the right electrode. By using first order perturbation theory, the transition probability of an electron in a state ψ_L to a state ψ_R can be expressed as

$$\Gamma_{LR} = \frac{2\pi}{\hbar}|M_{LR}|^2\delta(E_L - E_R) \tag{2.5}$$

Bardeen showed [32] that the tunneling matrix element M_{LR} can be determined by a surface integral on a separation surface between the two electrodes as

$$M_{LR} = \frac{\hbar^2}{2m} \int d\mathbf{S} \cdot (\psi_R^* \nabla \psi_L - \psi_L^* \nabla \psi_R) \tag{2.6}$$

The tunneling current is obtained as the sum over all relevant states, i.e., electrons flowing from the occupied states in the metal with the higher Fermi energy to unoccupied states in the metal with the smaller Fermi energy [1]. At any finite temperature, the electrons in both electrodes follow the Fermi distribution. Using Eq. 2.6, the tunneling current can be written as

$$I = \frac{4\pi e}{\hbar} \int_{-\infty}^{\infty} [f(E_F - eV + \epsilon) - f(E_F + \epsilon)] |M_{LR}|^2 \rho_L(E_F - eV + \epsilon) \rho_R(E_F + \epsilon) d\epsilon \tag{2.7}$$

where *f(E)* corresponds to the Fermi distribution function, *V* is the applied bias voltage, and $\rho_L(E)$ and $\rho_R(E)$ are the DOS of the two electrodes.

Within the transfer hamiltonian approach, the tunneling current can be seen as a convolution of the DOS of the two electrodes, and for STM, as a convolution of the tip and the sample DOS.

The Tersoff–Hamann approach: low–bias voltage limit

The more intuitive interpretation of STM images is due to the seminal work of Tersoff and Hamann (TH) [33]. Employing Bardeen formalism, Tersoff and Hamann modeled the tip as a local spherical potential well at its closest point to the surface, and computed the matrix element only for an s–wave tip wavefunction.

In the low bias voltage limit and at low temperatures, only states at the Fermi energy can make a contribution to the tunneling transition and Eq. 2.7 is simplified as

$$I = \frac{4\pi e}{\hbar} \int_{0}^{eV} |M|^2 \rho_s(E_F - eV + \epsilon) \rho_t(E_F + \epsilon) d\epsilon \tag{2.8}$$

In order to calculate the tunneling current, Tersoff and Hamann considered as a starting point an ideal STM tip. They considered the tip to be a mathematical point source of current, whose position is denoted by $\mathbf{r}_t$. Under all these assumptions (low temperature, low–bias voltage and ideal tip), the tunneling current becomes

$$I \; \alpha \; \Sigma_s |\psi_s(\mathbf{r}_t)|^2 \delta(E_s - E_F) \equiv \rho_{\mathbf{S}}(\mathbf{r}_t, E_F) \tag{2.9}$$

This model provides a very appealing and simple interpretation of the tunneling current in terms of a familiar quantity: the local density of states (LDOS) of the bare sample surface, at an energy eV with respect to the Fermi level E$_F$, taken at the center of curvature of the tip $\mathbf{r}_t$. More sophisticated treatments have been developed in which the microscopic nature of the tip

---

[1] In this case from the left to the right electrode.

has been taken into account [34].

From a practical point of view, the TH approach provides an easy method to compute constant current, i.e. constant LDOS contours in a straightforward manner, whenever there is no substantial chemical interaction between the surface and the tip. For metals, the crossover regime between point contact and vacuum tunneling has been estimated to be around 5–8 Å under low–bias voltage conditions [35, 36].

For semiconductors, low–bias voltages can lead to very small distances. Additionally, the LDOS shows a strong variation with the voltage range considered. In particular, it changes discontinuously at the band edges. With negative sample voltage, current tunnels out of the valence band (occupied states) of the sample into the unoccupied states of the tip, while for positive sample voltages, current tunnels into the conduction band (unoccupied states) of the sample from the occupied states of the tip. The corresponding images, reflecting the spatial distribution of the valence and conduction band wavefunction respectively, may be qualitatively different (see for instance Fig. 2.5 and Fig. 2.8 a and b).

On the other hand, at very high–bias voltages the current will be given by the Fowler–Nordheim equation [37] developed for emission in vacuum, i.e., for field emission current. For intermediates voltages various formulas have been developed to connect the two limits. A more realistic description of the potential barrier is needed in accordance with the system to be study, like in the case of semiconductors.

WKB approximation: intermediate–bias voltage limit

Tunneling models have predated the existence of STM. Simmons [38] was the first to derive a generalized formula of the tunnel effect between similar electrodes, separated by a thin insulating film, for all voltage ranges. Simmons made use of the one dimensional Wentzel–Kramers–Brillouin (WKB) approximation to solve this problem. He expressed the current density through a barrier of height V(z) in a very general form as

$$j = \frac{4\pi m^2 e}{h^3} \int T(E_z) dE_z \int dE[f(E) - f(E - eV)] \tag{2.10}$$

where the tunneling probability is given by the WKB approximation as

$$T(E_z) = exp[\frac{-2}{\hbar} \int \sqrt{2m(V(z) - E_z)} dz] \tag{2.11}$$

here *f(E)* corresponds to the Fermi–Dirac distribution function, and the z direction is taken as the direction normal to the electrodes. The normal energy distribution function can be express as

$$N(E_z) = \frac{4\pi m^2 e}{h^3} \int_0^\infty dE_\parallel [f(E) - f(E - eV)] \tag{2.12}$$

where $E = (E_x + E_y) + E_z = E_\parallel + E_z$. Substituting Eq. 2.12 into Eq. 2.10, the current density can be simplify in terms of the normal component of the energy distribution E_z as

$$j = \int_0^\infty dE_z T(E_z) N(E_z) \tag{2.13}$$

Given a potential barrier, Eq. 2.13 can be used to calculate the current density. For a trapezoidal barrier as in Fig. 2.2, the tunneling transition probability T(E_z) is given by

$$T(E_z) = exp[-2z\sqrt{\frac{2m}{\hbar}(\frac{\phi_s + \phi_t}{2} - \frac{eV}{2} - E_z)}] \tag{2.14}$$

where z is the tip–sample separation distance, and ϕ_s and ϕ_t are the work functions of the electrodes. From Eq. 2.14, it can be seen that the tunneling current does not depend solely on the separation distance z. At intermediate voltage ranges, it also shows an exponential dependance on the voltage. The tunneling current contains information on the tip and sample density of states alike, weighted by the transmission probability. The interpretation of the STM images can no longer be simplified, as in the case of low-bias voltage regime.

At negative sample bias (eV < 0), the transmission probability is largest for E_z =0, that is for the electrons at the Fermi level of the sample. Similarly, if $eV > 0$ (positive sample bias), the probability is largest for $E_z = eV$, corresponding to electrons at the Fermi level of the tip. In other words, the tunneling probability shows a maximum for electrons at the Fermi level of whichever electrode happens to be negatively biased.

For semiconductor surfaces, the STM images are almost entirely determined by the local electronic structure, not by the actual position of the atoms. Voltage dependant imaging can provide information on the relative spatial locations of the various electronic states at the surface.

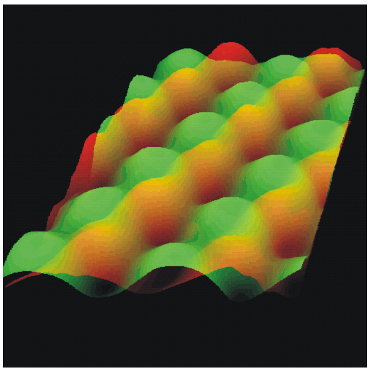

Fig. 2.5: Combined color STM images of GaAs(001). The red color corresponds to the occupied states (As atoms) and the green one corresponds to the unoccupied states (Ga atoms). Image taken from [39].

For instance, Feenstra et al. [39] were able to determined the buckling angle between Ga and As atoms in the GaAs(110) surface, by combining voltage–dependent images with theoretical calculations. The distinct chemical nature of the cation (Ga) and anion (As) species manifests in an spatial separation of the occupied and unoccupied states. By scanning with biases close to the band edges, they showed that at positive sample bias (unoccupied states), the current density maxima appeared centered around the location of the Ga atoms, while for a negative bias (occupied states), the maxima could be associated with the position the As atoms. By comparison between the STM images and state–density calculations, the buckling angle produce by the As–atoms displacement was accurately determined.

Scanning Tunneling Spectroscopy

The primary goal of the STM was to perform local spectroscopy on small areas. The voltage dependance of the tunneling current is the essence of the spectroscopic capabilities of STM, consolidating it as one of the most important tools for surface studies. By monitoring changes of the tunneling current as a function of the applied bias, it is possible to directly probe the energy–dependent DOS of the tip and sample.

In order to be able to correlate morphological characteristics of the surface with its electronic properties, it is necessary to measure the tunneling current as a function of bias voltage (I/V curves) at a fixed tip–sample separation distance, for different locations on the surface. This process is called Scanning Tunneling Spectroscopy (STS) [40].

The basic mode of operation for STS is similar to constant current imaging, where a feedback loop is used for adjusting the tip–sample distance while scanning, in order to maintain the tunneling current constant for a set of (x,y) points. In the case of STS, once the tip is localized over the point of interest, the separation distance is adjusted by setting a specific value of the tunneling current and a specific value of the Bias voltage, known as stabilization parameters. With the feedback loop disabled and the position fixed, the bias voltage is ramped and changes in the tunneling current and/or the differential conductance (dI/dV) are recorded. Afterwards, the feedback is closed and another point is chosen to perform the same measurement all over again. The differential conductance can be estimated from the previously discussed tunneling models.

In the most simple case, considering a constant tunneling barrier over the applied voltage range, for the low-voltage regime, the differential conductance is given in a simple form as

$$\frac{dI}{dV} \; \alpha \; \rho_s(eV)\rho_t(0) \tag{2.15}$$

For intermediate-voltage regimes, the tunneling probability depends strongly on the separation distance and the applied voltage. Feenstra et al. [40] proposed a normalization procedure to eliminate the dependance on the separation distance given as follows

$$\frac{dI/dV}{I/V} \simeq \frac{\rho_s(eV)}{\frac{1}{ev}\int_0^{eV} \rho_s(E)dE} \tag{2.16}$$

2.3 Atomic Force Microscopy

The main drawback of STM is the need of a conductive sample. This was circumvented soon after the development of the STM, with the invention of the atomic force microscope (AFM) by Binnig, Quate and Gerber [41] in 1985. Nowadays the AFM is by far the most commonly used of the scanning probes microscopes (SPM). It is a highly versatile SPM, with the advantage of imaging almost any type of surface, including polymers, ceramics, composites, glass, and biological samples [42].

The backbone of the AFM working principle is the sensing of the interaction forces between a sharp tip and a sample. A constant force is maintained between the probe and sample with the help of a feedback control unit, while the tip is raster–scanned across the surface. Different kind of forces can be measured with AFM such as, mechanical contact, Van der Waals, capillary, chemical bonding, electrostatic, magnetic, Casimir, etc. [43].

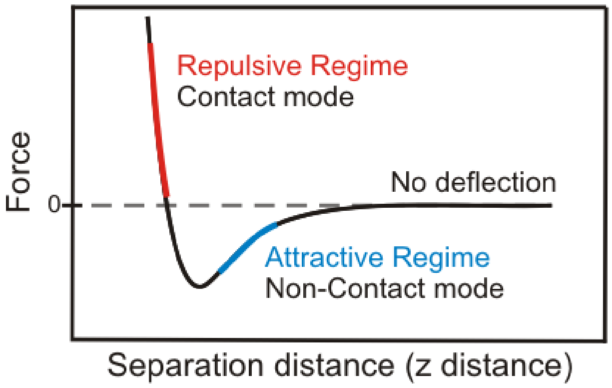

Fig. 2.6: Potential energy diagram of the interaction force between tip and sample vs separation distance.

In the AFM, the force is not measured directly. The tip is mounted at the end of a cantilever, which acts as a spring. Depending on the nature of the interaction and the separation distance, the tip is repelled by or attracted to the surface (Fig. 2.6), leading to a deflection of the cantilever. Several detection schemes have been developed for measuring the amplitude of deflection. The preferred detection method is based on a position–sensitive array of photodiodes that records the angle of reflection of a laser beam focused on the top of the cantilever (Fig. 2.7).

During scanning, changes in the deflection of the cantilever are produced due to the surface topography. As a consequence, the reflection plane for the laser beam changes and thus its position on the photodiode. The change in the signal between the segments of the photodiode is a sensitive measure for the deflection of the cantilever.

By measuring the deflection of the cantilever, and knowing its stiffness k, in a first approximation, the force can be obtained using Hook's law as

$$F = -kz \tag{2.17}$$

where F is the force and z is the distance which the cantilever is bent.

A topographic image of the sample is obtained by plotting the deflection of the cantilever versus its position on the sample. Nowadays, micro–fabricated cantilevers (Silicon Nitride or single crystal Silicon) with spring constants of less than 0.1 N/m and resonance frequencies of more than 100 kHz are commercially available, allowing measurement at forces typically in the range from 1 nN (in liquids) to 100 nN (in air).

Measuring the force with the cantilever in the AFM can be achieved in a static and a dynamic mode. In the first mode, the deflection of the cantilever is directly measured. In the second mode, the cantilever is vibrated and changes in the vibration properties are recorded.

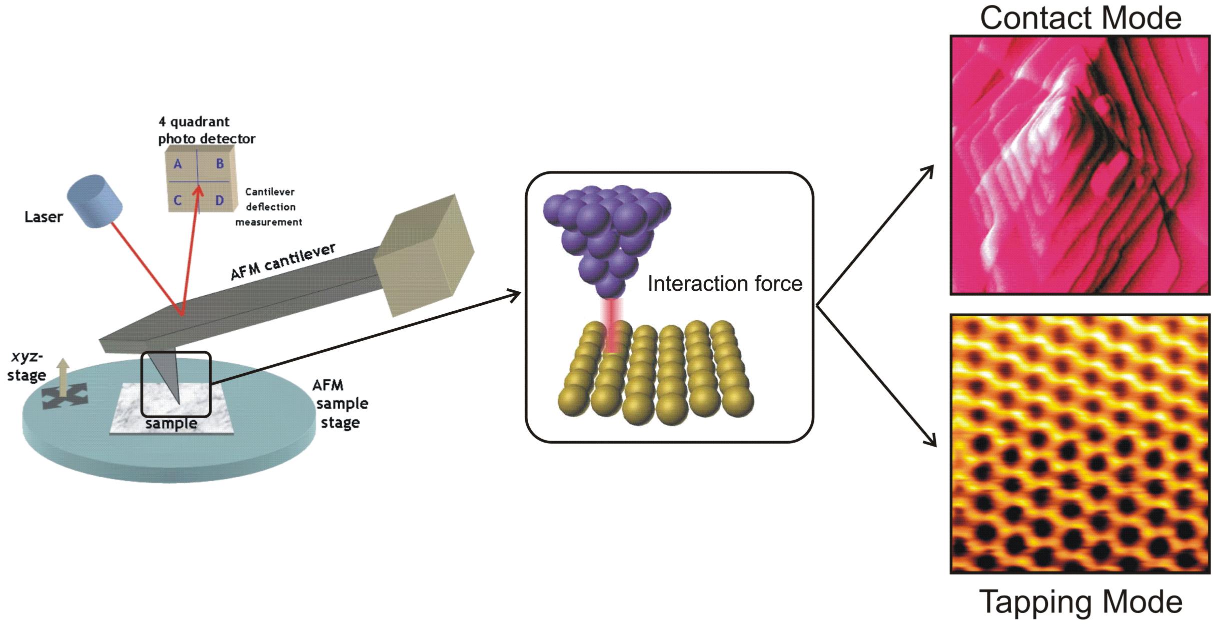

Fig. 2.7: Working principle of an AFM with an optical detection array of photodiodes. The contact mode image corresponds to Polyethylene crystals on mica [44]. The image size is 1 μm x 1 μm. The tapping mode image corresponds to Graphite [45]. Image size 2 nm x 2nm.

In the static mode, the tip is usually maintained at a constant force by adjusting the distance between tip and sample, while scanning. Since the typical surface–tip interactions are often less than one nano–newton, the tip is softly touching the surface; for this reason this mode is often called „contact “ mode.

In the „non–contact“ mode the tip is oscillated above the surface by a piezoelectric oscillator, close to its resonance frequency. The cantilever position is kept in the attractive regime (Van der Waals forces), meaning that the tip is quite close to the sample, but not touching it. When the vibrating cantilever comes close to the surface ($\approx$ 50–100 Å), the oscillation amplitude, phase and resonance frequency are modified by tip–sample interaction forces, in response to force gradients from the sample. In this way changes in the oscillation properties in respect to the external reference oscillation, provide information about the sample's characteristics.

The „dynamic contact mode “ (also called intermittent contact or „tapping mode “) was developed in order to achieve higher resolution under ambient conditions. In the „tapping mode “, the cantilever is oscillated in such a way, that it comes in contact with the sample within each cycle. To avoid dragging the tip across the surface, enough restoring force is provided by the cantilever spring to detach it from the sample. As the oscillating cantilever begins to intermittently contact the surface, the oscillation is necessarily reduced due to energy losses caused by the tip contacting the surface. Variations in the measured oscillation amplitude and phase are also indicators, in this case, of the tip–sample interaction.

In contrast to STM, AFM images can be directly interpreted as surface topography information both on the large and atomic scale. In the ideal situation, in which the tip is a dimensionless point and the piezos are perfectly linear, the image faithfully reproduces the surface topography. Thus, in a first order approximation, the influence of electronic inhomogeneities on the image features can be neglected. This property makes the AFM an effective tool for determining surface roughness or for the measurement of width, height and depth of individual nanostructures. Recently, with the use of lock–in techniques at low temperatures [46], high resolution images of the Ge(105)-1x2 surface formed on the Si(105) substrate have been achieved. „Non–contact“ AFM image shown in Fig. 2.8c reveals all dangling bonds on the surface, independently of any electronic contribution. For comparison, two STM images taken at negative (Fig. 2.8a) and positive (Fig. 2.8b) bias voltage are also shown. The strong dependance on the bias voltage is evident for the STM images. The rebonded–step (RS) model of this surface is superimposed on the right image. Furthermore, chemical identification of individual surface atoms by means of AFM under dynamical mode has been possible at room temperature, with the use of a force normalization calibration method [47] (Fig. 2.8d).

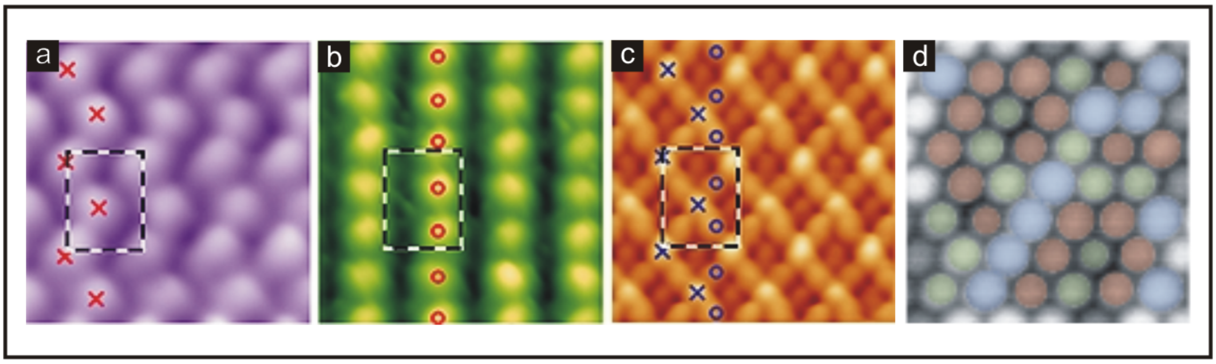

Fig. 2.8: On the left: High resolution images of Ge/ Si(105) taken with a) a STM at negative bias voltage, b) a STM at positive bias voltage and c) a non–contact AFM at low temperature [46]. On the right: chemical composition of Pb and Sn on Si(111). The color assignment of the atoms was given, among other measurements, through the maximum attractive total force obtained in the experiments [47].

In this work, all the AFM images were taken in tapping mode at room temperature. A commercial Digital Instruments Nanoscope IIIa multimode SPM with n^+ Si tips was used for this matter.

2.4 Molecular Beam Epitaxy

Molecular Beam Epitaxy (MBE) is a widely used growth technique developed in the early 1970's, that has become a milestone for the growth of semiconductor devices. The principal characteristic of MBE are the high purity of the elements used and the high control attainable during the growth. Another great advantage of MBE is its compatibility with in–situ characterization methods in every step of the process. Furthermore, MBE growth processes can be automatized, allowing the application of this technique in the commercial production of semiconductor devices.

MBE growth takes place under ultra high vacuum (UHV) and, as indicated by its name, materials are deposited on clean crystalline substrates in the form of molecular beams to produce thin epitaxial layers. The molecular beams are formed from the thermal evaporation of the desired material, heated independently in an effusion cell, better known as Knudsen cell. The growth speed is of the order of Å per second and the fluxes can be obstructed in fractions of a second, allowing atomically sharp material transitions. By MBE, it is possible to produce high quality layers of abrupt interfaces with an excellent thickness, doping and composition control, as well as low dimensional quantum structures [48].

One of the key elements for a good epitaxial growth is the structural quality of the substrate. Different ex–situ and in–situ cleaning techniques are applied to the substrate prior to the growth, such as chemical treatments, ion sputtering, degassing at high temperature, flash annealing, etc.

In the case of III–V materials, commercially prefabricated wafers are used. The wafers are oxidized in a controlled manner after growth. This oxide layer provides a protection against exposure and is removed in–situ by desorption, before their actual use as substrate.

Once the substrate is cleaned, a buffer layer of the same material as the wafer, e.g, GaAs, is grown in order to bury defects and to define the morphology of the growth surface. An overpressure of As is necessary for the growth of As–terminated surfaces in order to compensate the desorption produced by the sample heating. The subsequent steps vary according to the structures to be grown.

The growth speed, sample temperature and surface reconstruction are characterized by reflection high energy electron diffraction (RHEED). RHEED also provides information about the transition from 2D to 3D growth, such as the case of QDs formation [49].

To produce self–organized QDs, after the buffer layer, a material with a different lattice constant is deposited in order to induce strain. The growth proceeds in planar fashion, until for a specific coverage the nucleation of 3D islands takes place. Afterwards the as–grown islands need to be overgrown with a larger band gap material to guarantee the existence of confined states.

The system employed for the sample preparation in this work is a commercial Riber MBE system, with a base pressure of 1 x 10^{-11} mbar. Commercial heavily Si-n^+ doped GaAs wafer were used as a substrate for all the samples used in this work. After deoxidation at 640^{o}C in UHV, a 400 nm n–doped GaAs buffer layer was grown ($N_D \simeq 2$ x 10^{18} cm^3) at a growth rate of 0.6 ML/s, with a substrate temperature of 610^{o}C. The temperature calibration is made by monitoring with RHEED the GaAs reconstruction transition from a (2x4) to a c(4x4) surface ($\simeq$ 480 ^{o}C). Afterwards, the temperature is stabilized at the growing temperature which, if not specified otherwise, corresponds to 500^{o}C. After depositing a 10 –nm–thick undoped GaAs layer ($N_A < 1$ x 10^{15} cm^3), islands are grown by deposition of InAs at a growth rate of 0.008 ML/s under an As_4 beam equivalent pressure (BEP) of 8 x 10^{-6} mbar.

Immediately after finishing the growth, the substrate heater is turned off while keeping a constant As pressure, resulting in an initial cooling rate of 1 ^{o}C/s. As soon as room temperature is reached, the samples are transferred under UHV conditions to the STM chamber, where STM images are taken in the constant current mode with typical tunneling currents of 0.1 nA and negative bias voltage between -2.5 and -3.0 V. In the case of AFM analysis samples were imaged ex–situ in air.

The sample growth was made in collaboration with the MBE group of the Max–Planck–Institute for Solid State Research in Stuttgart.

2.5 Experimental set–up

In the development of this work, two different STM set–ups were used. The studies presented in Chapter 3, 4 and 5 were carried out using a room temperature (RT), home–built STM, which is designed to host samples with a total area of 5 cm x 5 cm. In particular, this STM is compatible with two MBE systems: one for 2–inches III–V compounds and another 3–inches for Si/Ge compounds. A detailed description of such STM can be found in [50]. For the studies presented in Chapter 6, a STM operating at LT was required. Experiments were performed in a home–built system with a base temperature of 5 K. This LT–STM is compatible only with the III–V MBE system. More details about the experimental set–up are given in [51,52].

The RT–STM offers the possibility of a wide scan range of 3.5 cm^2 (Fig.2.9c), allowing the study of samples similar to those grown in MBE systems for application purposes. Moreover, the STM head design is also suitable for large vertical displacements for the future possibility of implementing cross–sectional STM studies. Contrary to the RT–STM, where the sample size is not a constriction, LT–STM requires small sample sizes due to limitation in the cooling power of cryogenic systems. In order to fit each STM sample holder design, modifications to

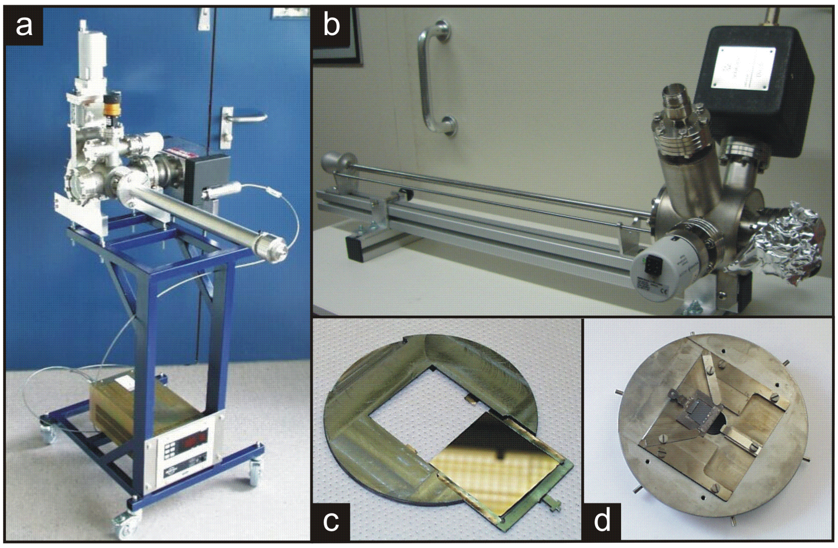

Fig. 2.9: a) Vacuum suitcase used for transferring samples to the RT–STM. b) Small vacuum suitcase used for transferring samples to the LT–STM. In c) and d) modified Mo block, adapted to host the home–built STM sample holder, are displayed.

the standard Molybdenum blocks were necessary. The modified Mo blocks used for the growth of samples for each particular STM are shown in Fig. 2.9 c and d, respectively.

A crucial issue in our studies is the preservation of the sample under UHV conditions. To accomplish that, the transfer process of the samples from the MBE to the STM is performed by using two detachable vacuum chambers (vacuum suitcase), one for each STM system. Both vacuum suitcases are independently pump through ion pumps and kept at a base pressure of 1 x 10 $^{-10}$ mbar. For the LT–STM, a smaller vacuum suitcase was constructed to allow the transfer of the sample under UHV conditions from the MBE location to the LT–STM located four floors above. A battery operated ion pump allows long distance transportation of the sample under UHV. The vacuum suitcase of the RT–STM and the one for LT STMs are shown in Fig. 2.9 a and b respectively.

The transfer process is similar for both systems, regarded that the RT–STM vacuum suitcase is attached directly to the load–lock of the MBE machine, while for the LT–STM, a peripheral load–lock needed to be attached to the middle chamber of the III–V machine in order to support a vacuum suitcase compatible with the existing LT–STM set–up.

A typical transfer process can be described as follows: first, the vacuum suitcase is attached in the corresponding load–lock. Soon after the sample is grown, it is removed from the growth chamber and secured in the vacuum suitcase. The vacuum suitcase is then detached from the MBE system, transported to the STM facilities and then attached to the STM load–lock. The load–lock chamber is pumped afterwards, from atmospheric pressure until UHV is reached.

Once proper vacuum is reached, the sample is transferred to the scanning stage.

Images in the RT–STM are taken in the constant current mode by using a bias voltage of around -2.5 and -3V and tunneling currents of $\sim$ 1 nA. STM images and STS spectra at low temperature were acquired at various values of the bias voltage at different tunneling currents and will be indicated in due time.

Electrochemically etched tungsten tips were used for scanning in both systems (Fig. 2.10). Passivation and oxide removal were achieved by immersing the tips in a solution of 50% HF (Hydrofluoric acid) for 30 sec, just before their insertion in vacuum. No further tip treatment was performed in vacuum. The tip preparation procedure is described in [53].

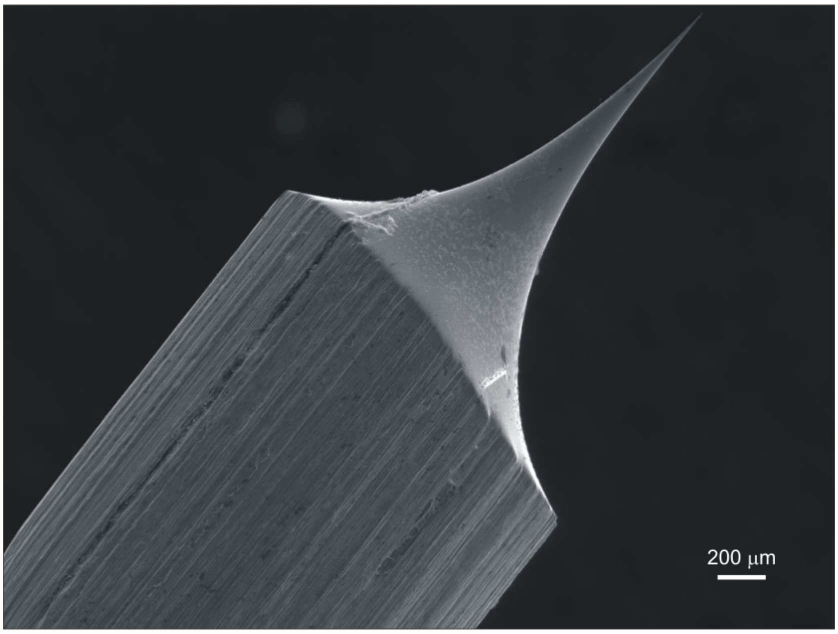

Fig. 2.10: Scanning Electron Microscope (SEM) image of an etched tungsteng tip, used for STM imaging, prior to the HF oxide removal.

Chapter 3

On the nucleation of 3D InAs strained islands

3.1 Self-Organization: Let nature do the work!

Whoever has marveled at the beautiful color of a morpho butterfly, fell enchanted by the radiance of light through clouds patterns in a sunset or just simply delighted with a walk over sand dunes, can say that she or he has encountered the beauty of self-organization.

A system is considered to be self-organizing if it acquires a spatial, temporal or functional structure without prodding. The idea that a system, if let alone can become more ordered by itself can be counterintuitive, but there are many examples in nature of systems which can start in a highly random state and, without being shaped from the outside, become more and more organized.

The term *self-organization* was coined in 1947 by W. Ross Ashby [54] in his pioneering work on cybernetics and it is presently a keyword to describe cooperative phenomena in diverse disciplines such as natural sciences, mathematics, sociology, psychology, geology, economics, linguistics and even in philosophy [55]. Self-organization also expands over different size scales, from glacier morphology to wasp colonies or to the formation of 3D nanometric structures during the growth of strained films [56]. It is precisely on this latter topic that we will focus our attention.

Self-organization in thin films offers the possibility of a direct fabrication of nanostructures that, in contrast to lithographic methods or SPM-fabrication, is technologically much simpler and represents a very cost-efficient route towards large-scale device production. Even more, self-organized structures are produced with no defect and very small sizes, and as a consequence large confinement energies.

3.2 Thin film growth

A film whose thickness is not larger than a few micrometers is consider a thin film. The key factor governing the properties of a thin film is the energy associated with its delimiting surface. The surface energy γ quantifies the disruption of chemical bonds present at the film's interface. These broken bonds (dangling bonds) represent a high energetic cost. Very often surface atoms rearrange their position with respect to those in the bulk and bond with other atoms in the surface (surface reconstruction) to minimize their energy. Atoms may as well bind and react with other kind of atoms, leading to an adsorption process which passivates the surface and thus minimize its energy. Either by reconstruction or passivation, the surface tends to reduce most of the dangling bonds in an attempt to reach an equilibrium configuration. Once a thin film has reached thermodynamic equilibrium, all surfaces processes, such as adsorption and re-evaporation, must obey detailed balance to preserve it.

However, for a thin film to grow, thermodynamic equilibrium must be broken, since the rate of the material leaving the substrate should be less than the material getting attached to it. The degree to which a thin film deviates from equilibrium, determines the main microscopic mechanisms that resolve to what extent, the final state will be ruled by thermodynamic quantities or by the growth kinetics. Some of the basic atomistic processes that can take place during initial stages of growth (Fig. 3.1), occurring at the interface are

- interaction between the surface and the gas phase: arrival, accommodation of atoms on the surface or re-evaporation of incoming atoms (condensation, adsorption or desorption);
- diffusion processes on the surface: migration on terraces, along or across steps until an incorporation site is found (diffusion and binding) or diffusion into the bulk by exchanging position with a substrate-atom (interdiffusion);
- nucleation and growth: aggregation into 2D or 3D islands, ripening and coalescence.

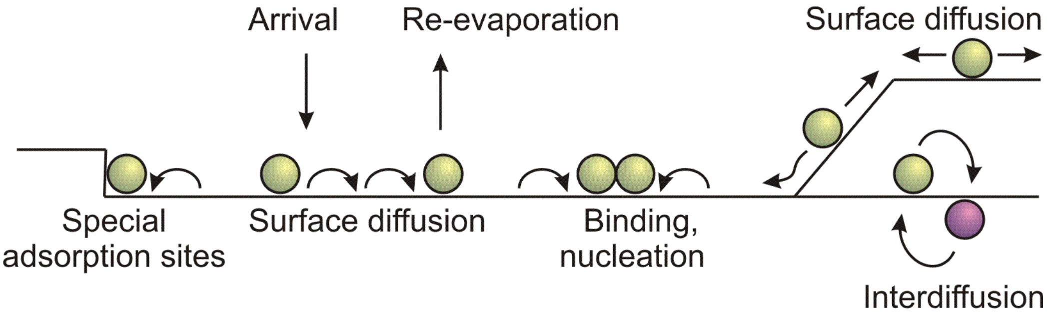

Fig. 3.1: Main atomistic processes taking place during thin film growth.

Thin film growth, not only its properties, is also determined by the balance of the energy of cohesion (bonding of neighboring atoms in the substrate surface) and the energy of adsorption (bonding to incoming atoms). Furthermore, the growth of a thin film might be as well, influenced by different types of growth instabilities, whose effect is to deform the growing surface at the microscopic level [57]. Such instabilities can be:

- geometric instabilities, produced artificially as by shadowing or oblique deposition angles;
- kinetic instabilities, present when the growth is too fast for the surface to reach its equilibrium shape, as in the formation of dendritic islands on a surface;
- thermodynamic instabilities, which take place when trying to produce a thermodynamically unstable material, as for lattice-mismatched growth.

Kinetic instabilities can originate because of diffusion biases caused by energetic surface barriers, such as the Ehrlich-Schwoebel barrier [58, 59]. For example, the relative magnitude of terrace diffusion and edge diffusion determines if the shape of an island is fractal or compact [60].

Heteroepitaxial growth can be thermodynamically unstable if the difference of lattice constants of the pure materials is too large. This thermodynamic instability, generated by the misfit between the lattice constant of the substrate and that of the deposited layer, is the most common driving force for self-organization.

Under these conditions, the growth starts with the formation of a pseudomorphic layer which is elastically distorted, and thus can not grow indefinitely thicker. The elastic energy stored in the film increases with growth, up to a certain critical thickness (θ_c) when relaxation occurs.

In general, energy can be reduced via plastic or elastic relaxation. During plastic relaxation, the elastic energy is reduced through the formation of misfit dislocations at the layer/substrate interface. If the energy decrease is via elastic relaxation, self-organized 3D structures are formed. Island formation provides strain relaxation which is not possible in a thin film, but it also results in an increase in the surface energy. Residual strain on the islands can be further reduced by the incorporation of dislocation at later stages of the growth. The interplay between the strain relaxation and the increase in surface energy in the growth of self-organized QDs, give rise to a very robust and complex behavior.

This work deals precisely with the study of the nucleation and further evolution of strain-induced self-organized 3D nanostructures in the case of semiconductor heteroepitaxy. If we want to gain control over thin film growth and more specifically over self-organized nanostructures, a deep understanding of the contribution of the distinct atomistic processes and their dependance on the growth parameters is required. It is the goal of this thesis to make a contribution towards the understanding of this intriguing phenomena.

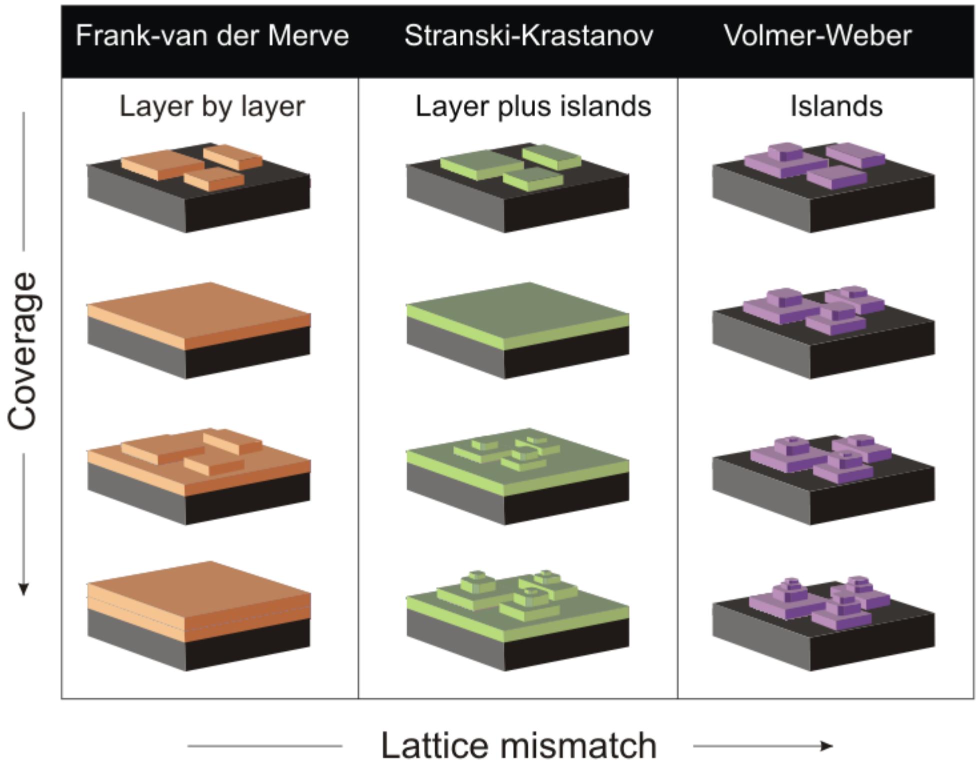

Fig. 3.2: Schematic representation of the three growth modes of a thin film for different coverage. Left to right panels: Frank-van der Merwe (FM), Stranski-Krastanov (SK) and Volmer-Weber (VW) mode.

3.2.1 Growth modes in heteroepitaxy: to wet or not to wet

Based on thermodynamic arguments, Bauer [61] distinguished that when close to equilibrium, a thin crystalline film grows by one of three possible mechanisms: the Frank-van der Merwe (FM), the Stranski-Krastanov (SK) or the Volmer-Weber (VW) growth modes. In which mode the film grows, depends upon the relatives magnitudes of the surface energies of the substrate γ_s, of the film γ_f and of the surface energy of the interface γ_i (Fig. 3.2). Neglecting edge energies and the orientation dependance of the surface energies, the quantity which determines the growth mode may be written as:

$$\triangle\gamma = \gamma_f + \gamma_i - \gamma_s \tag{3.1}$$

The growth proceeds in a layer-by-layer fashion, when the atoms feel more attracted to the substrate than to each other. This happens, independently of the thickness of the film, when the sum of the surface energy of the newly formed epilayer γ_f and of the interface energy γ_i is lower than the energy of the substrate surface γ_s, i.e., whenever the condition $\triangle\gamma \leq 0$ is fulfilled. This is known as the Frank-van der Merwe growth mode and it is said that the film wets the substrate. Inherently, this condition applies to each new layer of the film during growth, and thus Eq. 3.1

can be expressed in terms of any pair of subsequent layers *n* and *(n-1)* as follows

$$\triangle\gamma(n) = \gamma_{f(n)} + \gamma_{i(n,n-1)} - \gamma_{f(n-1)} \tag{3.2}$$

where $\gamma_{f(n-1)}$ corresponds to γ_s for *n*=1.

From Eq. 3.2, it is clear that in the case of homoepitaxy, where the film and the substrate consist of the same chemical species, for all *n* the condition

$$\triangle\gamma \leq 0 \tag{3.3}$$

is rigourously fulfilled, since $\gamma_{f(n)} = \gamma_{f(n-1)}$ and $\gamma_{i(n,n-1)} = 0$.

In a more general case, the chemical composition and as a consequence, the structure of deposited layer differs to some extent from that of the substrate. At the early stages of the growth (for *n* close to 1), $\gamma_{f(n)}$ deviates slightly from the surface energy of the starting surface γ_f, since the film must initially resemble the substrate structure, i.e., $\gamma_{f(n)} \simeq \gamma_{f(n-1)}$. Additionally, depending on the specific adsorbate-substrate interaction, there will be a contribution of the strain energy γ_i^{ε} to the interfacial energy γ_i. In the case where there is no significant misfit between the film and the substrate, the strain contribution γ_i^{ε} rapidly approaches to zero within the first few monolayers and the FM mode sets in, as in the growth of lattice matched AlAs on GaAs(001) [62].

In all other cases, as the growth proceeds, the strain energy γ_i^{ε} is actually enlarging with increasing *n*. This leads to an increase of $\gamma_{i(n)}$ until a critical thickness n^* is reached, for which the condition 3.3 is no longer valid. At this point, the growth changes from a layer-by-layer (2D) mode to the formation of 3D islands over the wetting layer previously formed. This is known as the Stranski-Krastanow mode. The growth of InAs on GaAs(001) [63] represents a prime example of this mode.

When the intra-adsorbate interaction is stronger than the adsorbate-substrate interaction, the condition 3.3 is never fulfilled and 3D islands nucleate since the very beginning of the growth. This is known as the Volmer-Weber growth mode. 3D island formation occurs since the material does not wet the surface for it is energetically unfavorable. Such is the case of the growth of Ge on C-alloyed Si(001) [64].

3.2.2 Capillary model of Nucleation

Using classical theory of nucleation, the necessary energy for the formation of a strained 3D nuclei, can be represented in a very general form, as the sum of:

- the energy arising from the change in volume accompanying the structural change from the vapor phase to the crystal phase;

- the lattice strain energy associated with the distortions produced by the partial or complete coherency between the two lattices;
- the island surface energy.

For simplicity, we can assume the surface energy to be isotropic, so the energy of formation for a spherical nucleus of radius *r* can be expressed as

$$\triangle G = -\frac{4}{3}\pi r^3 \triangle G_\mu - \frac{4}{3}\pi r^3 \triangle G_{strain} + 4\pi r^2 \gamma \tag{3.4}$$

in which $\triangle G_\mu$ correspond to the change of the free energy per unit volume upon formation, $\triangle G_{strain}$ is the strain energy per unit volume and γ the surface energy per unit area.

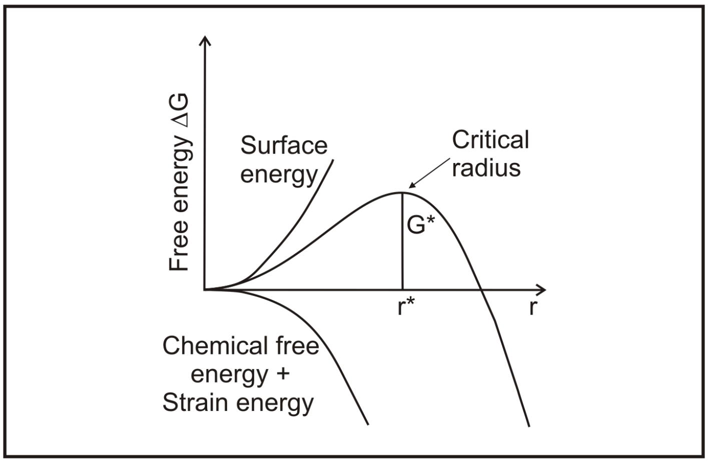

Fig. 3.3: Plot of the free energy change upon nucleation versus the spherical nucleus radius r.

From Eq. 3.4, we can notice that for small values of *r*, the surface term dominates and $\triangle G$ is positive, nuclei of all sizes are unstable and they will tend to shrink rather to grow (Fig. 3.3). At larger *r*, the volume free energy dominates and nuclei are stable because growth is accompanied by a decrease in *G*. There will be a size for which the nuclei can gain energy either by growing or dissolving, i.e., when $\frac{\delta G}{\delta r}|_{r_c} = 0$. These are called 'critical nuclei' and from Eq. 3.4 one can calculate the critical radius r_c as

$$r_c = \frac{2\gamma}{(\triangle G_\mu + \triangle G_{strain})} \tag{3.5}$$

Substituting the value of the critical radius in Eq. 3.4, the activation energy for the formation of stable nucleus is given as

$$G^* = \frac{16\pi\gamma^3}{3(\triangle G_\mu + \triangle G_{strain})^2} \tag{3.6}$$

From this simplified model, one can highlight that the existence of the surface term will always produce an activation barrier for nucleation and, that this activation energy varies inversely with the square of the nucleation driving force. The formation of stable nuclei will be determined by the balance between the energy gain due to the formation of a new stable state and the energy cost of creating a new surface.

In the case of semiconductor materials, several complications arise from the fact that the surface energy is not isotropic. γ is a function of the crystallographic directions, consequently the equilibrium shape must be obtained using the Wulff construction. There may be as well distinct surface reconstructions of different stoichiometry for the same orientation, leading to a piece-wise defined linear dependency of the surface energy on the chemical potential.

For lattice mismatched films, the surface stress also influences the surface energy value and induces changes in morphology, e.g., nucleation of steps, facets or defects [65, 66]. In the submonolayer regime, stress can cause intermixing and alloying, through diffusion of some of the deposited atoms into the top layers of the substrate [67, 68].

In the case of nucleation of strained islands, the role of strain is twofold. On the one hand, the strain dependence of the specific surface energies needs to be taken into account. On the other hand, the strain drives mass transport from regions of high strain to regions of smaller strain energy. Any deformation of the islands induces anisotropic changes on its facets as an elastic relaxation mechanism.

Applying the same thermodynamical rationale as in the previous section, the nucleation of strained islands can be understood from a pure energetic point of view: a morphological perturbation of a strained flat surface increases the surface energy, but reduces the total elastic energy by local elastic relaxation. The strain distribution in the growing layer is one of the main driving forces leading to the nucleation of nanostructures, and it also influences the particularities of their growth and mutual arrangement.

For the specific case of the SK mode, several approaches have been developed in an attempt to characterize the transition from a metastable 2D film to the spontaneous nucleation of 3D islands [69, 70] . It is important to note, that the elastic energy released by the islands depends mainly on their particular size and shape (for further details, see Chapter 4). Assumptions about the island morphology need to be made in order to formulate a theoretical description, proving experimental input to be of great value.

3.2.3 Stranski-Krastanov mode: lattice mismatched heteroepitaxy

The distinction between the different growth modes, strictly valid for close to equilibrium conditions, is applied to experiments only from a phenomenological point of view. For semiconductors SK growth is expected if the lattice mismatch is greater than 2%. There is an increasing number of systems under study, including several III-V, II-VI compound systems and group IV heterostructures [13], that grow in this regime and can be used for the self-organization of QDs.

Self-organized islands grown in the SK mode are free of dislocations, which is a mandatory requirement for device applications. Spontaneously formed islands have a typical lateral size of

10–100 nm, ergo, the wavefunctions of electrons and holes are confined in all three dimensions and as a consequence, their optical and electronic properties are greatly modified.

In order to use these islands to work as QDs, they must be embedded into a larger band gap material, potentiating their use in quantum information processing, quantum computation or optoelectronic applications.

The statistical nature of the growth will always give rise to a distribution of sizes, heights and compositions of the 3D islands, causing inhomogeneities in its optoelectronic properties and deterring their use for device applications. Nevertheless, island sizes can be tuned using the appropriate growth conditions, reducing the size dispersion to less than 10% [71] and frequently a bimodal size distribution is observed [72,73]. Despite each specific material system is characterized by its own peculiarities, for growth conditions close to the thermodynamic regime, striking similarities of shape, size distribution and evolution of the islands have been found [74]. This implies, that a general description based on thermodynamic quantities, as Bauer suggested for thin film growth, could give a general description of the QDs growth process.

In the forthcoming pages, the most important processes, namely nucleation, growth, evolution and capping of self-organized islands will be studied. In particular, a qualitative description of the growth of InAs on GaAs(001) will be presented, highlighting what seems to be a universal behavior of strained semiconductor QDs.

3.3 InAs on GaAs(001): 2D to 3D transition

Considered to be an instability of growth that diminished the performance of quantum wells, the formation of self-assembled QDs was underestimated for several years. In 1985, Goldstein et al. [63] reported good optical and crystalline properties of self-assembled InAs clusters formed by deposition of 2 ML of InAs over a GaAs (001) substrate (Fig. 3.4). This result prompted a whole new research area that continues to expand to the present day.

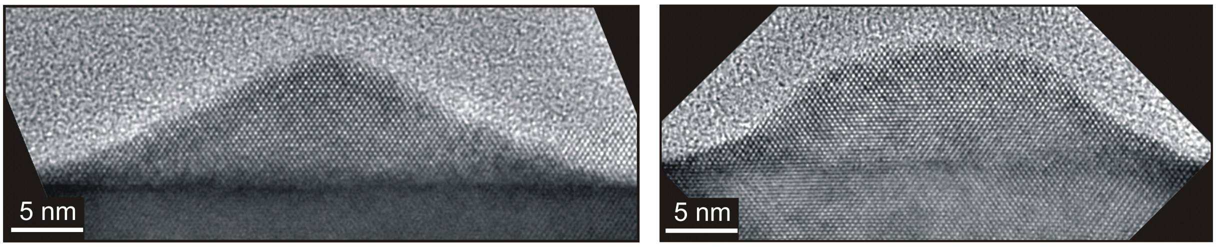

Fig. 3.4: High resolution TEM images of two different free standing InAs/GaAs(001) islands. Images taken from [75].

The growth of InAs layers on a GaAs substrate follows the SK growth mode, because of their large lattice mismatched (7.2%). Strain-induced self-organized islands combine advantages of bulk semiconductors with those of single atoms. They offer the capability of band gap engineering, allowing emission over a wide range of wavelengths, from the far infrared ($\sim 1.5\mu$m) to the blue region ($\sim$ 500nm), very suitable for diverse solid state devices and single dot applications [13].

The band gap of InAs (0.355 eV) is smaller than that of GaAs (1.424 eV), and the resulting band offsets can be controlled by manipulating the stoichiometry of the $\mathrm{In}_x\mathrm{Ga}_{1-x}\mathrm{As}$/GaAs heterostructures.

Another property that hinges on composition is the lattice constant since for $\mathrm{In}_x\mathrm{Ga}_{1-x}\mathrm{As}$ layers, it follows Vegards' law [76]. The elastic strain builds up as the square of the lattice mismatched during film growth. Evidently, the higher content of Ga in the deposited layer, the lower the strain accumulation. Therefore, the composition of the deposited material plays a crucial role in modulating the strain and consequentially, the size, shape, and composition of the 3D islands, as well as in determining when the SK transition takes place.

Although strain is of mayor importance, there are other active elements involve in the growth process. Island growth is also influenced by temperature, flux rates, III-V flux ratio, surface reconstruction and crystallographic orientation of the GaAs substrate [77]. In the quarry of a clearer picture of QDs nucleation and evolution, the relevance of all this factors must considered.

3.3.1 The substrate: GaAs(001)

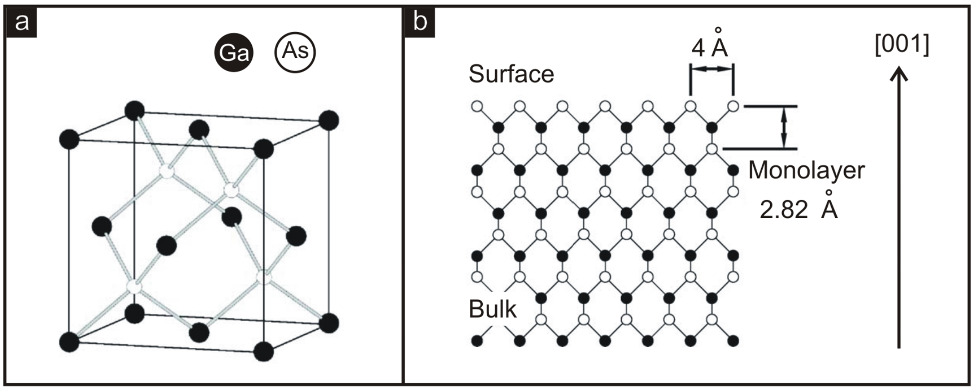

Fig. 3.5: a) GaAs zinc-blende unit cell. b) Diagram of the GaAs zinc-blende structure in the [001] direction. The spacing between layers is 1.41 Å and for the atoms on the unreconstructed bulk terminated surface is 4 Å.

GaAs(001) is the starting surface for the majority of optoelectronic devices. It has being epitaxially grown for more than 40 years and a vast experimental and theoretical work has been devoted to the understanding of this compound semiconducting surface [78].

GaAs is a zinc-blende semiconductor with a direct band gap of 1.424 eV and a lattice constant of 5.65 Å. In the [001] direction, the crystal is formed by alternating planes of Ga and As, separated by 1.41 Å. The (001) surface occurs in a variety of structural forms, depending on its stoichiometry. It is a polar surface and can be terminated by either Ga or As atoms, that forms a square (1x1) lattice when unreconstructed (Fig. 3.5). A monolayer of the GaAs(001) surface is a 2.82 Å thick Ga-As or As-Ga bi-layer.

As the most studied III-V system, GaAs homoepitaxy has proven to be a difficult starting point for the atomistic description of epitaxial growth of arsenide compound semiconductors. The complication emerges form the intricate interaction of As and Ga during adsorption/desorption and diffusion processes. Arsenic exhibits a preferential adsorption at surface sites with locally enhanced cation population and there is a difference in the sticking probabilities of As_2 and As_4 molecules.

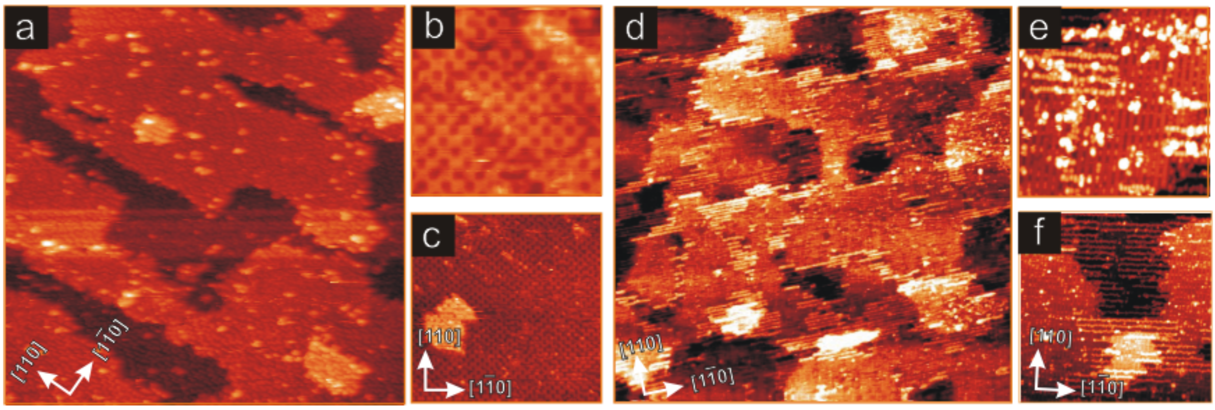

Fig. 3.6: On the left: As-rich GaAs(001) surface showing a c(4x4) reconstruction. Image sizes: a) 60 nm x 60 nm, b) 10 nm x 10 nm and c) 25 nm x 25 nm. Images b) and c) taken from [52]. On the right: Ga-rich GaAs surface showing a mixed c(8x2)+(6x6) reconstruction. Images size d) 300 nm x 300 nm, e) 40 nm x 40 nm and f) 80 nm x 80 nm. As-rich samples were grown by MBE, while Ga-rich samples were grown by Ar-sputtering and annealing cycles. In all cases, the tunneling condition were V_B= -3 V and I = 1 nA.

Furthermore, contrary to the case of single element surfaces, for compound semiconductor such as GaAs and InAs, the free energy depends on two chemical potentials. This adds another difficulty to the growth description since there are a large number of reconstructions with considerable atomic rearrangements, whose structures are determined by subtle changes in the growth parameters. Experimentally, the substrate temperature and As flux or BEP during growth are used to explore the rich chemical potential landscape of the GaAs(001) surfaces [79].

As-rich surfaces are obtained (Fig. 3.6 a-c) in the temperature range between 300^{o}C and 700^{o}C under high As flux, while Ga-rich surfaces can be grown at high temperatures ($<$ 600^{o}C) under low As flux or by sputtering-annealing without As overpressure (Fig. 3.6 d-f).

As-stabilized surfaces are preferred for optoelectronic applications [78]. The (2x4) is the foremost used surface for growing high-quality GaAs epilayers. Ga stable surfaces are more difficult to study, because any Ga excess tends to form free metallic clusters. For these reasons, crystallographic and electronic models have been mainly formulated for the arsenic-rich reconstructions, in particular for the (2x4) [78] and c(4x4) surfaces [80].

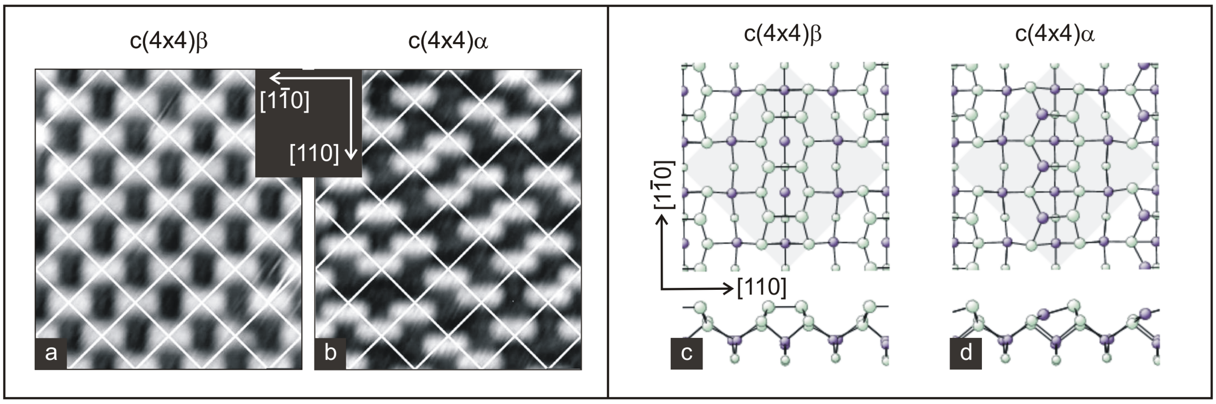

Fig. 3.7: Filled-state STM images of the GaAs(001)-c(4x4) surface prepared under: a) As_4 flux, corresponding to Ga-As dimer structures and b) As_2 flux, for As-As dimer structures. Images taken from [81]. Structural models of the GaAs(001)-c(4x4) reconstruction: c) model consisting of the conventional three As-dimers and d) model for the Ga-As heterodimers (hd) surface. Shaded rectangles indicate the surface unit cell. Side views along the [110] direction are given in the lower panels. Images taken from [82]

In the case of the deposition of InAs over GaAs(001), there is an upper limit for the growth temperature given by the In desorption temperature (520^{o}C). At this temperature regime (<520^{o}C) under high As flux, the GaAs(001) surface tends to the c(4x4) reconstruction. As a consequence, the majority of the work performed on InAs QDs involved the c(4x4) as the substrate surface.

The c(4x4) surface with the highest As coverage, so called c(4x4)β, is formed by a unit mesh of three As-As dimers oriented along the [1$\bar{1}$0] direction (Fig. 3.6 b and c). Recently a new structural model for the c(4x4) consisting of three buckled Ga-As heterodimers (c(4x4)α) was established by using first principles calculation in combination with X-ray Photoemission Spectroscopy (XPS) (Fig.3.7 b and d) [81]. The mixed dimer phase is found to be kinetically stable when the (2x4) is cooled under As_4 flux. Under As_2 flux, it is metastable and appears for a temperature range of 490^{o}C - 510 ^{o}C [80].

For the QDs samples studied in this work, the GaAs surface was prepared upon cooling the (2x4) surface under a constant As_4 flux, therefore, the starting surface used as substrate corresponds to the mixed dimer phase c(4x4)α.

Extensive theoretical work has been developed contributing to a comprehensive interpretation of the different observed microscopic details of GaAs growth ([83] and references therein). First-principles calculations have provided a basis for the study of the complex processes involved during GaAs homoepitaxy, such as adatoms diffusion barriers or the reaction of Ga with

As dimmers on the surface [84]. For instance, calculated surface phase diagrams of GaAs, for growth conditions ranging from As-rich to very Ga-rich stable reconstruction have been already developed (Fig. 3.8). These calculations have been extended to study the effect of strain in the surface energetics of GaAs as a function of the As chemical potential μ_{As}. Likewise surface diagrams are available for InAs, providing a better understanding to the first stages of the formation on the wetting layer, as it will be discussed in the following sections.

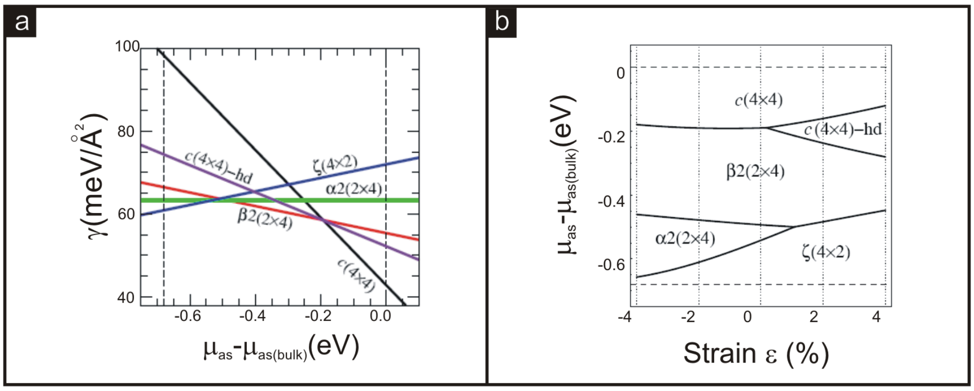

Fig. 3.8: a) Calculated equilibrium phase diagram of the GaAs(001) surface. b)Diagram of surface phase of GaAs(001) as a function of the As chemical potential μ_{As} and isotropic strain ε [85].

3.4 The wetting layer: InAs/GaAs(001)

If the characterization and description of the GaAs surfaces structures and their homoepitaxial growth posed a big challenge for theoreticians and experimentalist, the characterization and understanding of the different stages of the growth of InAs on GaAs turned out to be a bigger conundrum.

The formation of a wetting layer (WL) is inherent to the SK mode and strongly influences the growth of QDs, by acting on the nucleation and diffusion of adatoms even before the onset of 3D growth. It also plays a role in the carrier confinement and optical relaxation processes, since it may act as a quantum well coupled to the QDs, formed after the necessary GaAs capping process (Fig. 3.9).

The formation of the WL in the InAs/GaAs(001) case deviates from the classical SK picture, as it is not a pure InAs layer but rather forms an In$_x$Ga $_{1-x}$As alloy. Intermixing mediates the lattice mismatched, so that the lattice parameter distortion is less than it would be required to accommodate the pure binary alloy.

The strain energy stored in the epilayer increases linearly with the WL thickness. The precise value of the critical thickness depends on several factors, such as temperature, deposition flux or As BEP. Values reported in literature for the critical thickness vary from 1.2 to 1.8

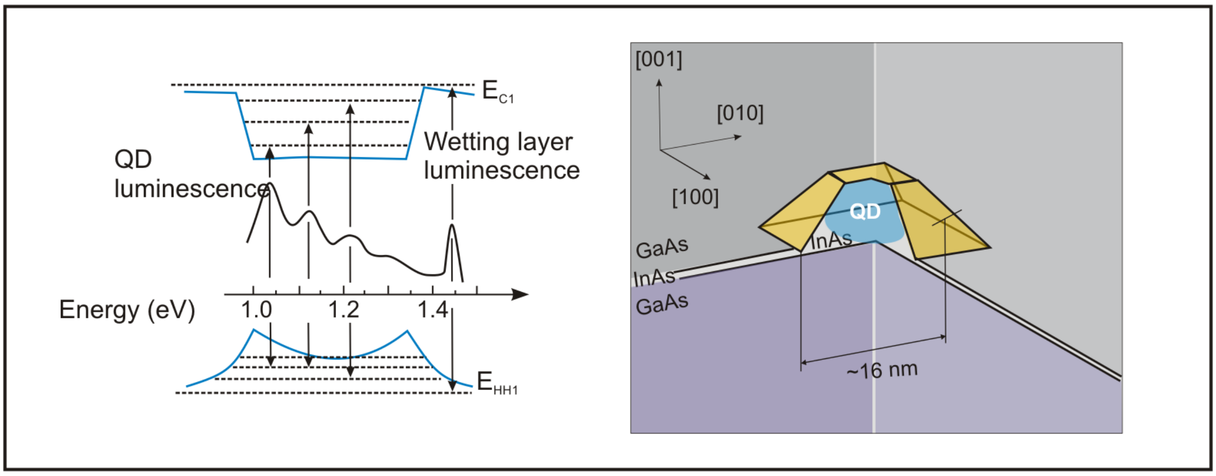

Fig. 3.9: Schematic representation of the quantum well emission of the wetting layer coupled to the optical response of the QDs.

ML [86].

3.4.1 Wetting layer structure: phase surface diagram

The hallmark of the the InAs/GaAs(001) WL growth is the rich change in structure with the growth parameters due to alloying. Representatives STM images of the WL layer are shown in Fig.3.11 a) for submonolayer deposition (0.3 ML of InAs), b) for a coverage close to θ_c (1.65 ML) and c) after the nucleation of 3D islands (1.8 ML). Samples were grown at 500^{o}C with a growth rate of 0.008 ML/s, under a constant As BEP pressure of 1 x 10^{-6} mbar.

The WL intermixing had been studied extensively with different techniques such as RHEED [87], XPS [88], STM [87] and Reflectance Anisotropy Spectroscopy (RAS) [89]. Combining RHEED and STM characterization, Belk et al. [87] established a detailed surface phase diagram of the WL as a function of growth temperature and InAs coverage, shown in Fig. 3.10.

Although this surface phase diagram was constructed for an specific InAs flux rate (0.1 ML/s), it represents indeed a very general description, frequently used as a reference. Small discrepancies can originated from kinetic effects due to different deposition rates, different As BEP or simply due to the often encountered problem of a difference in the calibration temperature for different MBE systems.

At the low substrate temperature ($< 450^o$C), for small InAs coverage (< 0.5 ML), the Indium spatial distribution is very uneven (Region 1). Small domains of In$_x$Ga$_{1-x}$As alloy are formed coexisting with the pure GaAs c(4x4) substrate structure. These alloyed domains show predominantly a (1x3) reconstruction. Upon further deposition, the domain size increases, enlarging the surface with (1x3) structure, until the entire WL exhibits this reconstruction (Region 4).

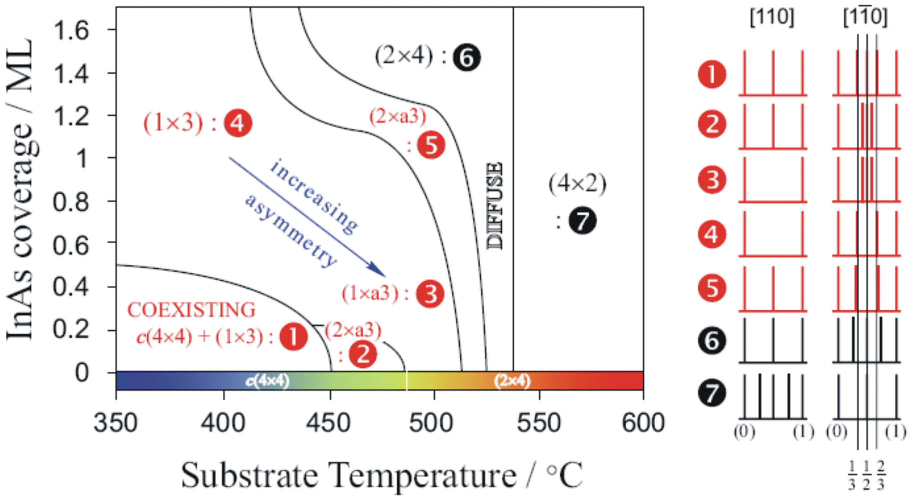

Fig. 3.10: A schematic illustration of the surface reconstructions observed by RHEED during the WL formation of InAs on GaAs(001) as a function of nominal InAs coverage and substrate temperature according to Belk et al. [87]. The letter 'a' indicates the presence of asymmetric patterns.

With increasing temperature (between 420^{o}C and 520^{o}C) and submonolayer coverage, the WL becomes disordered (regions 2 and 3), showing only local ordering with a basic periodicity of 1x, 2x in the [1$\bar{1}$0] direction, while along the [110] the periodicity can be 3x, 4x. These incommensurable regions are identified as asymmetric in Fig. 3.10 (see also [90]). For coverage higher than 1 ML, the surface tends to the (2x3) or (2x4) structure (regions 5 and 6).

For temperature higher than 520^{o}C, the surface exhibits a cation-rich (4x2) reconstruction, which is associated with Indium segregation and it is probably a surface very diluted in Ga (region 7).

From our experiments, we observed that at the initial stages of the WL growth, the (1x3) domains can be easily distinguished from the 'brickwork' pattern of the c(4x4) substrate reconstruction (Fig. 3.11 a-b), similar to what is refereed as Region 1 in Fig. 3.10. Indium starts to incorporate into the existing layer. It is more suitable for Indium to accommodate in step edges and defects, displacing Ga and distorting locally the substrate. The larger bonding energy of Indium to Indium relative to that of Gallium to Indium, would tend to produce Indium adatoms aggregation on the growing surface [91]. Inasmuch, this will favor the incorporation of a second Indium atom on top of another Indium atom, since the lattice is already expanded at that site. Some of this small Indium cluster can be seen in Fig. 3.11b over the intermixed domains at this coverage.

Experimentally it has been found that a complete layer structurally different from the substrate appears already after the deposition of 1/3 - 2/3 ML of InAs, depending on the temperature [88, 87]. At this stage the WL has already become entirely an alloyed surface, similar to

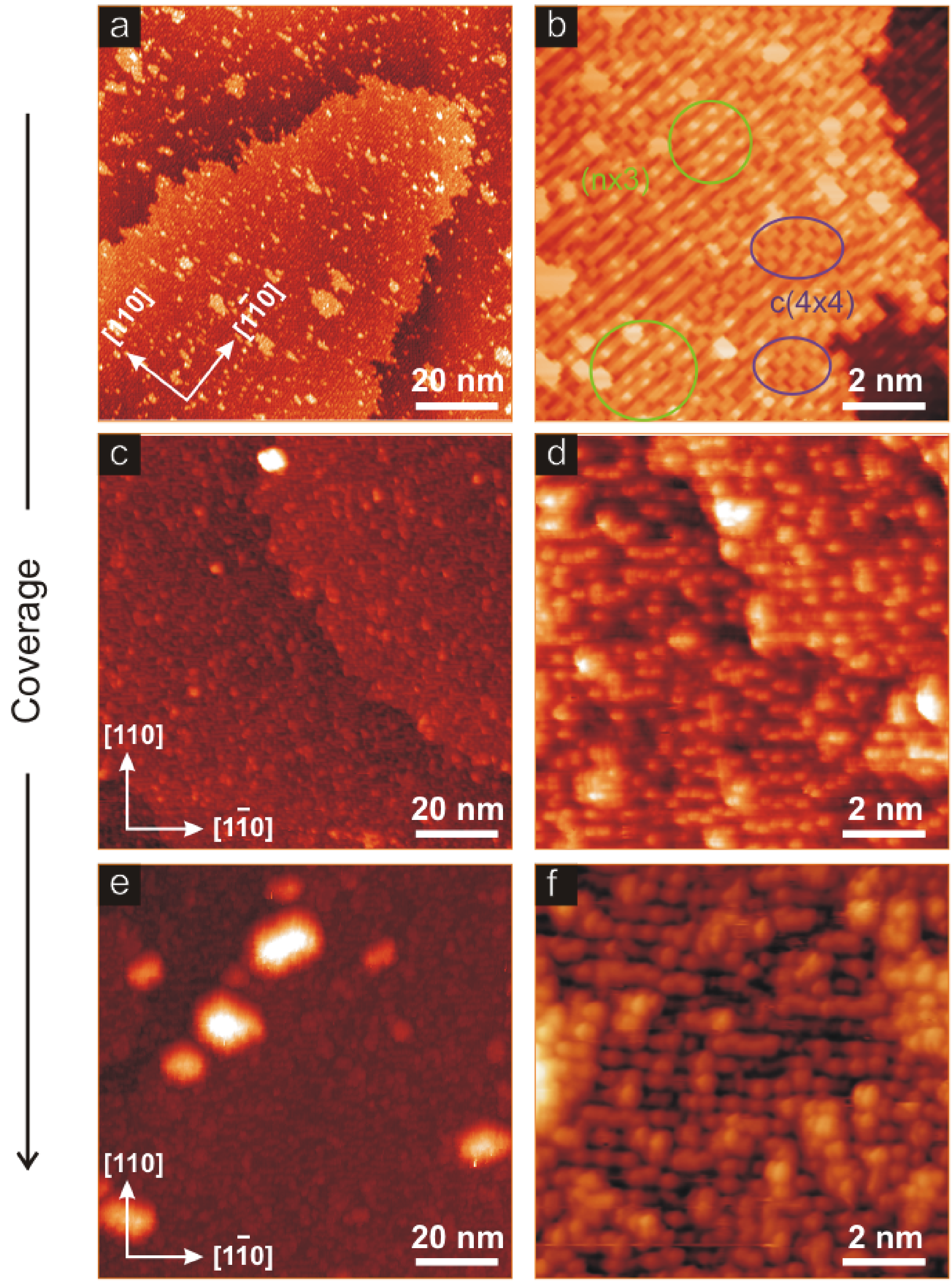

Fig. 3.11: Filled state STM images of InAs deposited on GaAs(001)-c(4x4), with tunneling condition of V$_B$ = -3 V, I = 1 nA. InAs submonolayer deposition is shown in a) for a coverage of 0.3 ML. Image b) shows details of the coexisting (1x3) domains and the c(4x4) substrate structure. Images of the disordered WL produced close to the 2D-3D transition are shown in c) and d) for a coverage of 1.65 ML and e) and f) for a coverage of 1.8 ML. Images d) and f) represent the wetting layer after the formation of the islands. Left images size is 100 nm x100 nm. Right images size is 20 nm x 20 nm.

Fig. 3.11 d and f. The surface is formed as a mixture of diverse periodicities (1x2), (1x3), (2x4), etc. In spite of the different InAs coverage (in both cases higher than 2/3 ML), both surfaces are alike and they still exhibit a similar reconstruction (Regions 5 and 6 in Fig. 3.10).

3.4.2 Alloyed wetting layer: the role of strain

For As-stabilized In$_x$Ga$_{1-x}$As alloyed surfaces, (nx3) periodicities have been reported with X-ray Diffraction (XRD) [88] and more recently by STM studies [85]. Interestingly, none of this (nx3) structures fulfilled the electron counting rule (ECR), which is an established criteria for determining allowed semiconductor surfaces structures.

Furthermore, Savage et al. [88] observed the formation of a commensurate (2x3) reconstruction of the In$_x$Ga$_{1-x}$As layer by X-ray diffraction, only for an Indium concentration of x = 2/3. Incommensurate (2xn) phases were observed for lower In concentrations and were attributed to faulted sequences with Ga-enriched content. Other groups have also supported the idea that a change in the structure towards a (nx3) surface is observed, only when a very defined amount of Indium is available on the wetting layer [87, 72].

By means of STM and RHEED, Krzyzewski et al. [92] studied the effect of the initial substrate reconstruction on the formation and evolution of the WL. Differences for the GaAs (001) (2x4) and c(4x4) reconstructions were significant for sub-monolayer InAs deposition, suggesting that the strain effect for this coverage is small. For InAs coverage higher than 0.5 ML, for both reconstructions, a rapid disordering of the GaAs surface through alloying was observed even at low substrate temperatures (480^{o}C), along with a weak (1x3) diffraction pattern. As the InAs coverage was increased towards 1 ML, the strain influence overrode the effects of the initial surface reconstruction. Krzyzewski et al. [92] concluded that strain begins to play a role at 0.7-0.8 ML of InAs, and in such a way that the formation of a uniform alloyed WL is independent of the starting substrate surface.

Using Density Functional Theory (DFT), Kratzer et al [83] calculated the formation energy γ_f of four of the most favorable structures for the WL surface: the (1x3), the (2x3), the α2(2x3) and the (4x3), shown in Fig. 3.12. The calculations were done for As rich conditions and considering a fixed coverage of θ_{In} = 2/3 as suggested from the experiments [88, 93].

The calculated formation energy γ_f, for the (2x3) structural model was found to be very close to the surface energy of the (2x4) surfaces, being more stable for As-rich condition (See Fig. 3.13). For As-poor condition, the α 2(2x4) turned out to be the most favorable reconstruction.

The low γ_f and the strong tendency of dimerization of the (2x3), makes it plausible to be a stable surface in spite of violating the ECR. Likewise, the change in the γ_f under applied isotropic strain ε showed that the lowest γ_f corresponds to the (2x3) reconstruction. On the basis of these calculations, Kratzer et al. single out the (2x3) reconstruction as a strain-stabilized sur-

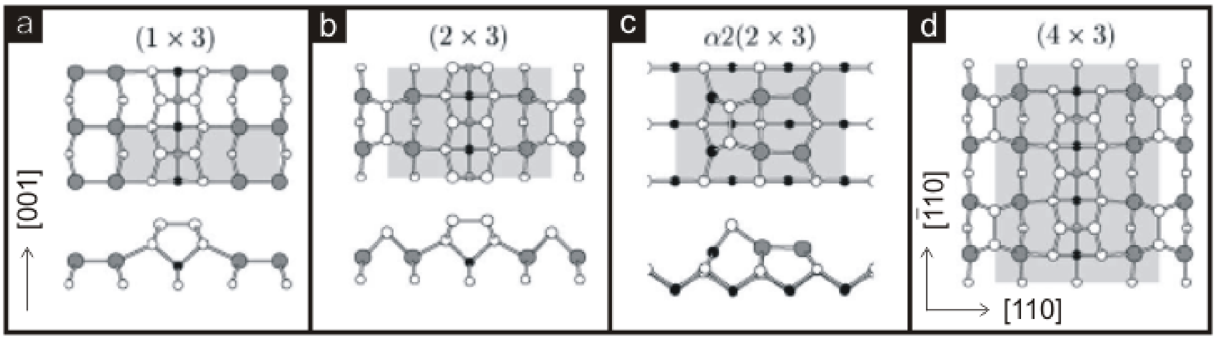

Fig. 3.12: Structural models for the commensurate (nx3) reconstruction of the $In_xGa_{1-x}As$ surface, after [83]. Unit cells are represented as grey polygons. The atomic arrangement is indicated for atoms in the topmost four atomic layers. The lower panels in a)-c) indicate the side views. The side view of d) is identical to that in b). In atoms are depicted in grey, Ga atoms in black and As atoms in white.

face that can be regarded as the main subunit preferable of the $In_xGa_{1-x}As$ film under As-rich conditions.

For thicker films (θ_{In} > 1 ML), similar DFT calculations [85] suggests that for most conditions, a structural transformation from the (nx3) surfaces towards the (2x4), occur prior to the 2D-3D growth mode transition, in accordance with the experimental phase diagram of the WL, shown in Fig. 3.10, for the temperature regime, where the (2x3) is present ($\sim$ 450-520^{o}C).

Experiments and calculations alike seem to indicate that strain effects are predominant when a specific stoichiometry of the substrate has been achieved (even before the full deposition of 1ML of InAs) and that strained induced intermixing is the driving force for the (nx3) structural transformation of the WL.

It is noteworthy, that only for the GaAs(001), intermixing is observed. On GaAs(111) and GaAs(110) surfaces, In does not incorporate into the substrate but rather remains on top and thus intermixing does not take place. Without the strain mediation of an intermixed WL, strain relaxation occurs through the nucleation of dislocations at the substrate interface, making the SK mode on GaAs(001) the exceptional case [77].

3.4.3 In segregation on the WL

One of the most relevant consequences of the intermixing of the WL is its impact on the diffusion of In atoms. Kratzer et al. [83] were able to estimate the In activation energy for In diffusion on an $In_{2/3}Ga_{1/3}As(001)$ film. The values obtained through their calculations are summarized in Table 3.1, together with the diffusion activation energies of Ga for homoepitaxy on GaAs(001). Interestingly, the well ordered $In_{2/3}Ga_{1/3}As(001)$ film turns out to be an excellent substrate for In diffusion [85]. The calculated activation energies are highly anisotropic

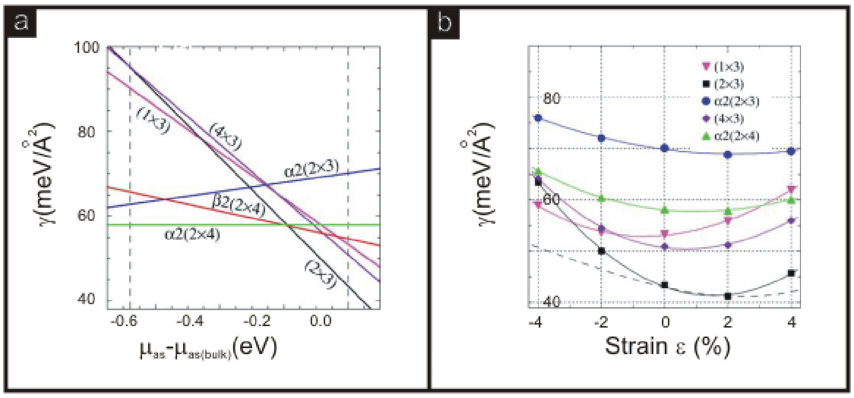

Fig. 3.13: Formation energy of the different reconstructions of the $In_{2/3}Ga_{1/3}As(001)$ surface: a) as a function of μ_{As} and b) as a function of the isotropic strain ε with respect to the GaAs substrate. Figures taken from [83].

and substantially lower than for Ga on GaAs(001). The way indium diffuses controls to a big extent the microscopic mechanism of nucleation of the 3D islands over a strained film [94, 85].

Moreover, it is well known that cation segregation plays an important role in the growth of III-V alloys. Several models have been developed in order to account for the high segregation efficiency of III-column materials. With the use of in-situ characterization techniques Moison et al. [91] interpreted their results with classical segregation theory. They attributed the effect to different chemical potentials of In and Ga atoms on the growth surface and suggested an exchange reaction of In and Ga between the surface layer and the underlying layer, assuming thermodynamic equilibrium. Substitutional segregation remains a valid picture even though limitations to this model were found for high growth temperatures ($\leq 500^oC$) and In concentration above 11%.

Muraki et al. [95] formulated a phenomenological segregation model that suggests that the concentration of In at the surface exceeded 1 ML. A similar observation was made by Garcia et al. [96], by monitoring in-situ the accumulation of stress acting on a GaAs substrate during MBE growth of InAs. They argued that at the usual growth temperatures ($\sim$ 450-500^oC), 50% of the deposited In does not incorporate into the WL during the first part of the growth. A

Adatom/substrate	Direction	
	$[\bar{1}00]$	[110]
Ga/Ga(001)-β2(2x4)	0.7	0.8(eV)
$In/In_{2/3}Ga_{1/3}As(001)$-(2x3)	0.13	0.29

Tab. 3.1: Activation energies for surface diffusion of Ga for homoepitaxy on GaAs(001), and of In for heteroepitaxy on a $In_{2/3}Ga_{1/3}As(001)$-(2x3)surface, as the one shown in Fig. 3.12b

reduction in stress was observed for a deposition close to the value of the critical thickness for islands formation ($\sim$ 1.4–1.6 ML).

Cullis et al. [97] developed a detailed description of the SK growth mechanism taking into account In segregation on the WL. The model also assumes exchange of the group III species between the top two layers during growth, producing a deviation of the actual In concentration and the deposition flux concentration. Following the work done by Walther et al. [98], they computed the In segregation for the deposition of a very diluted $\mathrm{In}_x\mathrm{Ga}_{1-x}\mathrm{As}(001)$ alloy (x = 0.25). They found out that accumulation of In increases rapidly and that for only $\sim$ 1 nm of deposited material, the In concentration exceeded 40%. The In content increased as deposition proceeds, up to a saturation value estimated to be around 80-85% for layer thickness of $\sim$ 2.5 nm. Since increasing In concentration results in an increase of strain, the critical In concentration can be understood in terms of the strain energy necessary to induce the 2D-3D transition, defining per se the WL critical thickness.

Very recently Tu et al. [99] proposed a continuum model for studying the critical thickness formation for the heteroepitaxy of Ge/Si(001). This accounts explicitly for the alloy formation during growth and the outcome coincides with that by Cullis et al. [97] for InAs/GaAs(001). The key factor controlling the transition is the continuous increased of the In surface composition during growth.

3.4.4 Nucleation: precursors, embryos and pyramids.

Albeit the recent improvements in the comprehension of the complex phenomena of self-organization, there is not still sufficient understanding of the precise microscopic mechanism operating at the growth transition. As a matter of fact nucleation of the self-organized 3D islands stands as one of the long lasting questions about the formation of semiconductor QDs.

From the vast number of studies addressing this issue, the in vivo STM study performed by Tsukamoto et al. [100] is remarkable. Using an STM placed inside the MBE growth chamber they closely followed the 2D-3D transition. An ultralow growth rate of 2.5 x 10^{-4} ML/s was used to enable time resolved sequences of InAs deposition at a substrate temperature of 430^{o}C. They concluded that only a fraction of the deposited In is incorporated into the WL, leading to a high density of mobile In adatoms and a WL with small domains of fluctuating alloy composition. This finding validates the picture of high In segregation during growth, conveyed in former studies and the subsequent theories discussed in the previous section.

The initial stage of island formation was observed in the sequence for InAs coverage between 1.65 and 1.70 ML, as shown in Fig. 3.14. First, at a coverage of 1.67 ML, very small islands with heights of 1 ML and width of $\sim$ 1.2 nm start to nucleate, followed almost simultaneously by the growth of 2–3 ML high islands. These islands quickly developed into fully

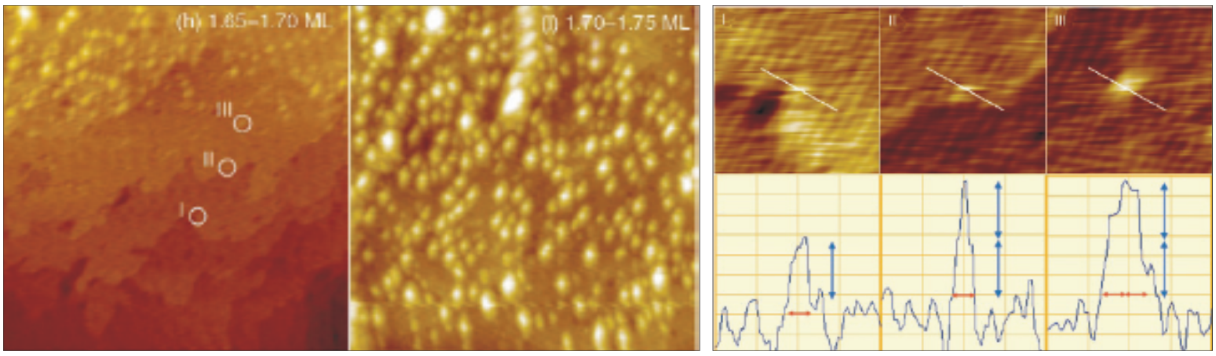

Fig. 3.14: STMBE images at a coverage range between h) 1.65–1.70 ML and i) 1.70–1.75 ML. The size of the images is 150 nm x 150 nm and they were completed in an interval of 0.05 ML. Magnified STM images of 15 nm x 15 nm are shown in insets I, II, III. The cross sections in the lower row correspond to the white lines in the insets. The vertical blue scale bar equals 1 ML (.28nm) and the red scale bars to a width of a unit mesh ($\sim$1.2 nm). Image taken from [100]

formed 3D islands. Tsukamoto et al. suggested that within the disordered WL small Ga-rich clusters act as an area of stronger bonding and hence as a preferential nucleation site, similarly to what was reported for the growth of Si/SiO$_2$ with kinetic monte carlo (kMC) simulations [94].

Based on the stated above and looking for a better characterization of the initial stages of QDs growth, we traced the initial stages of deposition of InAs/GaAs(001) by means of in-situ STM with the idea to provide more information about the microscopic features of the early stages of 3D InAs islands growth. As for all processes involved in the growth and evolution of these systems, nucleation depends greatly on the growth parameters and, for this reason, the studied samples were grown at low deposition rates (0.008 ML/s) under an As$_4$ BEP of 8x 10^{-6} mbar and at a substrate temperature of 500^{o}C. This was done with the attempt to provide growth parameters close to thermodynamic equilibrium conditions [74].

In a typical experiment, the samples are grown by MBE and then transferred with the aid of a vacuum suitcase, to the STM chamber for analysis (for details refer to section 2.5). Data collected in this way can be regarded as „snapshots “ of the dynamic processes occurring during growth. Although it is clear that post-growth annealing induces changes, it has been shown that with appropriate quenching protocols the growing surface „freezes “ for further study without significant changes [101]. In our case the quenching rate is of $\sim 1^0$C/s and the sample is kept under As pressure until it cools down to room temperature, preserving the surface morphology, therefore the island's sizes and shapes are still representative „samples “ of what actually is present in real time growth.

Figure 3.15 shows the change in the morphology for different InAs coverages. For a coverage close to the 2D–3D transition, very small 3D islands of less than 2 nm high begin to form as soon as the critical thickness (θ_c = 1.6 ML) is exceeded, as presented in Fig. 3.15a, for a coverage of θ = 1.7 ML [102].

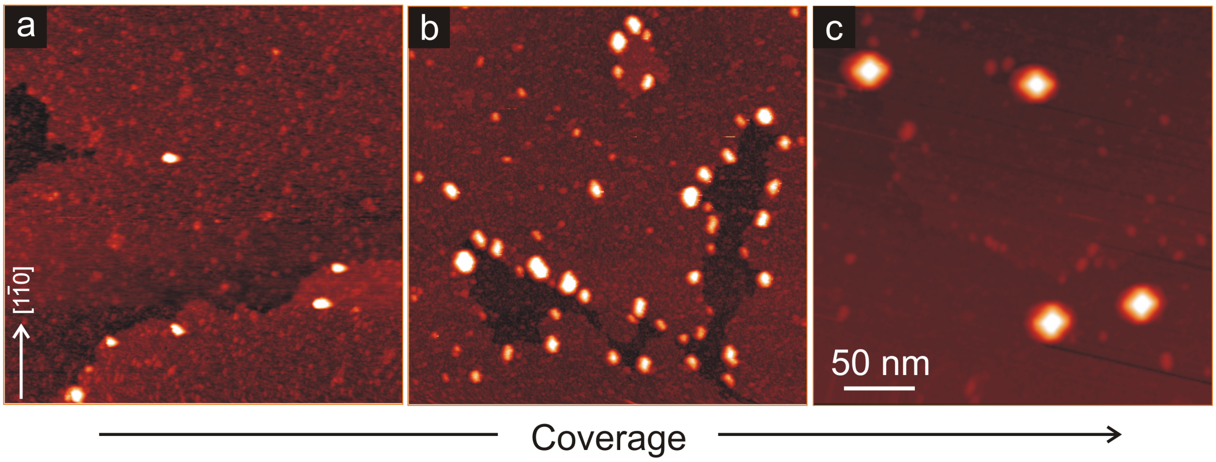

Fig. 3.15: Surface morphology as a function of InAs coverage during InAs/GaAs(001) growth. The corresponding coverage is: a) 1.7, b) 1.8 and c) 1.9 ML.

As the deposition continues (θ = 1.8 ML), the islands become larger and slightly elongated (Fig. 3.15b). We have identified these islands as huts and pyramids, in resemblance to the classification made previously to Ge/Si(001) islands [102]. Pyramids have an aspect ratio[1] of 0.2–0.3 with heights around 2–4 nm and are bounded by four $\{137\}$ facets. If the deposition increases further (θ = 1.9 ML), big multifaceted islands, or so called domes, with aspect ratio of 0.4–0.5 and heights around the 10–15 nm, start to appear (Fig. 3.15c) [103]. In the following chapter these two type of islands will be fully address, so no further details will be given here. It is rather on the very small islands, that we will focus our attention.

In the following, some images will be display using the negative local surface slope (LSS) for enhancing morphological details, or a combination of the LSS and the local height, to enhance small features. By displaying the image with the negative surface slope the extended light or dark regions correspond to shallow or steep facets respectively. For more details, please refer to Appendix A.

The smaller islands, often referred to as precursors, are highly irregular [104]. We observed that some of them have an almost two-dimensional character and are constituted by few ML high platelets as can be seen in Figs. 3.16a and 3.17a. Some are genuinely 3D, although not possessing a well-defined shape (Fig. 3.17c and Fig. Fig. 3.18a), and others possess a shape very similar to those of pyramids or huts, as the islands in Fig. 3.18b, but with slightly smaller aspect ratios ($\sim$ 0.15–0.19). The differences between precursors and pyramids can be seen more clearly from the cross sections display in Fig. 3.17 b–c and e–f.

Fig. 3.17e displays a typical triangular profile corresponding to a pyramid. One of the hallmarks of pyramids are their $\{137\}$ facets, which form a contact angle of 24^o with the WL. To

---

[1] The aspect ratio is defined as the height divided by the square root of the base area and is a common choice for islands classification.

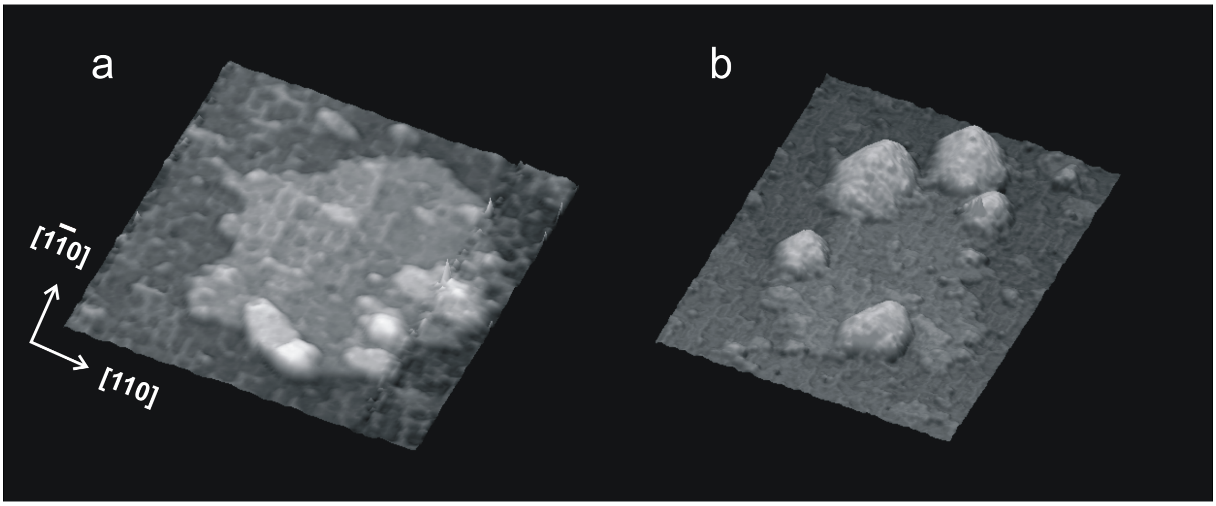

Fig. 3.16: 3D view of magnified STM images showing two distinct stages of nucleation. a) Shows quasi 3D structures at the early stages of InAs deposition (θ = 1.7 ML), while b) shows the coexistence of embryos and pyramids for a higher coverage (θ = 1.8 ML). Image sizes are a) 38 nm x 49 nm and b) 56 nm x 68 nm, respectively. The grayscale in both cases corresponds to a combination of the negative LSS and the surface height, used to highlight morphological features. These images are 3D representations of Fig. 3.17 a) and d).

emphasize this inclination, dotted lines rotated $\pm$ 24^o with respect the the horizontal axis, have been drawn next to the profiles. Platelets of few ML height with 3D protrusions on top can be recognized (See Fig. 3.17a). The asymmetry these platelets is reflected in their profiles, on one direction a rounded cross section can be spotted (Fig. 3.17c), whereas on the other, more regular sidewalls can be observed (Fig. 3.17b). Similarly, the more developed precursors exhibits somehow a more sharper profile (Fig. 3.17f). It is interesting to note, that the inclination of the precursors facets, are not quite the same as for the pyramids, no matter how well defined they seem to be. To analyze in detail the evolution of the slope distribution of the precursors, we have employed the facet plot analysis (FP) to compute slope histograms, as described in Appendix A. These 2D histograms represent the frequency at which values of a certain LSS appear in the STM images. In this way, all the points associated with the same surface orientation contribute to the same spot in the FP. From each spot in the FP, the facet orientation can be traced back, since it is determined by the distance and angular position with respect to the (001) center of the plot.

Three of such FPs can be found in Fig. 3.18. The slope analysis was performed using a piece of Fig. 3.15b. Similar FPs for can be obtained for any of the different coverages studied here. Even in the case where dome islands are formed, precursors as those analyze here can be found.

Each FP corresponds to an specific range of aspect ratios. The FP for islands with aspect

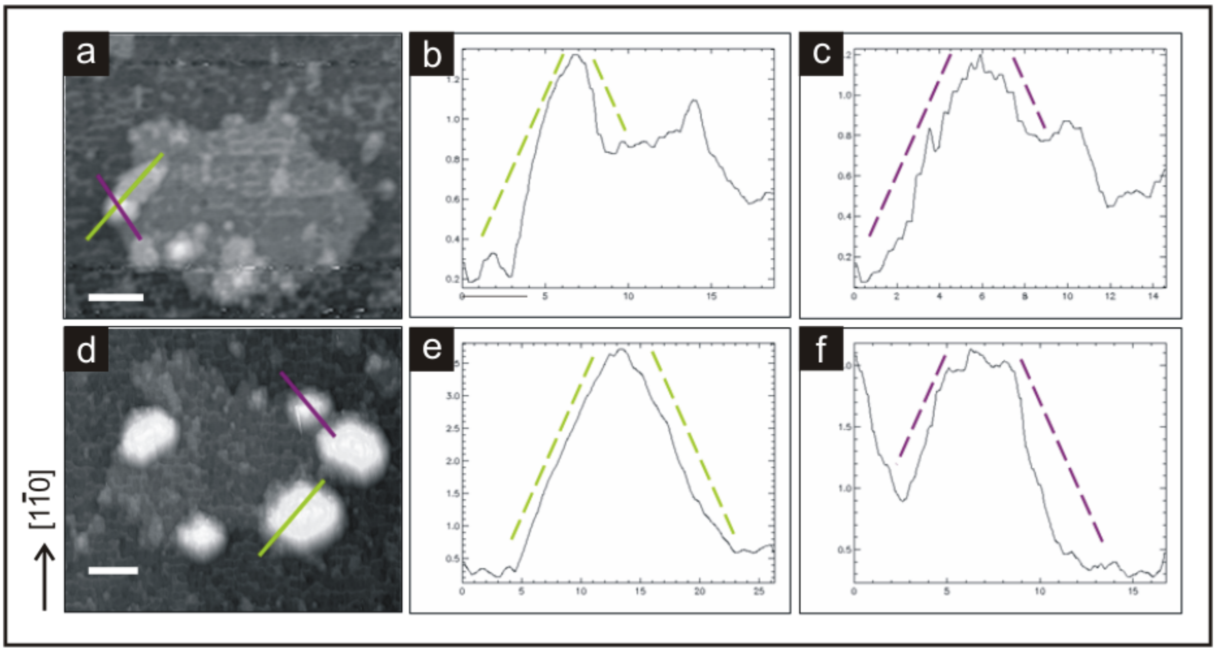

Fig. 3.17: In the first column, magnified STM images are shown for a coverage of a) θ =1.7 and d) θ = 1.8 ML, for the growth of InAs/GaAs(001). b) and c) display line profiles of the small island marked in a). e) and f) show profiles of the two different marked islands on d). The scale bars correspond to 10 nm. Profile scale are in nm.

ratios smaller than 0.15 is shown in Fig. 3.18d, for aspect ratios larger than 0.15 but smaller than 0.2 is shown in Fig. 3.18e, and Fig. 3.18f corresponds to aspect ratios larger than 0.2. Images of the corresponding representative islands are shown for each set in the upper row of Fig. 3.18.

From the FP it is clear that there are two types of precursors. The first types is represented by the very small islands in Fig. 3.18a with no defined shape. These ill-defined shapes translate into an absence of a clear spot in the FP. (Fig. 3.18d). The change from Fig. 3.18d to Fig. 3.18e indicates that the islands suffered a sudden increase in their height compared to their width, and facets with slopes very close to the {137} facets start to nucleate at this stage. We have called these type of islands as embryos [102]. Embryos are partially defined islands, as can be seen from Fig. 3.19. When the aspect ratio reached a value of 0.2, the formation of fully defined pyramids and huts is prompted.

In general, from the previous results and the analysis described above, we can suggest a general picture of the nucleation of the 3D InAs/GaAs(001) islands for growth conditions close to thermodynamic equilibrium. The growth of 3D islands deviates from the ideal SK growth mode due to intermixing. Even for the deposition of pure InAs on GaAs(001), intermixing is produced due to substitutional segregation of the III species. Additionally, the preferential segregation of In over Ga and As, creates an excess of In on the growing surface and a gradient of composition on the deposited layers. The morphology of the intermixed WL tends to a strain-

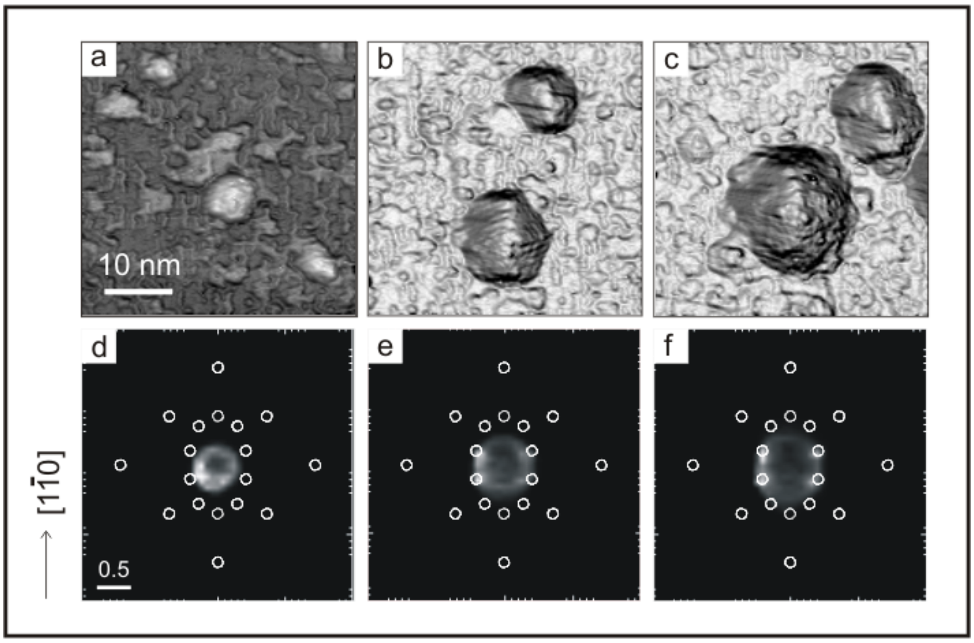

Fig. 3.18: In the upper row: precursors and pyramids with aspect ratios in the range used for the FPs below. In the lower row: FPs selectively evaluated according to aspect ratio. d) corresponds to islands with aspect ratios smaller than 0.15, e) to aspect ratios between 0.15 and 0.2 and f) for aspect ratios larger than 0.2. The islands were grown by the deposition of 1.8 ML of InAs/GaAs(001). The STM image sizes are 40 nm x 40 nm. The grayscale of image a) corresponds to a combination of the surface height and the negative LSS. In b) and c) the negative LSS is displayed.

stabilized (nx3) surface and, in the ideal case, it tends to the (2x3) surface reconstruction. This wetting layer is endowed with lower activation barriers for In diffusion [83]. Consequently, any excess of In available on the surface will be highly mobile [100, 94].

Whenever the In concentration on the top layer reaches a critical value, the 2D-3D transition is triggered due to a critical accumulation of strain. In turn, the excess of In available on the surface enhances mass transport producing a very rapid nucleation of 3D islands during growth, as a mechanism of strain relaxation [72, 90].

Moreover, from the careful inspection of HR-STM images, we can deduce the existence of very small islands, with aspect ratio smaller than 0.15, similarly to what was observed by Tsukamoto et al. [100] for lower temperatures and ultralow deposition rates, and in some cases 2D structures can be also observed as in Fig. 3.19. These precursors represent the first stages of 3D island formation and are preferentially located close to step edges or defects induced by intermixing, since these sites allow the highest strain relaxation and might be characterized by lower migration barriers [94]. We also note that the lowering of the activation barriers for diffusion due to the intermixing of the WL and the high In segregation might enhance uphill diffusion. The nucleation of the dots might start on the upper part of a step to later on cross over it, as appreciated in Figs. 3.16a and Fig. 3.19.

Once the nucleation has started, the very small precursors tend to dissolve in favor of the larger islands. For specific aspect ratios (volumes) $\{137\}$ facets start to appear piece-wisely on the islands, giving rise to partially defined embryos, before transforming into fully developed pyramids (Fig. 3.19). As the size increases the islands transform into well-defined pyramids, bounded by four $\{137\}$ facets.

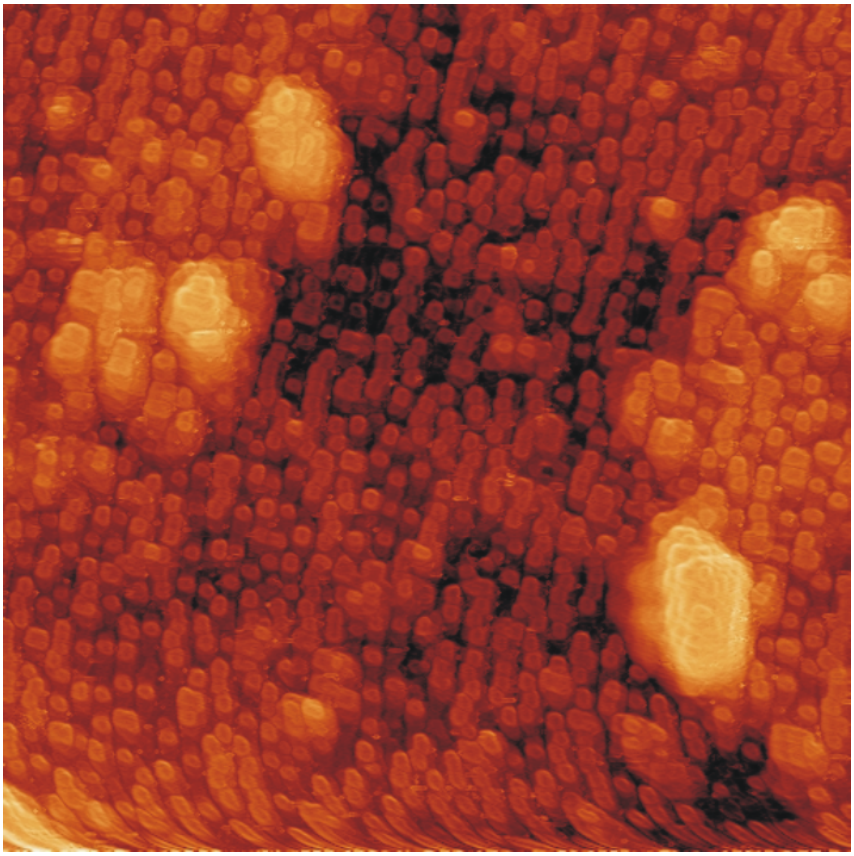

Fig. 3.19: HR-STM image of an InAs embryo, grown after the deposition of 1.8 ML of InAS/GaAs(001) at 500^{o}C. Smaller 2D platelets can also be recognized on the surroundings. Image size 50 nm x50 nm. In this particular case, the positive LSS is used for enhancing the nanometric details of the image.

Chapter 4

On the evolution of 3D InAs strained islands

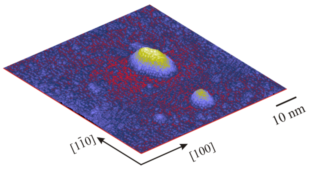

4.1 Self-Organized Quantum Dots

According to Bimberg [13], one speaks of „Self-Organized Quantum Dots“, if QDs with uniform size and shape are formed via optimized growth parameters, inasmuch as this system represents a clear example of spontaneous formation of microscopic order from inherent random size and shape distributions. Self-organized QDs need to fulfill certain requirements in order to be useful for device applications at room temperature. They must be sufficiently small to guaranty the existence of quantized states but sufficiently large to guaranty an energy level separation larger than kT. High density and size homogeneity are of great interest for optimizing the performance of the QDs devices, while for devices that exploit the properties of a single or a well defined number of nanostructures control in position and alignment is fundamental, as is the case for single electron transistors (SET) [20].

The allure of the spontaneous formation of 3D islands turned out to be also the deterrent for homogeneous QDs ensembles. All structural parameters of the 3D islands, such as size, shape, and chemical composition are subject to random fluctuations due to the statistical nature of their growth, where, thermodynamics as well as kinetics are involved. For this reason, the resulting QDs properties are governed by the growth parameters, offering a wide range of possibilities to tune the different degrees of order available for QDs ensembles, i.e., their orientation, density, shape, size, position and composition.

The only possibility to understand how the experimental characteristics of the QDs depend on growth parameters, such as deposition rate, temperature, As flux, etc., is to understand the mechanisms of growth. The optoelectronic properties of QDs are governed by their structural characteristics combined with their composition and strain and in order to develop assertive theoretical models that account for the observed properties, experimental input has proven to be of crucial importance [105]. Hence a thorough characterization of the 3D islands becomes essential.

The actual size and shape of the InAs/GaAs(001) islands remained uncertain for a long time. Sizes in the range of 10 to 40 nm for the islands diameter and heights going from 2 to 10 nm were reported. Pyramids, truncated pyramids, concave lenses, etc. were among the diverse suggested QDs geometries [105]. The fact that both, thermodynamic and kinetic effects are important in determining the structural properties of the self-organized nanostructure, is the most probable reason for the diversity of experimental results. In the following discussion we will provide some insights towards the elucidation of such incertitude.

A further difficulty encountered in the determination of the size and atomic structure of self-organized QDs is that these are not only affected by the growth parameters during the stages of nucleation and growth of 3D islands but also, by the compulsory overgrowth with a larger band gap material. This subject will be discussed in more detail in chapter 5. Here the main focus will be the structural characterization of the intermediate stage towards QDs formation, i.e., the study of the just as-grown islands.

4.2 Bimodal distribution: Pyramids and Domes

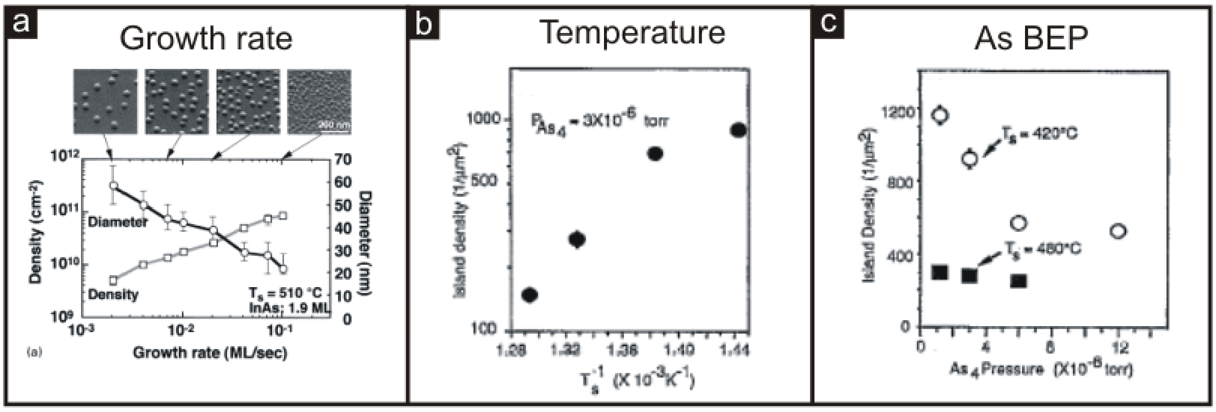

Fig. 4.1: Effect of the growth parameters on the average size and density of InAs 3D islands. a) Base diameter and density as a function of the growth rate. AFM images of samples grown at various growth rates are also shown. Graph taken from [106]. Variation of the islands density as a function of b) substrate temperature and c) As flux. Graphs taken from [107]

The dependance of the size, shape and density of the as-grown islands on growth parameters was the subject of many of the early studies [107, 108, 106]. It was noticed that the density and the average size of the islands was strongly varying with temperature, growth rate and As flux, modifying as well, the optical properties of the resulting QDs.

A breakthrough in the fabrication of QDs was the possibility to obtain narrow size distributions, using appropriate combinations of growth and capping parameters. Several models, some based on minimum energy configurations [109, 110] and some others based on kinetic effects [111], were suggested to account for such narrow size distributions. However, a correlation between the proposed models and the experimental measurements was not fully accomplished.

A very remarkable observation, made by different groups, was a bimodal distribution of the islands sizes, obtained under specific growth conditions [112]. The bimodal size distribution was not restricted to a particular system, it was observed in Ge/Si(001), InAs/InP(001), InAs/GaAs(001) to mention a few [13]. Furthermore, experiments proved that each maximum of the bimodal distribution could be associated to a characteristic island shape (Fig. 4.3).

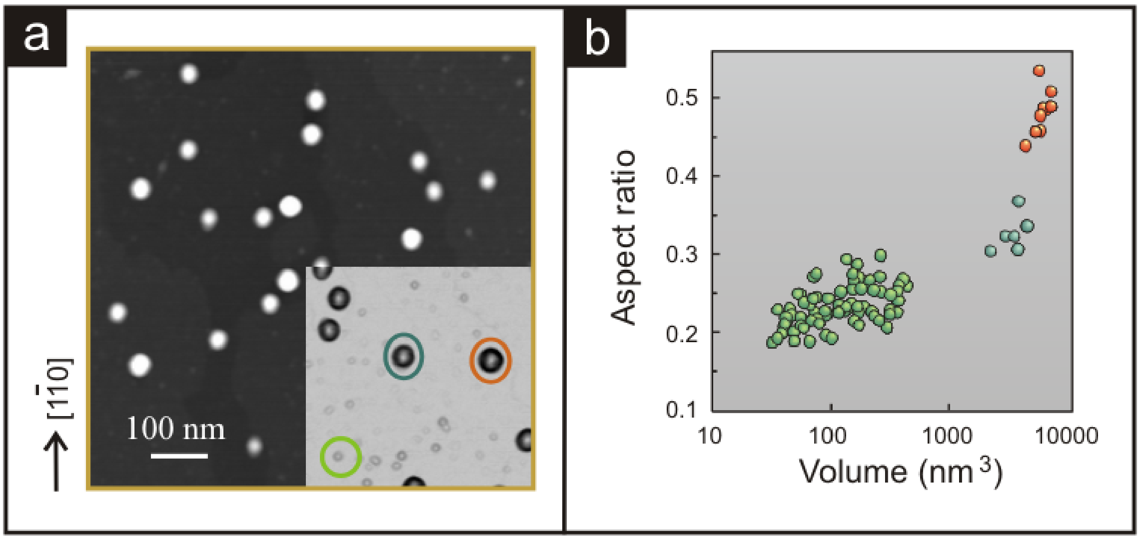

Fig. 4.2: a) AFM topography of an InAs/GaAs(001) sample showing a bimodal distribution of islands. The lower corner of the image displays the negative LSS in order to enhance details. b) Scatter plot of aspect ratio versus volume for a set of three images similar to the one showed in a). Clearly, the islands can be grouped according to their aspect ratio.

Fig. 4.2a displays an AFM image of a characteristic sample showing a bimodal size distribution. The studied samples were grown by the deposition of 1.8 ML of InAs at a growth rate of 0.008 ML/s with a substrate temperature of 500 ^{o}C, under an As$_4$ pressure of 8x10^{-6} mbar. From the image, the coexistence of small and large islands can be appreciated. The right lower corner is display using the negative LSS to enhance the differences among the islands.

A quantitative analysis of the topographies, in which the aspect ratio of each island is plotted versus its volume, shows clearly that the islands divide into two main families with well-defined aspect ratios (Fig. 4.2b). The difference of the islands aspect ratio gives a straight indication that both families have different morphology.

Using HR-STM images, we were able to unambiguously establish the morphology of these two families [113,73]. Previously, this transformation had been reported only in the Ge/Si(001) system [114, 115], but the data of Fig. 4.3 constitute the first evidence that a similar phenomenon occurs also for InAs/GaAs(001). As an analogy with the case of Ge/Si(001) islands [116], we dubbed these two families as Pyramids and Domes [102].

On the upper row of Fig. 4.3, representative STM images of pyramids and domes for the case of InAs/GaAs(001) are shown. Pyramids are bound by one type of shallow facet, while domes are steeper and multifaceted. This can be quantified making use of the FP analysis, as discussed in the previous chapter. A brief description of the FP analysis is also presented in Apendix A.

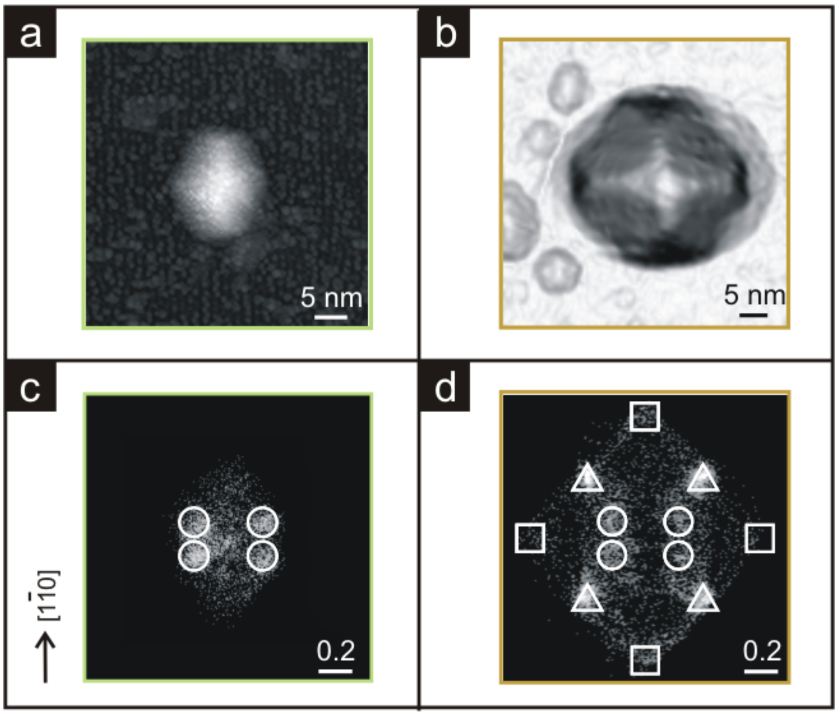

Fig. 4.3: HR-STM of a pyramid a) and a dome b) for the InAs/GaAs(001) system. The grayscale of the pyramid corresponds to the surface height while for the dome corresponds to the negative LSS. In the lower panel, the corresponding FPs are displayed.

The lower row of Fig. 4.3 shows the results of the FP analysis, selectively done for pyramids and domes. Pyramids show four spots located at the same distance from the center of the plot, representing four equivalent and equally extended facets with $\{137\}$ orientation. By applying the FP analysis to the domes, several spots are produced corresponding to $\{137\}$, $\{101\}$ and $\{111\}$ facets.

Based on the high-resolution STM data, it becomes possible to formulate a precise morphological model for the pyramid and dome islands as depicted in Fig. 4.4. This represents the long-sought simple and coherent description of 3D self-organized islands for the InAs/GaAs(001) system. We notice that the emerging picture is directly compatible and unifies a number of previous reports [113, 117, 118, 119, 120]. Moreover, slightly different assignments of the islands facets [121, 122] can also be brought back to this model, when considering the inherent imprecision of the experimental techniques by which they were obtained.

Besides the islands belonging to the main families, a small percentage of the islands represented in the scatter plot of Fig. 4.3 is characterized by volumes and aspect ratios with values in between of those for pyramids and domes. These islands conceal the answer to the anomalous ripening leading to the observed narrow size distributions.

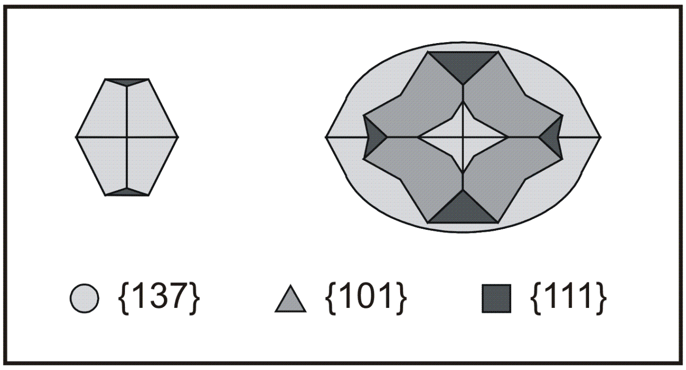

Fig. 4.4: Proposed structural models for pyramids and domes islands for the InAs/GaAs(001) system. Different facets have different gray tones, according to the color code. The symbol code represents the corresponding facets, as indicated in the FPs of Fig. 4.3.

Interestingly, for GeSi 3D islands on Si(001) a rich variety of shapes has been also observed. Recently, a shape transition from shallow pyramidal islands to larger dome islands bounded by multiple facets has been established [123, 119]. This motivated proposals that a similar shape transition should take place in the InAs/GaAs(001) system. Early reports of such shape transition [124, 114] have been very recently substantiated by atomically resolved STM images of InAs 3D island during various stages of their growth [115].

4.3 Structural shape transition: theory and experiments

In the present work, we aim at exploring the nature of the shape transition both experimentally through the characterization of 3D islands during various stages of the transition by STM and by a theoretical analysis of the energetics involved. The calculations are based on a fully equilibrium approach, disregarding any kinetic effects. Although this might not be entirely so, since kinetics can not be excluded a priori, the agreement between experiments and calculations validates the assumptions made. This work was done in close collaboration with Prof Peter Kratzer at the Fritz-Haber-Institut and Dr. Quincy K. K. Liu at the Hahn-Meitner-Institut, in Berlin.

The role of $\{137\}$ facets for the shape of InAs island will be specially addressed in terms of their stability under strain. Moreover, we will discuss the implications of the shape transition for the general view of the island formation as a coarsening process [125, 126], looking forward to the understanding of the experimentally observed narrow size distributions, in the pursuit of controlling the islands characteristics through the growth conditions.

4.3.1 Pyramid-to-Dome evolution: a HR-STM study

For the samples studied in the present section, In was evaporated by MBE at a rate of 0.008 ML/s under an As_4 beam-equivalent pressure of 8x 10^{-6} mbar and at a substrate temperature of 500^{o}C. After cooling, the samples were transferred under ultrahigh vacuum conditions to a STM and there imaged at room temperature. The deposition varied slightly between 1.7 and 1.9 ML of InAs to favor the study of distinct morphologies. The increasing volume prompts the appearance of steepers facets, as can be seen for the $\{101\}$.

A sequence of STM magnifications for the most archetypal types of the different island is presented in the upper row of Fig. 4.5. These images exemplify the transformation path that growing pyramids undergo when they evolve into domes.

While in Fig. 4.5a, a pristine $\{137\}$ pyramid can be recognized, the island in Fig. 4.5b has started to develop a small $\{011\}$ facet in its upper-right side. Fig.4.5c represents a later stage of the shape transition in which extended $\{101\}$ facets have appeared on all sides of the island and two small $\{\overline{111}\}$ facets have formed along $[\bar{1}10]$ direction. Finally, in Fig. 4.5d a mature dome is shown which displays also $\{111\}$ facets along the [110] direction. Only in very few cases we also found domes where the small shallow facets recognizable at the island top and bottom, in Fig. 4.5d these had completely disappeared.

The transition from shallower to steeper facets can be quantitatively followed in the lower row of Fig. 4.5, where the FPs are displayed. Fig. 4.5 e–h show that the shape transformation mainly happens through the successive evolution of $\{101\}$ and $\{111\}$ facets at the expense of $\{137\}$ ones. Fig. 4.5 and the similar results recently published by Xu et al. [127, 128], clearly demonstrate that the pyramid–to–dome transition in the InAs/GaAs(001) systems is almost identical to the corresponding transition occurring during the growth of Ge on Si(001) [127]. This analogy substantiates the claim that very similar microscopic processes must govern the evolution of islands in these two material systems [127, 128].

4.3.2 Pyramid-to-Dome evolution: hybrid approach

The method employed in this work to analyze the energy gain associated with the formation of 3D islands on the wetting layer, was done by employing a hybrid approach. It combines classical continuum elasticity theory and DFT and was developed at the Fritz-Haber-Institut.

The total energy gain is divided into a contribution originated from bulk strain relaxation,

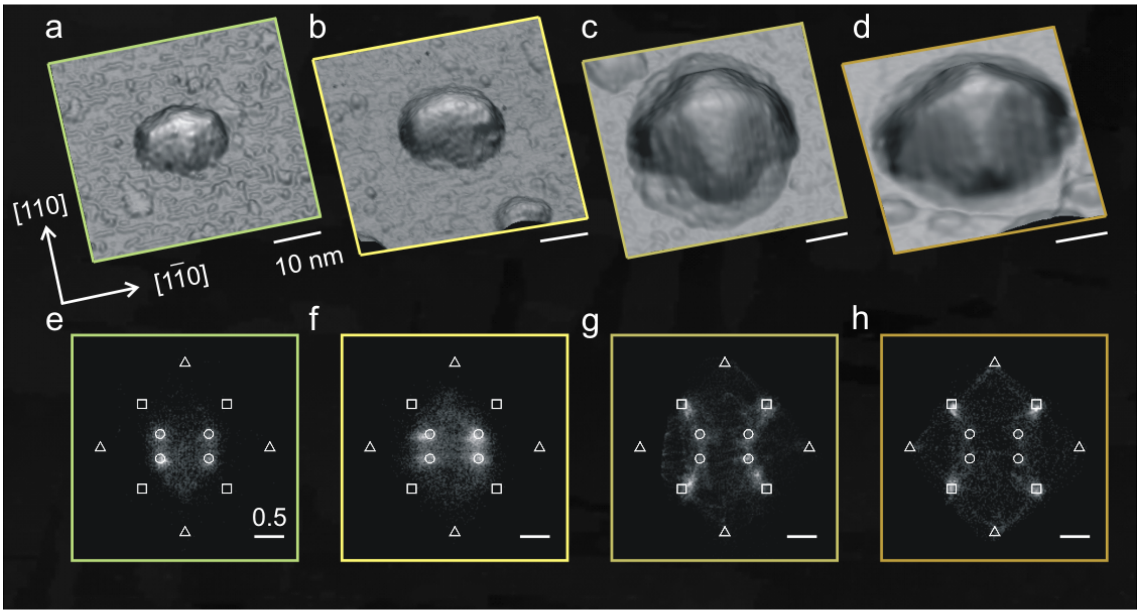

Fig. 4.5: Upper row: HR-STM images of : a) a small pyramid, b) a pyramid starting the shape transformation, where a small steeper $\{011\}$ facet can be recognized on its right side, c) an island after the shape transition with a steeper upper part and d) a fully developed dome-shape island. Lower row: FPs corresponding to the islands shown above. The dense clusters of points in the histogram correspond to the predominant facet orientations, indicated here by the following symbols: $\circ\{137\}$, $\square\{101\}$ and $\triangle\{111\}$.

E$_{relax}$, and terms accounting for the additional formation of island facets, E$_{surf}$, and edges E$_{edge}$, as

$$E_{tot} = E_{relax} + E_{surf} + E_{edge} \tag{4.1}$$

The leading terms are the elastic relaxation energy and the sum over the surface energies of the surface facets. Both quantities depend sensitively on the island shape. The surface reconstructions, the surface energies, and their strain dependance are calculated by DFT and analyzed as a function of the chemical potential.

For islands bigger than ~ 1000 atoms, the strain fields and the elastics energies happened to be well describe by the elastic theory [129]. Therefrom, the long range strain-relaxation in the islands and in the underlying substrate are evaluated by elastic theory applying a finite-element approach. This approach permits the systematic investigation of almost any island shape with less computational effort. It should be emphasize that in each term of Eq. 4.1, the energy difference between a 3D island and a homogeneous planar InAs film of the same volume is considered.

Elastic relaxation: Classical Continuum Elasticity Theory

The treatment of the first term, the elastic relaxation, is done entirely within classical continuum elasticity theory. Results of such calculations for uncapped InAs islands on GaAs substrate have been reported previously [130, 131]. These, together with similar calculations done for InP islands on GaP substrate [132], have demonstrated the applicability of the results to nanostructures. Further details of the theoretical hybrid approach can be found in [130, 131].

The energy of relaxation, E_{relax} of Eq. 4.1, is the difference between the remaining bulk strain energy stored in the island plus the substrate after relaxation, E^{is}_{relax}, and the energy in an equivalent unstrained volume V of a fully strained epitaxial InAs on GaAs, $\epsilon_{film}V$.

The mismatch between InAs and GaAs that gives rise to the elastic energies is

$$\alpha = (a_{GaAs} - a_{InAs}/a_{InAs}) = -6.7\% \tag{4.2}$$

where a_{GaAs} and a_{InAs} are the lattice constants of GaAs and InAs, respectively. The size of the substrate is suitably chosen according to the density of islands seen in the experiments. Periodic boundary conditions were applied to the side-planes of the material in the simulation. The distribution of the eight-node hexahedral finite elements was such that the number of finite elements was increased in the parts of the island where the elastic energy density was large until an estimate of the accuracy of 5% was reached.

For the situation of a homogeneous planar film, the elastic energy per unit volume can be given in an analytical form as

$$\epsilon_{film} = (c_{11} + c_{12} - 2\frac{c_{12}^2}{c_{11}})\alpha^2 \tag{4.3}$$

The explicit values of the moduli of elasticity c11, c12 and c44 of InAs and GaAs can be found in the literature [6,34].

InAs(137): surface energy

The calculation of the second and third term in Eq. 4.1 requires knowledge about the detailed atomic structure, and hence DFT calculations for the surface energies of (reconstructed) surfaces are needed. At present, we neglect the energy of edges in Eq. 4.1, due to lack of knowledge about the atomic reconstruction near the edges. This approximation is justified for not too small islands, as those observed in the present experiments, since the ratio of edges relative to a facet area decreases with increasing island size. For the surface energies, results of DFT calculations within the local-density approximation are available in the literature for low-index facets of InAs [130]. For non-stoichiometric surfaces, the surface energy is a function of the chemical environment, which is described by the chemical potential of arsenic, μ_{As}, in the growth apparatus, corresponding to the experimental choice of temperature and As partial pressure during growth.

In the following, the model considers moderately arsenic-rich conditions, using $\mu_{\rm As} = \mu_{\rm As(bulk)} - 0.2$ eV in compliance with earlier work [133]. This value is close to the experimental conditions for growing the samples shown in Fig. 4.5. In experimental terms, $\mu_{\rm As} = \mu_{\rm As(bulk)} - 0.2$ eV corresponds to InAs deposition at temperatures slightly above the transition of the GaAs(001) substrate from the c(4×4) to the $\beta2(2 \times 4)$ reconstruction [134], and leads to the (re)appearance of a (2×4) pattern on the wetting layer immediately before the 2D–3D growth transition. A detailed study of the structure of the wetting layer by means of DFT calculations [135] shows that the wetting layer, for an In deposition of more than 1.75 ML and moderately arsenic-rich conditions, displays a (possibly disordered) $\alpha2(2 \times 4)$ reconstruction.

To complement the calculated data for low-index InAs surfaces, DFT calculations for the surface energy of InAs(137) were performed, using the same methodology as described in [136] and [137].

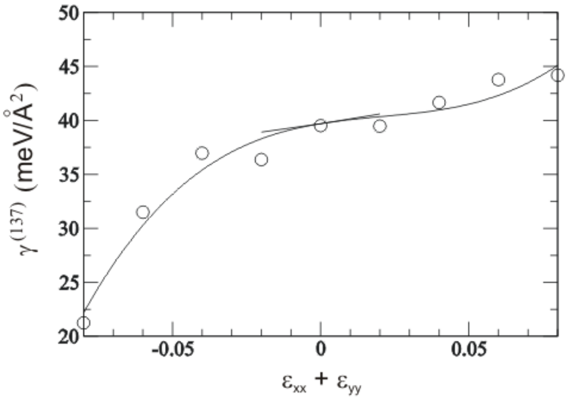

Fig. 4.6: Surface energy γ of the the InAs(137) surface as a function of strain ε, per unit surface area (of the unstrained material).

Since the $\{137\}$ facet appears at the base of the experimentally observed dome-shaped islands and hence may be highly strained, the dependence of its surface energy, $\gamma^{137}(\varepsilon)$, on strain ε was calculated. To this end, DFT calculations were performed for slabs under biaxial strain, while the surface could relax freely in the direction of the surface normal.

Results of these calculations are shown in Fig. 4.6. It turns out that the surface energy is significantly reduced under compressive biaxial strain. This finding is in close analogy to GeSi islands on Si(001), where it has been shown that the surface energy of the $\{105\}$ side facet is also strongly reduced by strain [138, 139, 140, 141]. To capture the strain dependence, a parametrization by a third-order polynomial is used for the $\{137\}$ facets.

For the other facets forming the steep upper part of the 3D islands, the surface strain is small and can be taken into account by a linear correction proportional to the intrinsic surface stress, $\sigma^{(i)}$, following earlier work by Moll et al. [136]

$$\gamma^{(i)}(\varepsilon) = \gamma^{(i)}(\varepsilon = 0) + \mathrm{Tr}(\sigma^{(i)}\varepsilon^{(i)}) \tag{4.4}$$

For numerical evaluation of $\gamma^{(i)}(\varepsilon)$, the two in-plane components of the strain on each facet, averaged over the facet area, are taken from the finite-element calculations. We find the two components to be rather similar, which justifies the approximative use of an isotropic stress tensor in Eq. 4.4. Finally, the term E_{surf} in Eq. 4.1 is calculated as

$$E_{surf} = \sum_i \gamma^{(i)}(\varepsilon^{(i)})A^{(i)} - \gamma^{(0)}A^{(0)} \tag{4.5}$$

where $\gamma^{(i)}(\varepsilon^{(i)})$ and $A^{(i)}$ denote the surface energies and surface areas of the ith side facet of the QD. The numerical values of $\gamma^{(i)}$ and $\sigma^{(i)}$ are adopted from Fig. 4.6 and from Ref. [136], Table II. $A^{(0)}$ denotes the island base area, and $\gamma^{(0)}$ is the energy per area of the wetting layer, including both surface and interface contributions, but excluding the strain energy stored in the wetting layer (which is treated separately by the term $\varepsilon_{\mathrm{film}}$, cf. Eq. 4.3). Numerically, the value $\gamma^{(0)}(\mu_{\mathrm{As}} = \mu_{\mathrm{As(bulk)}} - 0.2\mathrm{eV}) = 42$ meV/Å^2 is used, which has been determined from DFT calculations [135].

4.4 Evolution pathway: growth and faceting

In the following, we suggest a kinetic pathway for the transition from small to large InAs islands and explore its energetic implications. Since the shape transition is a dynamic non-equilibrium phenomenon involving up to 10^5 atoms, it is very difficult to describe it using results from theoretical calculations of equilibrium properties. We rather need to use experimental information about intermediate shapes as input for the analysis, augmented by the guiding principle that changes of the island shape occur predominantly through surface mass transport. This implies that a later shape during the growth transition results from an earlier shape by adding material to the side facets (by a layer-by-layer growth on these facets). This is particularly plausible at the growth temperatures used for our experiments and implies that the material already incorporated into a complete side facet will remain there and is no longer available for growth or reshaping of the islands.

Our description of the shape transition, inspired by the experimental observations shown in Fig. 4.5, is outlined in the sequence of pictures in Fig. 4.7: starting from the flat shape bounded predominantly by the $\{137\}$ facets observed experimentally, and proceed by adding a steeper top part delimited by low-index facets, whose size continuously increases from Fig. 4.7

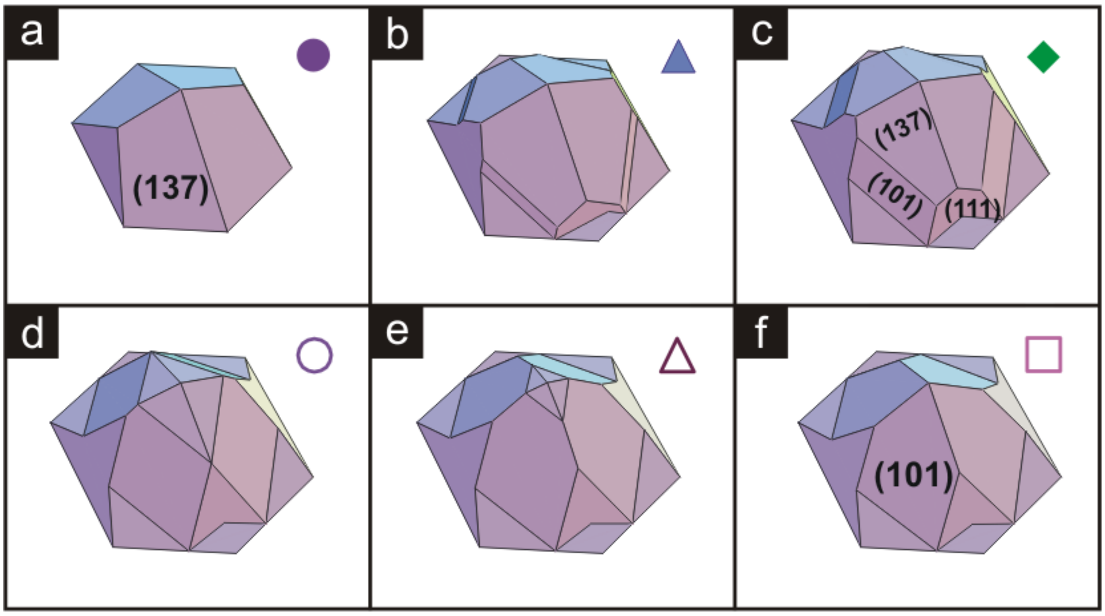

Fig. 4.7: Proposed sequence of shapes for the growth of InAs 3D island on GaAs(001). Small islands, a), are bounded by $\{137\}$ and $\{\bar{1}\bar{1}\bar{1}\}$ facets. Growth proceeds mostly through layer-by-layer growth on the $\{137\}$ facets; however, the newly grown layers do not make contact with the (001) substrate (Fig. b). As a result, $\{110\}$ and $\{111\}$ facets develop at the lower end of the added layers, giving the island an increasingly steeper appearance (Figs. c)–e)). Eventually, a sharp tip could possibly develop if growth of the $\{110\}$ facets extends to the top (Fig. f).

b through e. For the construction of the shape, we use the guiding principle (evidenced in Ref. [142]) that, whenever shallow facets exist at all as part of the equilibrium shape, they must appear both in the top part and at the foot of the island This is in line with the experimental observation, Fig. 4.5c, where, in addition to shallow facets at the top, the island is found to be surrounded by a rim of material with the same slope as the top facet [74, 102].

In order to facilitate the calculations, we have assumed somewhat simpler island shapes compared to the experimental ones. For example, we have neglected the small shallow $\{\bar{1}35\}$ and $\{\bar{1}12\}$ facets that have been recently reported for the first stages of the islands evolution [143]. Nevertheless, we believe that this simplification does not substantially modify the key aspects of the shape transition.

Moreover, we have considered only the case of islands composed of pure InAs, while a more realistic treatment should include islands with an InGaAs composition. The lower surface energy of InAs in respect to GaAs causes an InAs surface enrichment also in alloyed islands. As a consequence, the surface energies calculated in this work should be valid also for more realistic islands. The situation is clearly different for the bulk strain relaxation. As long as the InGaAs alloy is uniformly distributed within the island, the only difference with the energy values calculated here would be a reduced lattice mismatch α and therefore, from Eq. 4.3, a smaller elastic energy per unit volume. The experimentally reported island compositions are however quite anisotropic, with an increasing indium concentration in the growth direction [144, 145]. This will surely influence the strain energy but we expect it to be only a second-order effect.

4.4.1 Energetics of the islands formation

For all the shapes calculated, we find that the first term in Eq. 4.1 is an energy gain, i.e., the islands stabilize themselves by strain relief compared to the homogeneously strained film. It can be shown within continuum elasticity theory that the bulk strain relief (disregarding island-island interaction and strain relief due to edge discontinuities) scales proportional to the volume of the island. One the other hand, the second term in Eq. 4.1, due to the creation of side facets, is found to be an energetic cost for all calculated shapes. As a surface term, it scales like $V^{2/3}$ to leading order (i.e., disregarding the renormalization of surface energies due to strain, cf. Eq. 4.4). We make use of these scaling relations to extend our results, calculated for a particular shape and size, to islands of the same shape, but arbitrary size. The gain due to strain relief, E_{relax}, being a volume effect, ultimately becomes dominant for the larger islands. Using the scaling relation

$$E_{\mathrm{tot}} = e_{\mathrm{relax}} V + e_{\mathrm{surf}} V^{2/3} \tag{4.6}$$

enables us to extend our results, calculated for a particular island size, to any size of the island, where $e_{\mathrm{relax}} = E^{\mathrm{is}}_{\mathrm{relax}}/V - \varepsilon_{\mathrm{film}} < 0$ and $e_{\mathrm{surf}} = E_{\mathrm{surf}}/V^{2/3} > 0$ are shape-dependent quantities calculated within continuum elasticity theory and within DFT, respectively.

4.4.2 Chemical potential of In atoms and punctuated island growth

Previous theoretical work [133] has given evidence that for a given amount of material the 3D islands during their growth stage are fed by material diffusing towards the island from the wetting layer around it. This idea has been experimentally confirmed both indirectly by arguments of mass conservation [108], as well as by direct observation of the erosion of steps near islands [146, 143].

Under conditions where the mass transport occurs sufficiently close to equilibrium, it can be described as being driven by a difference of chemical potential $\Delta\mu_{\mathrm{In}}$ between the InAs species in the island and in the surrounding wetting layer: as long as the chemical potential of an atom attached to the island is lower than the chemical potential of the adatom lattice gas, the island will proceed to grow; else its growth will stop. In the following, we will derive the relevant chemical potential difference as a function of island size and shape from the hybrid approach.

For the usual definition of the chemical potential, allowing for unconstrained variation of shape with size, differentiation of Eq. 4.6 with respect to the number of In atoms, N_{In} (proportional to V) yields a monotonously decreasing function. However, as we indicated in the preceding section, it is more relevant to consider a situation where attachment of new material at the foot of the island has stopped to occur due to the highly compressive strain that makes attachment of InAs in this region highly energetically unfavorable (see, e.g. Ref. [147], although the authors, somewhat paradoxically, assume that facet growth would initiate in this highly strained region). There is experimental support for such a scenario, which has been put forward by Madhukar and co-workers under the term *punctuated island growth* [112].

Recently, Montalenti et al. [127] and Xu et al. [143] have employed similar considerations to analyze their experimental data. Mathematically, the chemical potential can be obtained in this case from the variation of the free enthalpy under the constraint of fixed base area of the island. As we will see below, the chemical potential

$$\Delta\mu_{\mathrm{In}} = \left(\frac{\partial \Delta G}{\partial N_{\mathrm{In}}}\right)\bigg|_{p,T,A^{(0)}} \tag{4.7}$$

$$\approx \frac{\partial E_{\mathrm{tot}}}{\partial N_{\mathrm{In}}}\bigg|_{A^{(0)}} = v_{\mathrm{mol}} \frac{\partial E_{\mathrm{tot}}(A^{(0)},h)}{\partial V(A^{(0)},h)}\bigg|_{A^{(0)}} \tag{4.8}$$

defined with *the constraint of fixed base area* $A^{(0)}$ is generally a non-monotonous function of V. Here, v_{mol} is the volume of an InAs pair in the InAs crystal. Moreover, in going from Eq. 4.7 to Eq. 4.8, we have assumed that vibrational and configurational entropy contributions to ΔG largely cancel when considering differences, and hence these contributions can be neglected.

To be specific, we consider the situation where further growth of the island is possible only by incomplete facet layer growth: at first, a small island, of the shape shown in Fig. 4.7a, will grow in layer-by-layer growth mode on the $\{137\}$ facets, thus reproducing its shape.

As the most likely growth scenario, we consider that the facet layers start to grow from the island top and fill the facet by growing downward. At a later stage, layer growth stops before the growing facet layer touches down to the substrate (or only reaches it at a single point, as shown in Fig. 4.7b.

While more and more incomplete $\{137\}$ facet layers grow from top to bottom, steeper facets of the $\{110\}$, $\{111\}$ and $\{\bar{1}\bar{1}\bar{1}\}$ families develop at lower terminating edges of the incomplete facets. Fig. 4.7c–f are a schematic representation of this growth sequence.

In the language of layer-by-layer growth, the appearance of steeper facets can be interpreted as step bunching. Indeed, for Ge islands on Si, an analogous discussion in terms of stepped side facet growth has been given in Ref. [127]. The growth scenario of Fig. 4.7, evaluated for fixed base area $A^{(0)}$, defines a unique relation $V(A^{(0)},h)$, which enables us to evaluate the derivative in Eq. 4.8.

Figure 4.8 displays both the unconstrained chemical potential (solid line), and the chemical potential for constrained growth of islands with a given base area (dotted lines). The latter was obtained by inserting the scaling relation Eq. 4.6, for the two-parameter function $E_{\mathrm{tot}}(A^{(0)},h)$ into Eq. 4.8, and taking the derivative under the constraint of fixed base area.

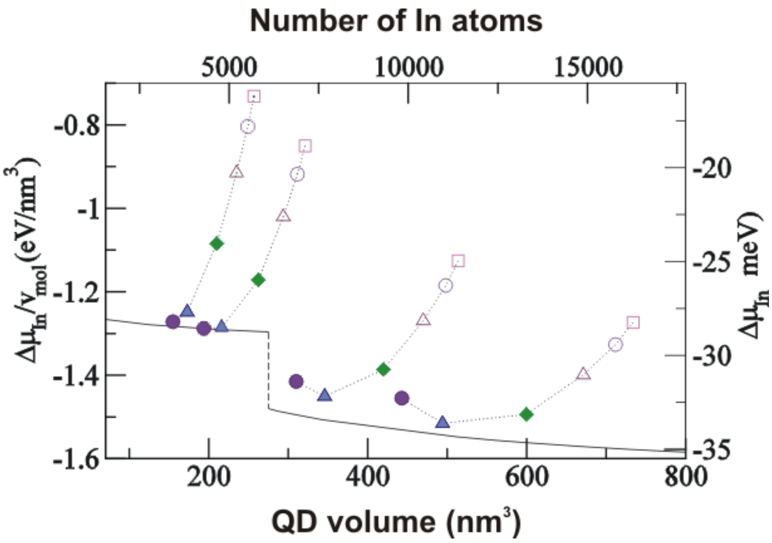

Fig. 4.8: Chemical potential of In atoms in 3D islands of various fixed base areas, as a function of the island volume. The curves, from upper left to lower right, correspond to islands with a base diameter in [110] direction of 19.8, 24.7, 39.6, and 56.6 nm, respectively. The symbols along the curves refer to the different shapes shown in Fig. 4.7. For islands of small base area, adding material on top of the pyramid, (Fig. 4.7a) would result in an increase of chemical potential and hence doesn't occur spontaneously. For islands with a base length larger than 30 nm, however, a transition from the shape in Fig. 4.7a to Fig. 4.7b becomes a spontaneous process accompanied by a lowering of $\Delta\mu_{\text{In}}$ (dotted lines, Eq. 4.8). The unconstrained chemical potential (solid line) shows an abrupt drop at the growth transition.

While the unconstrained chemical potential decreases monotonously, the constrained chemical potential is found to increase for the two smallest base areas shown. The latter finding indicates that there is no driving force for a spontaneous transition of the island shape in these cases, i.e., the shape of Fig. 4.7a is stable for small base areas, and would reproduce itself in layer-by-layer growth mode on the side facets.

For islands with larger base areas, however, the constrained chemical potential decreases when growth proceeds from Fig. 4.7a to Fig. 4.7b (compare the filled circles and filled triangles in Fig. 4.8). This implies that layer growth on the $\{137\}$ facets becomes incomplete, and a band of steeper $\{101\}$ facets develops spontaneously. The shape transition is defined by this initial decrease in the constrained chemical potential.

For the conditions of this study ($\mu_{\text{As}} = \mu_{\text{As(bulk)}} - 0.2$ eV), the shape transition occurs for a volume of about 270 nm^3, a base diameter of about 30 nm, or 6000 In atoms and 6000 As atoms in the island. We note that these numerical values may vary depending on growth temperature, arsenic partial pressure, and the degree of actual intermixing between InAs and GaAs in the island. Although this implies that a direct comparison of the calculated values with experiments has to be taken cautiously, the values of the transition volume that we found in our measurements agree reasonably well with the theoretical ones.

The fact that the transition is spontaneous only above a specific island size can be expressed also in another way: introducing the band of $\{101\}$ facets is energetically favorable only if they have a minimum size, i.e., if the island has some minimum base length. For smaller islands, the energetic cost of introducing these facets is not yet counterbalanced by the energy gain of strain relief in the upper part of the island.

The unconstraint chemical potential, also plotted in Fig. 4.8, shows an abrupt drop at the shape transition. This behavior brought out by the hybrid approach for the InAs/GaAs(001) islands conforms with the results of a simpler continuum treatment for GeSi islands on Si(001) [148]: both in this study and in our work, a discontinuity of the chemical potential occurs during island evolution. In the case of GeSi/Si(001), the consequences of this finding for the growth kinetics have been worked out [148].

In brief, it gives rise to an anomalous island size distribution characterized by a few islands that have passed the transition point and continue to grow quickly, while a large number of smaller, pyramidal islands are left behind in their evolution.

While the smallest islands shrink (as seen in Ref. [149]) and are eventually consumed by the large dome-shaped islands, the remaining pyramids show a narrow distribution of sizes peaked slightly below the transition point.

Thus the spontaneous transition to large dome-shape islands triggers anomalous coarsening of the overall island population. In this case, a narrower island distribution than expected for conventional (Ostwald) coarsening kinetics result. We expect a similar anomalous kinetics to be operative in the InAs/GaAs(001) system. Due to our atomistic treatment of the surface energies, we can identify the incomplete facet growth on the $\{137\}$ side facets of the InAs islands and the appearance of steeper $\{101\}$ facets as the microscopic cause for the anomalous coarsening kinetics. A more detailed understanding of the kinetic implications of our findings needs to await kinetic simulations using the calculated energetics as input.

4.4.3 Shape of equilibrated islands

If a single island is considered as an isolated system (rather than in equilibrium with the wetting layer), the stability of the island is characterized by the energy per atom, or likewise, per volume, $E_{\rm tot}/V$. Such a theoretical description allows for *arbitrary* changes of the island shape and is appropriate for modeling annealing experiments without material deposition, where the influx of atoms to the islands is much smaller than during growth.

Making contact to previous studies [136, 133], the quantity $E_{\rm tot}/V$ is evaluated and compared for different shapes and sizes. The curves plotted in Fig. 4.9 were obtained by evaluating Eq. 4.6 for the various shapes of islands shown in Fig. 4.7. The asymptotic energy gain in the limit of large islands, dominated by strain relief, is maximum for the fully-developed dome shape.

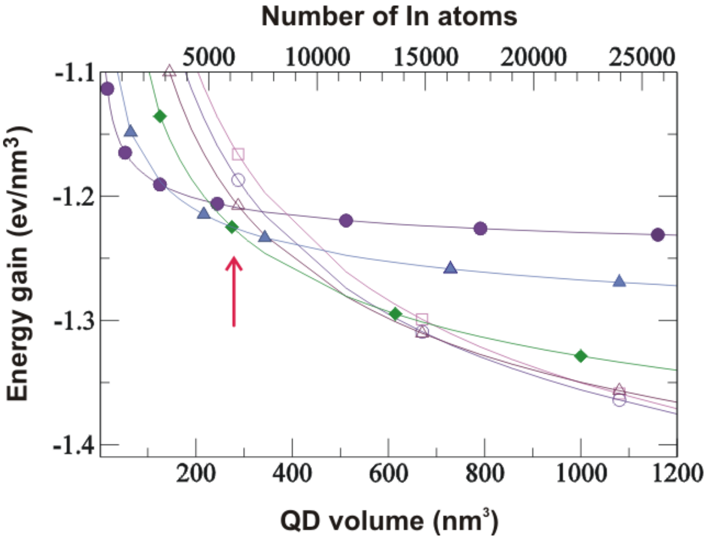

Fig. 4.9: Energy gain per volume for the formation of islands of different shape, as shown in Fig. 4.7, as a function of the island volume. The symbols refer to the shapes labelled a–f in Fig. 4.7. The lowest-energy pathway for island growth within the given family of shapes is described by the lower convex envelop of the individual curves. The arrow marks the shape transition point.

For small islands, however, the flat pyramid is energetically favorable, due to its low cost in terms of surface energy. The shallow $\{137\}$ side facets increase the surface area only moderately compared to the base area $A^{(0)}$ of the island. Furthermore, the high surface strain on these facets lowers their surface energies considerably, as seen from Fig. 4.6. Going from small to large island volumes, the energetically most favorable shape runs through the sequence depicted in Fig. 4.7 a–f. The lowest-energy pathway for island growth, within the family of shapes given by Fig. 4.7, corresponds to the lower convex envelop of the curves for the individual shapes.

By attempting to fit the convex envelop by a single functional dependence, it can be seen that there is a cusp in this curve at a volume $V = 270\,\mathrm{nm}^3$, indicated by the arrow in the Fig. 4.9. Since only a discrete set of shapes has been calculated, Fig. 4.9 alone would not warrant such a conclusion.

However, the analysis of growth with fixed base area in the previous section puts us in position to conclusively identify the shape transition point. The cusp in the lower convex envelop in Fig. 4.9 gives rise to the discontinuous drop of the unconstrained chemical potential at the transition seen in Fig. 4.8.

It is interesting to note that the shape of Fig. 4.7b (filled triangles) appears in Fig. 4.9 already before the shape transition, while its first appearance is indicative of the transition in Fig. 4.8. This is due to the different restrictions imposed in both treatments: dropping the constraint of fixed base area, i.e., allowing for the relocation of material from the island foot to the top facets, stabilizes the shape of Fig. 4.7b) already at an earlier stage.

Compared to previous work [133] assuming an island shape bound by low-index facets *only*, the lower convex envelop obtained in the present study has a smaller energy per volume. Thus we have demonstrated that the occurrence of the high-index $\{137\}$ facets indeed leads to an enhanced stability of the islands, which gives additional support to the choice of shapes in Fig. 4.7 originally inspired by experiment.

The transition from the flat to a dome-like shape is clearly visible when the energy gain E_{tot}/V is plotted for a fixed amount of material as function of a variable parameterizing the shape transition. In Fig. 4.10, we use the aspect ratio (ratio of height h to base diameter, measured along [110]) as a descriptor of the shape. Clearly, islands of small volume are seen to have a minimum of the energy per particle for the flat pyramidal shape, while very large islands, of size larger than 1000 nm^3, favor a very steep shape with an aspect ratio in excess of 0.4, see for example Fig. 4.7f).

Between these two extremes, domes with an aspect ratio in the range of 0.29 – 0.33 are found to be the energy minimum of the moderately larger islands of the typical sizes observed in experiment, with a volume up to about 1000 nm^3, or up to some 22,000 indium atoms.

Thus, the range of aspect ratios for small and medium-sized islands found in our present study is in much better agreement with experiment than previous theoretical models [136, 133].

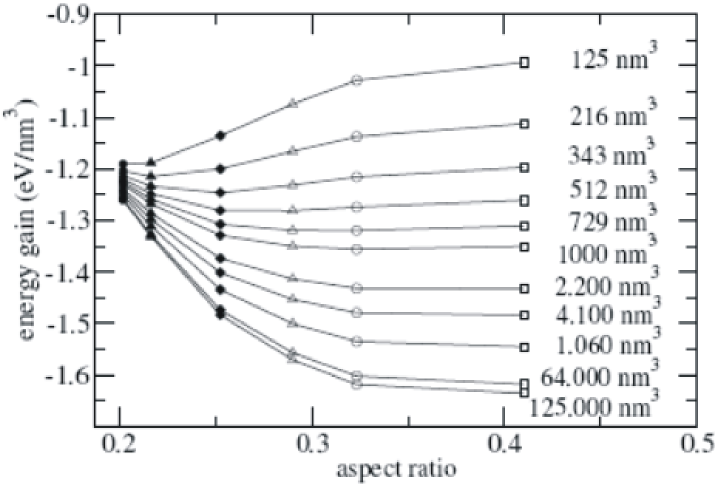

Fig. 4.10: Energy gain per unit volume for an island formed from a given amount of material, but with no restrictions on its shape. On the abscissa, the shapes displayed in Fig. 4.7 are represented by their aspect ratio (height : base diameter). The curves, from top to bottom, correspond to increasing amount of material (volume), as specified by the labels. While for small islands (uppermost curve) the flat pyramid of Fig. 4.7a is energetically preferable, islands in later stages of their growth prefer a dome-like shape.

From this combined work comprising STM measurements of InAs islands grown by MBE and calculations of the thermodynamic stability of these islands, we were able to provide evidence for a shape transition in InAs/GaAs(001) heteroepitaxy.

For small island sizes, flat pyramids dominated by {137} facets are energetically favorable. Density-functional calculations of the surface energy and surface stress of these facets show that their appearance is favored by the pronounced lowering of the (137) surface energy on the compressively strained side facets of the InAs islands. For larger islands, a higher aspect ratio is found to be preferable due to more efficient strain relaxation in the steep part of the island. Hence there is a thermodynamic driving force for developing a dome-like shape on top of a flat base as the island grows larger. Furthermore, our theoretical analysis shows that the change of island shape can be understood in analogy to a structural phase transition with an abrupt drop of the chemical potential at the transition point, with important consequences for the growth kinetics of the island ensemble as a whole.

Chapter 5

On the capping of 3D InAs strained islands

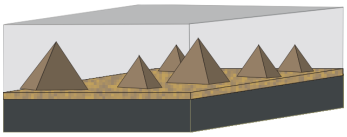

5.1 Quantum Dots Confinement

Quantum confinement is the hallmark of semiconductors 3D islands. Nonetheless, free standing islands confinement is usually hindered by interface defects (non-radiative recombination) or diminished by the island's surrounding. Free standing islands have a smaller emission energy than that of buried strain islands. Capping of the islands by a larger band gap, strengthen the required 3D confinement and has proven to homogenized the islands distribution sizes, improving as well the optoelectronic properties as a whole.

A fundamental aspect that has recently attracted substantial attention is that the deposition of a capping layer might be, and very often is, far from being harmless for the 3D islands. In fact, the capping procedure itself is a lattice mismatched heteroepitaxy process and is therefore associated with strain release, segregation, faceting, intermixing, strain-enhanced diffusion, etc..

These phenomena take place at the island surface and can strongly modify the quantum dot morphology and composition. Since the optical and electronic properties of QDs strongly depend on their size, shape and stoichiometry, a detailed microscopic understanding of the capping process that ultimately allows a tailoring of the opto-electronic characteristics, becomes essential.

For the Ge/Si(001) system a microscopic picture of the dot overgrowth has recently been established [150, 151]. The transformation that dome islands undergo while being capped by a Si layer have been precisely characterized and described based upon the dependence of the optimal island shape on its composition [151]. This is not the case for InAs/GaAs(001), the model system which is mostly used for QDs for optical investigations. Although several reports have been published on this topic [152, 153], a coherent picture of the capping process based on a systematic microscopic investigation was still lacking.

This chapters deals with the study of the GaAs overgrowth of well-characterized InAs QDs on GaAs(001) by means of STM. A detailed investigation as a function of the cap thickness and growth rate reveals the existence of two successive evolution regimes and a dramatic change of the islands morphology with the capping rate. Moreover, striking similarities with the GeSi case are found for the initial stages of the overgrowth, allowing us to identify general microscopic mechanisms responsible for the QD evolution during capping.

To extend the aforemention studies, the same growth conditions were used to prepared the islands to be capped. Islands were form by the deposition of 1.8 ML of InAs, deposited at 500^{o}C with a deposition rate of 0.008 ML/s and an As_4 beam equivalent pressure of 8x10^{-6} mbar. In order to avoid In desorption, the sample temperature was lowered to 460^{o}C right after InAs growth and GaAs capping layers of various thickness (0-15 ML) were deposited at three different rates Φ = 0.08, 0.6 and 1.2 ML/s. As soon as room temperature was reached, the sample was transferred under UHV to the STM.

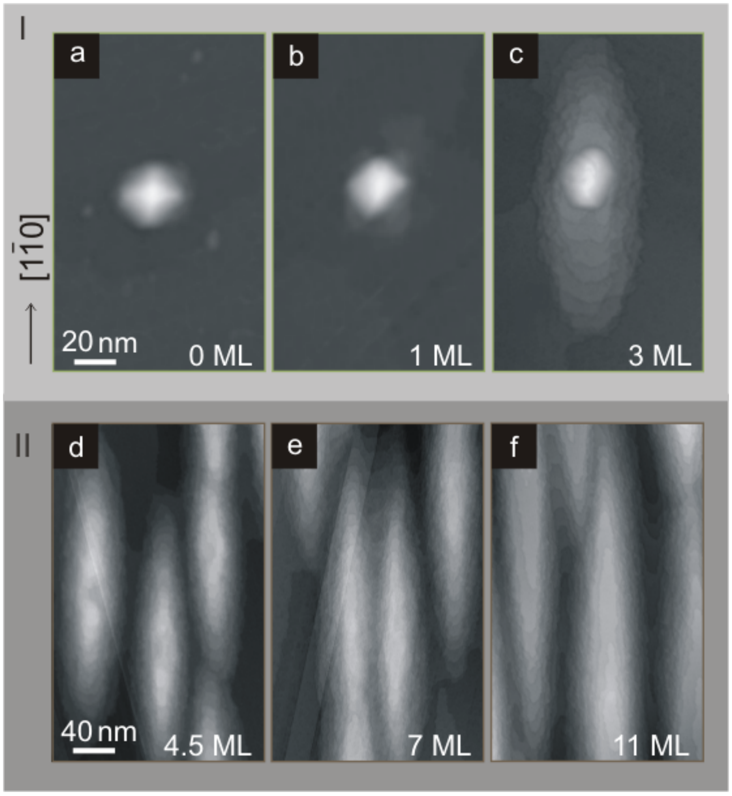

Fig. 5.1: a)–f) STM images of InAs dome islands during GaAs capping at 0.08 ML/s. The islands were overgrown by different capping thickness as indicated in each image.

Figures 5.1 a–f show the evolution undergone by InAs domes when capped with increasing amounts of GaAs at a rate of 0.08 ML/s. Even at the very first stages of capping (1 ML), strong modifications take place in the island morphology: the height is considerably reduced and a rim of material starts to accumulate around the island base (Fig. 5.1b). After the deposition of 3

ML of GaAs, only a small part of the original island is still visible, while the surrounding rim increases its height and elongates in the direction of the substrate (Fig. 5.1c). Further deposition of GaAs causes the complete disappearance of the faceted regions and a steady increase in the length of the elongated structures that eventually merge (Fig. 5.1 d–f).

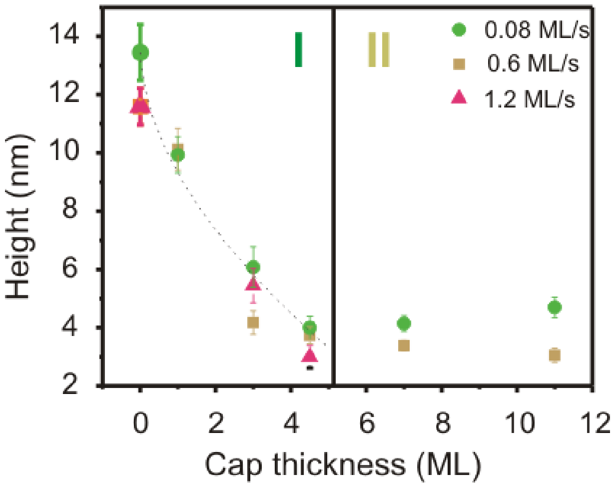

Fig. 5.2: Island heights h as a function of the cap thickness for different GaAs deposition rates. The series at 0.08 ML/s was analyzed by STM, and those at 0.6 and 1.2 ML/s by AFM. The scatter line corresponds to the best fit of the model described in the text.

We measured similar evolution series for different GaAs deposition rates by ex-situ AFM, to monitor the height changes as a function of the capping layer thickness. The quantitative analysis of the height of the overgrown structures is reported in Fig. 5.2.

The most evident result is the existence of two well-defined capping regimes. The first regime is characterized by a rapid height collapse of the pristine islands, while the second is marked by a true overgrowth of the remaining structures, as demonstrated by a non-negative slope of the height vs. cap thickness. Comparable trends have been reported for the overgrowth of InAs islands under different experimental conditions [67, 154]. A similar behavior has also been observed in the capping of Ge islands with Si [151], indicating, the generality of this phenomenon. In the following, we will separately discuss the two regimes, trying to identify the microscopic processes that govern the corresponding morphological transformations.

5.2 First regime: Island dissolution

Higher resolution STM images of the first capping regime are reported in Fig. 5.3 for the central part of the actual structure, i.e. disregarding the elongated rim. A quantitative analysis of the

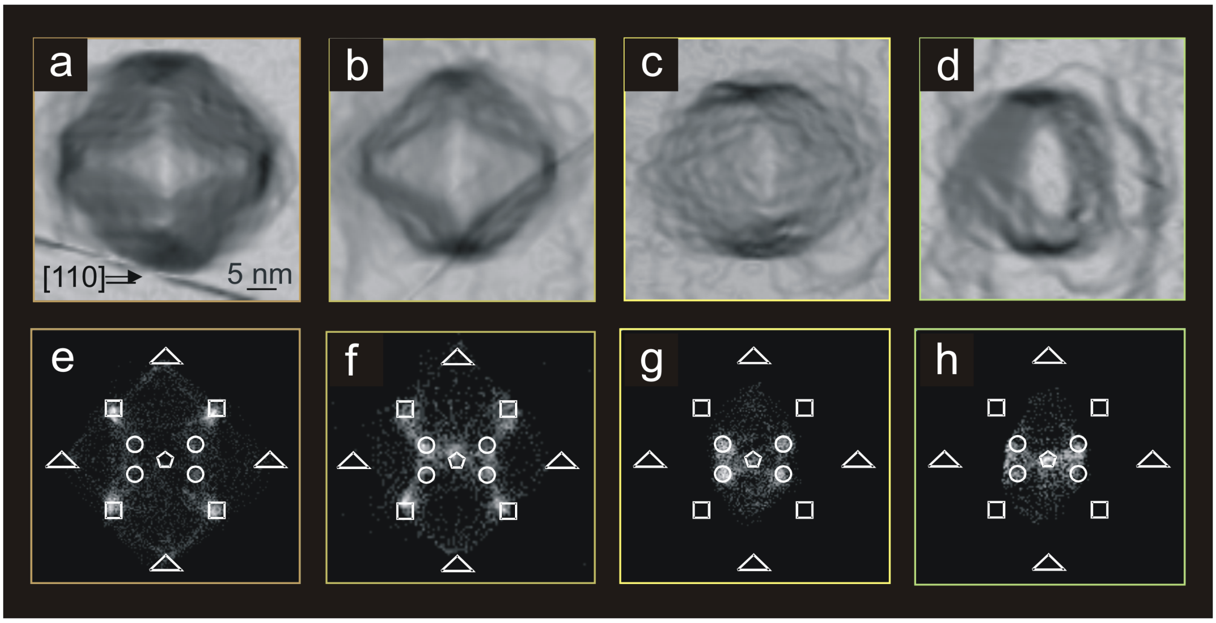

Fig. 5.3: Island shape evolution during the first capping regime. a) Initial dome, b) 1 ML, transition dome, c) 2 ML, pyramid and d) 3 ML, truncated pyramid. The gray scale of the STM topographies represents the local surface slope. Figures e–h show the corresponding FPs for each island.

facet distribution can be performed by analyzing the FPs of the islands for each coverage (Fig. 5.3 e–h).

The pristine domes (Fig. 5.3 a and e) are delimited by steep $\{101\}$ and $\{111\}$ as well as by shallow $\{137\}$ facets. After 1 ML of GaAs has been deposited (Fig. 5.3b) , the $\{137\}$ facets located at the islands' apex become larger while the other facets drastically reduce in size as reflected by the change in the relative spot intensity in Fig. 5.3f. With increasing cap thickness, the island shape further changes first into a pyramid dominated by $\{137\}$ facets (2ML GaAs, Figs. 5.3 c and g) and finally into a truncated pyramid with an extended $\{001\}$ top facet (3ML GaAs, Figs. 5.3 d and h).

This morphological transformation is quite similar to that occurring during the Si overgrowth of Ge domes [151] and is essentially the reverse of the pyramid-to-dome transition occurring during growth [155]. The later can be appreciated by comparing Fig. 5.3 and Fig. 4.5 from the previous chapter.

We notice that the temperature quenching rate of our experimental setup seems to be sufficient for preserving the overgrown structures when starting from a substrate temperature of 460°C. In contrast to what was reported for 500°C [153], we do not observe any relevant island leveling, i.e, an equivalent increased in height of the wetting layer thickness, here taken as the reference plane. Substantial changes in the island height can only be detected by intentionally introducing an extended annealing after a partial capping of the island.

Relevant structural modifications happen already at the very first stages of the overgrowth, e.g. the deposition of only 0.28 nm GaAs (1ML) induces a island height decrease of 3 nm (about 25% of the original value), therefore a dynamic picture that accounts for the atomic-level processes occurring during the cap deposition is more suitable than a static one based on thermodynamic arguments only [151, 156].

From the observed changes we can be understood as follow, the Ga atoms that are deposited directly onto the domes do not find favorable adsorption sites [157] since the lattice parameter of these islands approaches that of pure InAs across their tops [158]. As a consequence, Ga atoms tend to migrate away from the islands' apex and to accumulate at their base (Fig. 5.4a) where the lattice parameter is closer to GaAs. These Ga-rich regions represent advantageous alloying sites for the In atoms of the islands, whose chemical potential can decreases because of both entropy gain and strain energy release [159]. The net result is thus a redistribution of the islands' material from the top to the base that causes the observed height decay (Fig. 5.4b). At the temperatures used during our experiments a bulk reshuffling of the atoms is kinetically hindered and the displacement of the island In-rich material can be produced by surface diffusion processes only. In other words, the lowering of the islands' height happens through a layer-by-layer removal of material, naturally producing an extension of the $\{137\}$ facets at the expenses of the steeper $\{101\}$ and $\{111\}$ ones (Figs. 5.3, 5.4b). This is the opposite of what happens during growth, where pyramids evolve into domes by layer-by-layer stacking of incomplete shallow facets at their tops [160]. From this point of view it is thus not surprising that a reverse dome-to-pyramid transition is associated with the island height decrease during capping.

5.3 Second regime: True overgrowth

Figure 5.2 clearly shows that for a cap thickness $\leq$ 4 ML the island decay is almost independent of the Ga deposition rate, indicating that this first overgrowth regime must be governed by a rapidly occurring diffusion processes. This is coherent with the above microscopic description, where the morphological transformations are induced by strong driving forces such as the release of elastic strain energy through alloying and the reduction of surface energy. In other words, this first regime is thermodynamically driven as further indicated by the island morphologies in Fig. 5.3 that closely resemble InAs/GaAs(001) equilibrium island shapes [160].

A simple 1+1 D analytical model can be developed for describing the experimentally observed behavior. According to our previous analysis, the first capping regime can be schematically described as the island shrinking depicted in Fig 5.4b. As a consequence, the island volume can be expressed as

$$V(t) = V_0 - \frac{[h_0 - h(t)]^2}{\alpha_2 - \alpha_1} \tag{5.1}$$

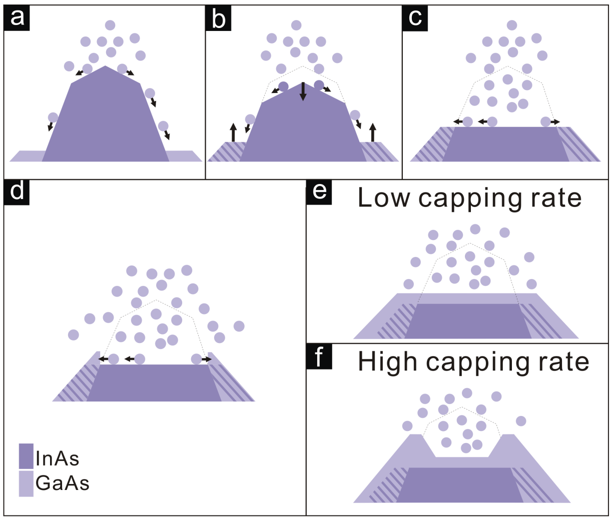

Fig. 5.4: Schematic representation of the QD overgrowth process. Only the III-group elements are considered for simplicity.

where V_0 and h_0 are the initial island volume and height, respectively and α_1 and α_2 are the slopes of the shallow and steep facets, respectively. The number of atoms that leave the island per unit time is given by

$$\frac{dN_{In}}{dt} = -\Omega^{-1}\frac{dV}{dt} \tag{5.2}$$

where Ω represents the atomic volume. If we assume that each new Ga atom arriving from the flux induces the detachment of β In atoms from the island, we find that

$$\frac{dN_{In}}{dt} = \beta\frac{dN_{Ga}}{dt} = 2L\Phi\beta \tag{5.3}$$

where Φ is the Ga flux and 2L the lateral island size. This leads to a differential equation for the island height with a solution equal to

$$h(t) = h_0 - \sqrt{2C\Phi t} \tag{5.4}$$

with C = $\beta\Omega$L($\alpha_2 - \alpha_1$).

Despite the extremely simplified assumptions of the model, this functional dependence describes quite well the initial rapid island shrinking and particularly its independence of the Ga deposition rate (Fig. 5.2. By fitting the model to the experimental data, we obtain $\beta \sim 1$, which is a quite reasonable value. This results indicates that on average, each Ga atom reaching the island produces the out-diffusion of one In atom.

In contrast to the SiGe case [151], the alloy composed of the In from the island's top and the Ga of the capping flux is not incorporated into a faceted base, but accumulates into (001)-stepped flanks (Figs. 5.1 b–f). The highly anisotropic diffusion of In on the InGaAs(001) surface (see Table 3.1), prones the formation of the elongated island shapes [161] since, once adatoms have reached the island's base, they move preferentially along the [1$\bar{1}$0] direction [162].

Moreover, the adatom diffusion on these (001) stepped mounds has to be much slower than on the island's facets. In fact, contrarily to the island height, the lateral extension of the flanks is kinetically determined, being larger for lower GaAs deposition rates (Figs. 5.5 a–b and d–e).

While the height of the islands decreases with the amount of the deposited GaAs, that of the lateral flanks increases (Fig. 5.4 b). A closer look at the structures that develop just after these two opposite moving fronts have met, reveals the formation of two shallow humps symmetrically located with respect to the original island position (Figs. 5.5 b and e and Fig. 5.4d). These are caused by the same microscopic processes that induce the island shrinking.

In this case, since the central part of the island is no longer protruding, the preferential migration of Ga and In atoms away from its center (driven by lattice mismatch and alloying, respectively) leads to the formation of a central depression and of the observed lateral humps. We notice however that the In out-diffusion cannot go on indefinitely. In fact, even before capping, nominally pure InAs islands are actually characterized by a vertical compositional gradient [163, 85, 164], with a Ga content close to their base that can be even larger than 60% [158]. As a result, the driving mechanisms of In out-diffusion and alloying first weaken and then completely vanish with decreasing island height. Thereafter a true overgrowth sets in. A direct consequence of this effect can be found in the experiments by Songmuang et al. [104], where the height at which the island collapse stops, scales with the indium percentage of the $\mathrm{In}_x\mathrm{Ga}_{1-x}\mathrm{As}$ capping layer.

At variance with what happens in the first capping regime (Figs. 5.5 a and d), the morphological transformations occurring after the In out-diffusion has stopped, strongly depend on the capping deposition rate (Figs. 5.5 c and f). At a GaAs rate of 0.08 ML/s the humps in Fig 5.5a are quickly smoothened out and only $[1\bar{1}0]$ elongated mounds remain, centered at the position of the original islands (Figs. 5.5c and Figs. 5.4e). On the contrary, when GaAs is deposited at 0.6 ML/s, the two protrusions continue developing and evolve first into camel humpback structures [104, 165] (Figs. Figs. 5.5d and Figs. 5.4f) and eventually into rhombus-shaped structures with a central hole (Figs. 5.5f) [166]. For both deposition rates, the c(4x4) surface reconstruction of the substrate, indicates a pure GaAs growing front for cap thicknesses larger than 15 ML. The morphological evolution during this second capping regime is mainly driven by a migration of Ga adatoms away from the position of the embedded island that acts as a stressor and causes a local lattice expansion [157]. As already noticed, this preferential diffusion over stepped (001) terraces is evidently slower than the diffusion processes governing the first capping regime. As a consequence, at lower deposition rates, longer diffusion lengths allow a surface smoothing. On the contrary, at higher rates the ability of surface diffusion to minimize surface curvature is kinetically reduced and the ridged morphology is reproduced for higher cap thicknesses. It has been recently reported that if the Ga deposition occurs under As_2 instead of As_4 flux, the anisotropy between the migration distances along the $[1\bar{1}0]$ and the [110] direction is significantly reduced and rounded ring-shaped structures form instead of the camel humpbacks [165]. However, we believe that the same type of microscopic processes described here are responsible also for the ring formation.

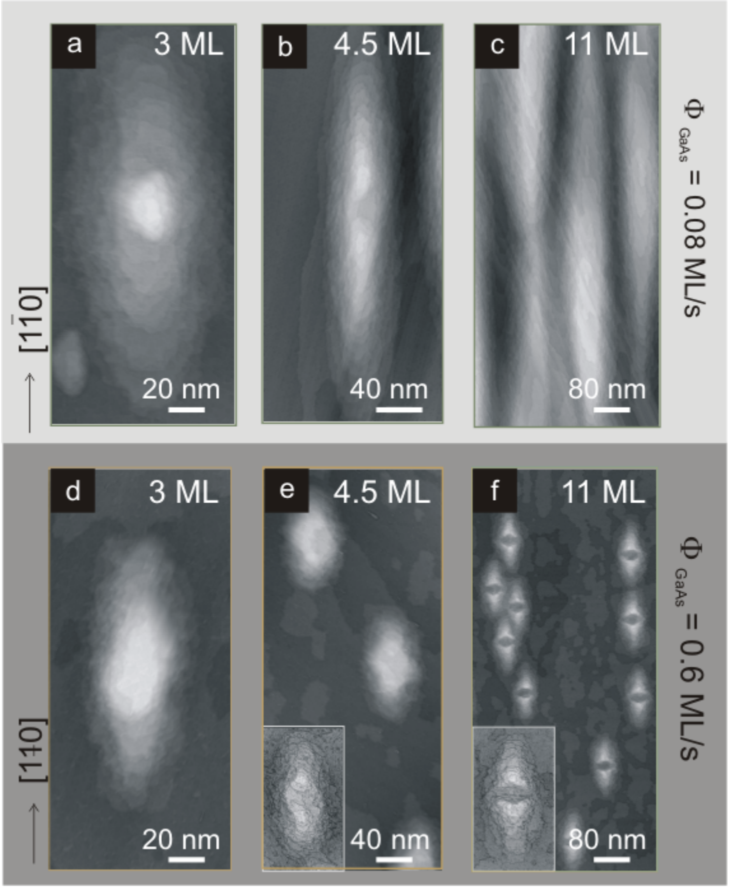

Fig. 5.5: Dependence of the overgrowth morphology on the GaAs deposition rate: upper row 0.08 ML/s, lower row 0.6 ML/s. Cap thickness: a) and d) 3 ML, first regime. b) and e) 4.5 ML, transition between the regimes. e) 11 ML and (f) 15 ML, second regime. The contrast of the 60 nm x 100 nm insets in e) and f) is enhanced by the use of the negative LSS.

Summarizing, we have thoroughly analyzed the GaAs overgrowth of InAs self-organized islands and determined the existence of two capping regimes. The first is characterized by a substantial island shrinking almost independent of the cap deposition rate. The resulting island structures closely resemble thermodynamic equilibrium shapes. The second is marked by a true overgrowth and is essentially determined by a kinetically limited diffusion on a stepped (001) surface. Depending on the GaAs rate, elongated mounds or structures with a central hole are formed. A simple description of the observed phenomenology has been developed based on microscopic diffusion processes. This model coherently accounts for many experimental reports on semiconductor island capping reported in literature.

Chapter 6

Summary and Outlook

6.1 InAs/GaAs(001): a microscopic picture

This dissertation comprises morphological studies of QDs in the InAs/GaAs(001) system. With the used of HR-STM images, a microscopic description of QDs formation could be completed.

Self-organized QDs had been subject to intense study for more than 15 years and applications are now commercially available. Albeit the vast number of experimental, as well, as theoretical results available, a clear unified picture of their nucleation, evolution and final capping had been missing. The complex interplay of thermodynamics and kinetics during QDs growth made the overall description extremely puzzling.

For this reason, with intention to establish a reference point for further studies, we examined samples grown under thermodynamic equilibrium conditions [73]. Even though kinetic effects can not be withdrawn entirely, this allow a systematic study of the distinct stages of QDs formation.

In this work, we have carefully study the early stages of 3D islands nucleation. Very small precursors with heights of ≤ 2 ML were found. These precursors possess undefined shape and start to appeared right after the critical thickness is exceeded. In some cases the nucleation starts with the formation of 2D platelets, that later on evolved into 3D faceted structures, as visible from the HR-STM images.

Incomplete facets start to developed in the growing islands whenever their aspect ratio exceeds ~ 0.15. At this point, the islands begin to resemble partially defined pyramids. As the growth continues, the facets are completed and the shape of the islands turns to well defined pyramids, bonded by four $\{137\}$ facets.

A second shape transition from shallow pyramids to multifaceted domes is also observed. Using a hybrid theoretical approach, thermodynamic analysis of the island stability was performed. Within this approach the elastic strain relief E_{relax} in the islands is calculated by continuum elasticity theory, while surface energies and surface stresses E_{surf} are taken from

DFT calculations. In this case, shape-dependant quantities consider the experimentally observed shapes as an input for the calculations.

Analyzing the evolution pathway of the islands during growth some important results can be drawn

- it was found that the surface energy of the $\{137\}$ facets is reduced under compressive strain, favoring their appearance as facets of the small highly-strained pyramids;
- islands stabilized themselves by strain relief compared to an homogeneously strained film, and ultimately, strain relief becomes predominant for bigger islands;
- the constrained chemical potential shows a discontinuity at each shape transition, in compliance with the lowest energy pathway. The discontinuity implies that the transition is spontaneous for a minimum island size where the energy cost of introducing steeper facets is counterbalanced by the energy gain in strain relief. Hence, the incomplete growth of $\{137\}$ side facets and the appearance of $\{101\}$ facets can be identify as the microscopic cause for the anomalous coarsening observed experimentally.

Based on the results, the fist part of the formation of InAs/GaAs(001), that is the nucleation and evolution of 3D islands, can be summarize as follows

- nucleation starts with the aggregation of small unfaceted islands that preferentially pin at defects or step edges. As the islands enlarged, facets start to developed partially until for an specific aspect ratio, fully faceted pyramids are formed;
- once pyramids are nucleated, they will begin to grow in a self-similar mode on the strained-stabilized $\{137\}$ facets, thus reproducing its shape;
- at a later stage, incomplete $\{137\}$ facets will start to form on the islands' top and fill the facet growing downward, without reaching the substrate;
- finally, after an accumulation of a certain number of incomplete facets, steeper $\{101\}$, $\{111\}$ and $\{\overline{111}\}$ facets developed at the lower terminating edges of the incomplete facets as a more efficient strain released mechanism.

For a complete description, the mandatory overgrowth process that the islands undergo in order to become QDs, was also subjected to study. The overgrowth process was analyzed as a function of the capping thickness and capping deposition rate.

The most evident result is that two well-defined capping regimes can be distinguished. The first regime is characterized by a rapid partial dissolution of the pristine islands, while the second is marked by a true overgrowth of the remaining structures.

Strong modifications take place in the islands morphology since the very first stages of the capping: the height is considerably reduced and a rim of material starts to accumulate around the island. After the deposition of only 1 ML of GaAs, the $\{137\}$ facets located at top of the pristine domes, become larger while the other facets drastically reduce their extension and assumes a transition dome morphology. With increasing capping thickness, this shape further transform first into a pyramid dominated by $\{137\}$ and finally into a truncated pyramid with an extended$\{001\}$ top facet.

From the observed transition shapes, it can be established that the first capping regime is mainly dominated by thermodynamics and that the dominant surface diffusion processes is the strain induced In out-diffusion.

Contrarily to the first regime, the development of the true overgrowth process is kinetically determined as can be seen by the lateral extension of the flanks, which is larger for lower GaAs deposition rates. While the height of the islands decreases, that of the lateral flanks increases with the amount of the deposited GaAs. A closer look at the structures that develop just after these two opposite moving fronts have met, reveals the formation of two shallow humps symmetrically located with respect to the original island position. As the capping continues, the driving mechanisms of In out-diffusion and alloying wane with decreasing island height until they finally vanish and a true overgrowth sets in.

6.2 Outlook: QDs electronic properties

As Feymman once said for nanotechnology, in the QDs description „there is still plenty of room at the bottom “. Single QD electronic structure characterization is just sprouting. Most of the work performed so far, involved ex-situ studies of overgrowth structures and multi-stacked heterostructures, where the individual QD wavefunctions are smeared out.

When the size of a nanostructure is comparable to the length of a few monolayers, nonuniform features such as strain, defects, and impurities become more important. These heterogeneous features lead to nonuniform electronic properties and just as embedded structures differ strongly from free standing islands, large modifications of the electronic properties are imposed by a different combination of growth parameters. To study these features experimentally, LT-STM spectroscopic measurements are powerful technique for addressing the individual electronic properties of such structures. There are few successful attempts addressing the electronic structures of islands locally, such as cross-section STM [167] and mainly LT-STM, where a spatially resolved wave-mapping was reported [168].

Preliminary results of LT-STS studies are presented in this section. Further improvement of the experimental set up needs to be carry out in order to achieve local probing of individual QDs.

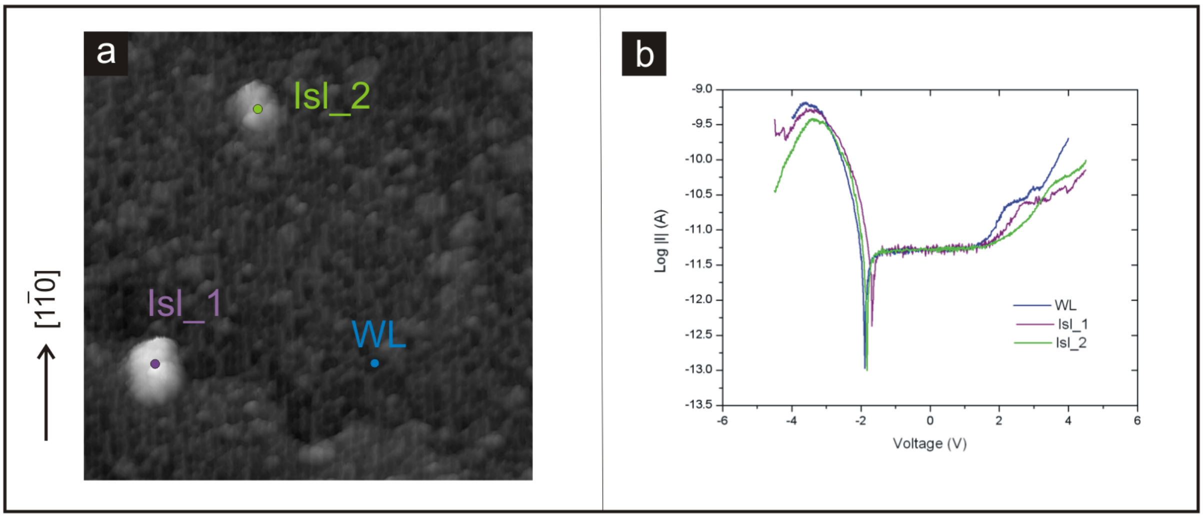

Fig. 6.1: On the left: STM image of an embryo and a precursor grown after the deposition of 1.75 ML of InAs/GaAs(001). Tunneling conditions: V_B = -3.5V and I = 0.3nA. On the right: Current vs voltage characteristics taken at 7K, for an embryo, a precursor and the WL. Stabilization parameters: V_B = -3 V and I = 0.3nA

Figure 6.1b shows I-V characteristics taken at low temperature ($\sim$ 7K) for an embryo, a precursor and on the WL, as shown on the STM image (Fig. 6.1a). For these small islands, there is no signature of confinement in the spectra and it can be seen Fig. 6.1b, the overlap of the wavefunctions of the islands and the wetting layer.

One of the problems encountered during the growth of the samples for the LT-STM was the control and calibration of the temperature during growth, due to the modification made on the Mo block (Fig. 2.9d). Similar results were found for other studied samples . Islands sizes were smaller than what expected for the growth conditions, we estimated that the real temperature during growth was significantly higher that that intended, affecting as well the islands composition.

Improvements in the design of the Mo block have been made and currently more LT-STS studies are being performed.

To a larger extend, QDs composition plays a fundamental role in the determination of the electronic properties of the QDs. Recently selective chemical etching has proven to be an effective tool to reveal the composition of the as-grown islands and QDs alike, for the Ge/Si(001) system [169]. In order to obtain complementary information, we have started etching experiments in order to investigate the composition profiles of buried InAs/GaAs(001) islands.

1.8 ML of InAs/GaAs (001) were deposited at 500^{o}C at a growth rate of 0.1 ML/s for growing mainly dome islands. Temperature was decreased to 460^{o}C to covered the surface with 15nm of GaAs, in order to reduce intermixing. Figure 6.2 presents a successful attempt to uncapped such a sample.

Figure 6.2a corresponds to an AFM image of the sample before the etching procedure. Using a 5:5:245 NH_4OH:H_2O42:H_2O solution at room temperature, the underlying islands are revealed. Surprisingly, the uncapped islands resemble very closely the just as grown dome islands. Islands' shape preservation was very recently observed for low-temperature (300^{o}C) capped islands for Ge/Si(001) system [170]. A rigorous and systematic analysis is currently under way, in order to disclosed effects of the capping deposition rates on the composition of the islands.

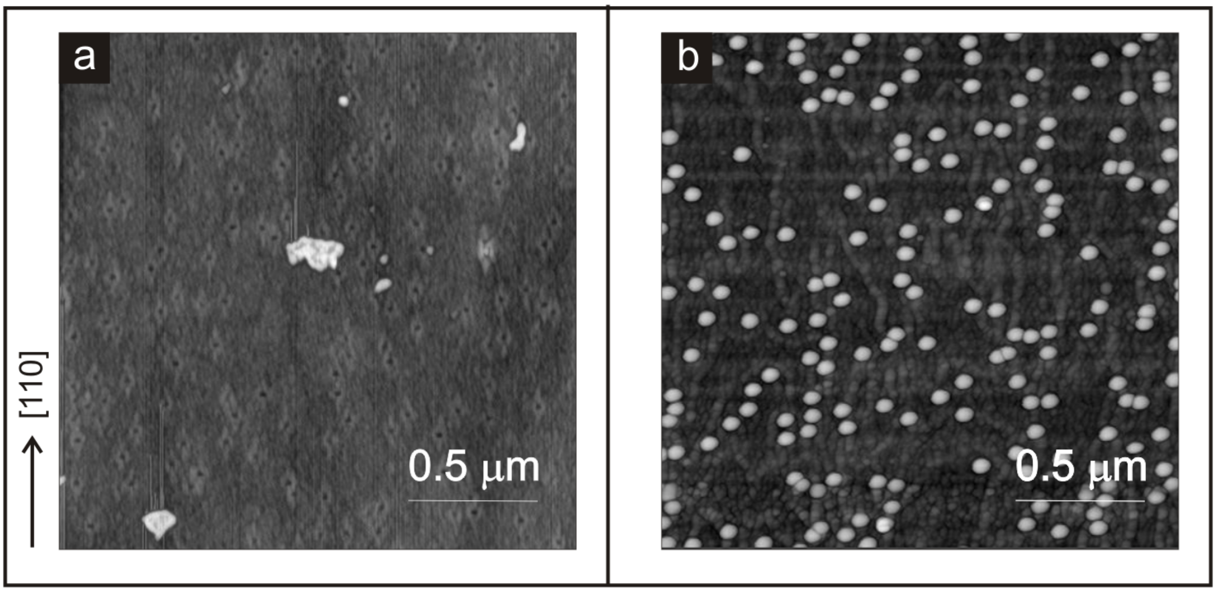

Fig. 6.2: On the left: AFM images of sample with a deposition of 1.8 ML of InAs at 500^{o}C, capped with 20nm of GaAs at 460^{o}C. On the right: an AFM images of the same sample after the capping layer was removed reveling the underlying islands.

We believe that together with the compositional determination of the islands, local spectroscopic studies will allow a complete description and understanding of the electronic properties of QDs. The hallmark and the most outstanding properties of these structures is the ability to confine carriers in all three dimensions. The ultimate goal is to find the correlation of the individual shape and composition with the confinement fingerprints allowing a full characterization of the most relevant QDs properties.

Appendix A

Facet Plot

The analysis of 3D images is one of the central issues in local probe studies. Nowadays, several algorithms have been put forward for obtaining information from STM images, among which stand the so-called Facet Plot analysis. In essence, this method offers a clear visualization of the surface by plotting the derivative of the surface height. In this appendix, a brief overview of this technique will be given.

In STM images, the surface morphology is usually displayed with grayscale, where each tone is used to depict a specific value of the surface height. In other words, the brighter an area in a STM image, the higher it is. Due to the inherent nature of each surface, its topography might consists of several facets with different slopes. Therefore, it seems intuitive to distinguish these facets by using a grayscale corresponding to the modulus of the surface gradient. For instance, if $z = f(x, y)$ represents the height of the surface's topography for each pixel located at (x, y), the modulus of the surface gradient is given by

$$\vec{g}(x,y) = \vec{\nabla} f(x,y) = \Big(\frac{\partial f}{\partial x}, \frac{\partial f}{\partial y}\Big) = -(\xi, \psi) \tag{A.1}$$

where (ξ, ψ) is a vector directed along the projection of the surface normal at (x, y) onto the (001) plane. In this representation, local surface orientation with steeper facets will appear darker than shallow facets, which will appear lighter, according to Eq. A.1.

By forming a 2D histogram with the aforementioned slopes or local surface orientations, quantitative information about the distribution of facets present on the surface can be obtained. This 2D histogram is called the Facet Plot (FP). As an example, let us consider the ideal case where N pixels are located at $(x_i, y_i)_{i=1,\ldots,N}$ in the topographical image and belonging to the same kind of facet F. These point will, in turn, have the same slope value $[-g(x_i, y_i) = (\xi_F, \psi_F)]$ and will give rise to a single bin with intensity N in the facet plot. However, in the real case F gives rise to a broadened spot centered at (ξ_S, ψ_S).

In this method for an ideal case, the facet's direction and its inclination in respect to the (001) plane ($\tan \alpha_F$ in the FP plane are given by the vector $\vec{v}$ with origin at $(0, 0)$ and tip at

(ξ_F, ψ_F) and its length (tan$\alpha_F = |\vec{v}| = (\xi_F^2 + \psi_F^2)^{1/2}$, respectively.

The facet's area is given by $A_F = N \times A_p/\cos\alpha_F$, where A_p is the area of a pixel in the STM image. As mentioned above, in the real case F corresponds to a broadened spot centered at (ξ_S, ψ_S). Here, the slope and orientation of the facet is measured by replacing (ξ_F, ψ_F) with (ξ_S, ψ_S), while the facet's area corresponds approximately to $A_F \approx A_p \sum_i (1/cos\alpha_i)$, where tan$\alpha_i = |-g(x_i, y_i)|$ and the sum extends to all pixels located in the broadened region center at (ξ_S, ψ_S).

For the sake of completeness, it is worth mentioning that one of the main drawback of the gradient-scheme representation is its inaccessibility to obtain information about the the height of the surface features. This limitation can be overcome through a linear combination of $f(x, y)$ and $g(x, y)$ in the following way

$$h(x, y) = af(x, y) + b|\vec{g}(x, y)| \tag{A.2}$$

Here, a and b satisfy a normalization condition in such a manner that $a + b = N_c$, where N_c corresponds to the number of gray tones used in the representation. Although h has no clear physical meaning, it can give a qualitative idea of the surface height and slopes of the different facets at the same time.

The versatility of this method also allows to study the wetting layer by enhancing its corrugation. This is done by limiting the grayscale in such a way that features higher than certain z_{max} appear white (index N_c) and those lower than certain z_{min} appears black (index 0). In other words, one has to define a function such that

$$\theta(z) = \begin{cases} N_c & \text{for } z \geq z_{max} \\ \frac{z - z_{min}}{z_{max} - z_{min}} & \text{for } z_{min} \leq z < z_{max} \\ 0 & \text{for } z < z_{min} \end{cases}$$

Nevertheless, this representation has a disadvantage since the islands will appear featureless. This problem can be solved by combining the representation described above with $|\vec{g}|$ or even with the laplacian (second derivative) of the surface $\nabla^2 f = \vec{\nabla}\vec{g}$. Thus, equation A.2 is generalized as follows:

$$h(x, y) = a\theta(f(x, y)) + b\theta(|\vec{g}(x, y)|) \tag{A.3}$$

where the second term enhances the island's facet.

Finally, in order to enhance edges and image contrast, one can replace the second term in Eq.A.3 by the laplacian as follows:

$$h(x, y) = a\theta(f(x, y)) + b\theta(\nabla^2 f(x, y)). \tag{A.4}$$

In the present work, we frequently make used of the negative local surface slope (LLS) for visualizing the characteristic facets composing an island(Eq. A.1). In some cases a combination of local surface height and local surface slope are made to enhanced minute features disguised by the height discrepancy between the islands.

To illustrate the difference between each representation, an AFM image of InGaAs quantum dots is display in different modes. The grayscale in Fig. A.1a, corresponds to the positive surface slope, edges and other small features can be appreciated relatively better than by using the local surface height as shown in Fig. A.1b. Fig. A.1c is represented using the negative local surface slope. Finally, in Fig. A.1 d and e, a combination of the surface height with and the positive (d) and negative surface slope (e) are shown for comparison.

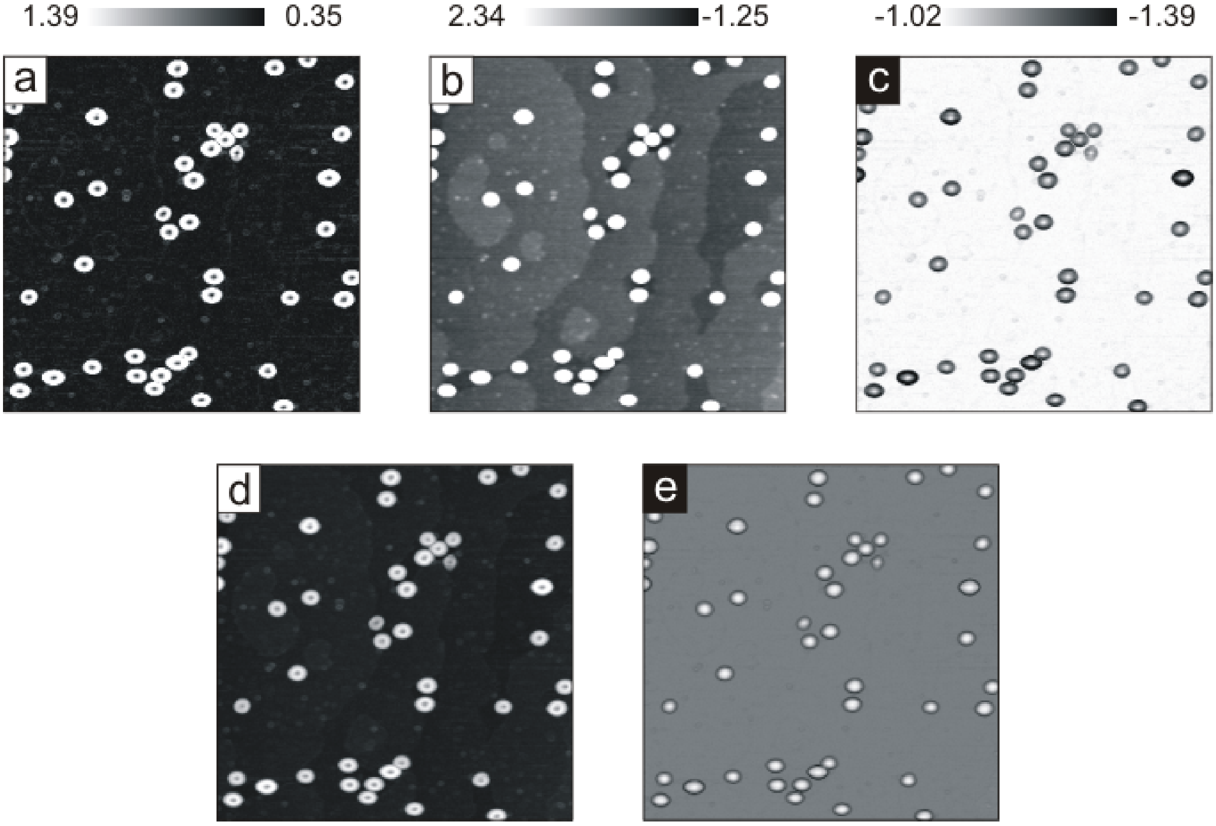

Fig. A.1: AFM images of InGaAs islands. Grayscale according to a) positive LSS, b) local surface height, c) negative LSS, d) a combination of surface height and the positive LSS and e) a combination of the surface height with the negative LSS. The vertical scales for the first three are given. All image size are 2μ m x 2 μm.

Bibliography

[1] X. Wang, L. Yang, Z. Chen, and D. M. Shin, CA Cancer J Clin **58**, 97 (2008).

[2] M. Goldberg, R. Langer, and X. Jia, Journal of Biomaterials Science. Polymer edition **18**, 241 (2007).

[3] *Introducing Molecular Electronics*, edited by G. Cuniberti, G.Fagas, and K.Richter (Springer, Berlin, 2005).

[4] B Kane, Cahiers de la Revue de théologie et de philosophie **393**, 133 (1998).

[5] G.M. Whitesides, Nature Biotechnology **21**, 1161 (2003).

[6] P. Fortina, L. J. Kricka, S. Surrey, and P. Grodzinski, Trends in biotechnology **23**, 168 (2005).

[7] V. Springel, S. D. M. White, A. Jenkins, C. S. Frenk, N. Yoshida, J. Navarro L. Gao, R. Thacker, D. Croton, J. Helly, J. Peacock, S. Cole, P. Thomas, A. Evrard H. Couchman, J. Colberg, and F. Pearce, Nature **435**, 629 (2005).

[8] N. Charvet, P. Reiss, A. Rogeta, A. Dupuisb, D. Grünwaldb, S. Carayona, F. Chandezona, and T. Livachea, Journal of Materials Chemistry **14**, 2638 (2004).

[9] Y. Rakovich, J.F. Donegan, S.A. Filonovich, M.J.M. Gomes, D.V. Talapin, A.L. Rogach, and A. Eychmuller, Physica. E, Low-dimensional systems and nanostructures **17**, 99 (2003).

[10] Y. Yin and A.P. Alivisatos, Nature **437**, 664 (2005).

[11] R. Hanson, L. P. Kouwenhoven, J. R. Petta, S. Tarucha, and L. M. K. Vandersypen, Reviews of Modern Physics **79**, 1217 (2007).

[12] D. Gammon, in *Optics of Quantum Dots and Wires*, edited by G. W. Bryant and G. S. Solomon (Artech House Publishers, Boston-London, 2005), Chap. 9, pp. 349–399.

[13] D. Bimberg, M. Grundmann, and N. N. Ledentsov, *Quantum Dot Heterostructures* (John Wiley Sons, Chichester, 1999).

[14] E. Voura, J.K. Jaiswal, H. Mattoussi, and S.M. Simon, Nature Medicine **10**, 993 (2004).

[15] J. Gao, W. Zhang, P. Huang, B. Zhang, X. Zhang, and B Xu, Journal of the American Chemical Society **130**, 3710 (2008).

[16] D. G. Deppe and D. L. Huffaker, Applied Physics Letters **77**, 3325 (2000).

[17] P. Michler, A. Kiraz, C. Becher, W. V. Schoenfeld, P. M. Petroff, L. Zhang, E. Hu, and A. Imamoglu, Science **290**, 2282 (2000).

[18] C. Y. Ngo, S. F. Yoon, C. Z. Tong, W. K. Loke, and S. J. Chua, Nanotechnology **18**, 365708 (2007).

[19] S.M. Sze, *Physics of Semiconductor Devices* (John Wiley Sons, Chichester, 1981).

[20] *Lateral Alignment of Epitaxial Quantum Dots*, edited by O.G. Schmidt (Srpinger, Heidelberg, 2007).

[21] http://www.lanl.gov/orgs/tt/index.shtml.

[22] *Introduction to Conventional Transmission Electron Microscopy*, edited by De Graed Marc (Cambridge University Press, Cambridge, 2003).

[23] E. H. Synge, Phil. Mag. **6**, 356 (1928).

[24] J. A. OKeefe, J. Opt. Soc. Am. **46**, 359 (1956).

[25] Russell Young, John Ward, and Fredric Scire, Review of Scientific Instruments **43**, 999 (1972).

[26] G. Binnig, H. Rohrer, Ch. Gerber, and E. Weibel, Phys. Rev. Lett. **50**, 120 (1983).

[27] G.Binnig and H.Rohrer, Angewandte Chemie International **26**, 606 (1987).

[28] J. P. McKelvey, *Solid State and Semiconductor Physics* (Harper and Row, New York, 1966).

[29] J. Sakurai, *Modern Quantum Mechanics* (Addison Wesley, Los Angeles, 1985).

[30] I. Brihuega, PhD dissertation, Universidad Autónoma de Madrid, 2003.

[31] C. Julian Chen, *Introduction to Scanning Tunneling Microscopy* (Oxford University Press, New York, 1993).

[32] J. Bardeen, Phys. Rev. Lett. **6**, 57 (1961).

[33] J. Tersoff and D.R. Hamann, Phys. Rev. B **31**, 805 (1984).

[34] A. Selloni, P. Carnevali, E. Tosatti, and C. D. Chen, Phys. Rev. B **31**, 2602 (1985).

[35] N. D. Lang, Phys. Rev. B **36**, 8173 (1987).

[36] J. K. Gimzewski and R. Möller, Phys. Rev. B **36**, 1284 (1987).

[37] Werner A. Hofer, Adam S. Foster, and Alexander L. Shluger, Progress in Surface Science **42**, 169 (1993).

[38] John G. Simmons, Journal of Applied Physics **34**, 1793 (1963).

[39] R. M. Feenstra, Joseph A. Stroscio, J. Tersoff, and A. P. Fein, Phys. Rev. Lett. **58**, 1192 (1987).

[40] J. Stroscio and R.M. Feenstra, in *Scanning Tunneling Microscopy*, edited by Joseph A. Strocio and William J. Kaiser (Academic Press, San Diego, 1993), Chap. 4, pp. 96–148.

[41] G. Binnig, C. F. Quate, and Ch. Gerber, Phys. Rev. Lett. **56**, 930 (1986).

[42] B. Cappella H. J. Butt and M. Kappl, Surface Science Reports **59**, 1 (2005).

[43] D. Sarid, *Scanning Force Microscopy*, *Oxford Series in Optical and Imaging Sciences* (Oxford University Press, New York, 1991).

[44] http://electron.mit.edu/∼gsteele/mirrors/elchem.kaist.ac.kr/jhkwak/TopometrixWeb/apmmi01.htm.

[45] http://www.physik.uni-regensburg.de/forschung/giessibl/fjg/index/index_d.shtml.

[46] T. Eguchi, Y. Fujikawa, K. Akiyama, T. An, M. Ono, T. Hashimoto, Y. Morikawa, K. Terakura, T. Sakurai, M. G. Lagally, and Y. Hasegawa, Phys. Rev. Lett. **93**, 266102 (2004).

[47] Yoshiaki Sugimoto, Pablo Pou, Masayuki Abe, Pavel Jelinek, Ruben Perez, Seizo Morita, and Oscar Custance, Nature **446**, 64 (2007).

[48] M.A. Herman and H. Sitter, *Molecular Beam Epitaxy*, Vol. 7 of *Springer Series in Materials Science* (Springer, Berlin, 1996).

[49] F. Patella, F. Arciprete, M. Fanfoni, V. Sessi, A. Balzarotti, and E. Placidi, Applied Physics Letters **87**, 252101 (2005).

[50] C. Manzano, PhD dissertation, thèse epfl, no 3002, Ecole Polytechnique Fédérale de Lausanne, 2004.

[51] M. Vogelgesang, PhD dissertation,thèse epfl, no 3352, Ecole Polytechnique Fédérale de Lausanne, 2005.

[52] S. Olthof, Bachelors dissertation, Universitaet Stuttgart, 2005.

[53] J. P. Ibe, P. P. Bey Jr., S. L. Brandow, R. A. Brizzolara, N. A. Burnham, D. P. DiLella, K. P. Lee, C. R. K. Marrian, and R. J. Colton, Journal of Vacuum Science and Technology A: Vacuum, Surfaces, and Films **8**, 3570 (1990).

[54] W. R. Ashby, Journal of General Psychology **37**, 125 (1947).

[55] J Barth, Annual Review of Physical Chemistry **58**, 375 (2007).

[56] C. Teichert, Physics Reports **365**, 335 (2002).

[57] P. Politi, G. Grenet, A. Marty, and J. Villain, Physics Reports **324**, 271 .

[58] Gert Ehrlich and F. G. Hudda, The Journal of Chemical Physics **44**, 1039 (1966).

[59] Richard L. Schwoebel and Edward J. Shipsey, Journal of Applied Physics **37**, 3682 (1966).

[60] H.Brune, C. Romainczyk, H. Röder, and K Kern, Nature **369**, 469 (1994).

[61] E.Bauer, Z. Kristallogr. **110**, 372 (1958).

[62] J. Behrend, M. Wassermeier, W. Braun, P. Krispin, and K. H. Ploog, Phys. Rev. B **53**, 9907 (1996).

[63] L. Goldstein, F. Glas, J. Y. Marzin, M. N. Charasse, and G. Le Roux, Applied Physics Letters **47**, 1099 (1985).

[64] O. Leifeld, A. Beyer, D. Grützmacher, and K. Kern, Phys. Rev. B **66**, 125312 (2002).

[65] J. Tersoff and F. K. LeGoues, Phys. Rev. Lett. **72**, 3570 (1994).

[66] Y. H. Xie, G. H. Gilmer, C. Roland, P. J. Silverman, S. K. Buratto, J. Y. Cheng, E. A. Fitzgerald, A. R. Kortan, S. Schuppler, M. A. Marcus, and P. H. Citrin, Phys. Rev. Lett. **73**, 3006 (1994).

[67] P. B. Joyce, T. J. Krzyzewski, G. R. Bell, and T. S. Jones, Applied Physics Letters **79**, 3615 (2001).

[68] S. Rousset, S. Chiang, D. E. Fowler, and D. D. Chambliss, Phys. Rev. Lett. **69**, 3200 (1992).

[69] J. Tersoff and R. M. Tromp, Phys. Rev. Lett. **70**, 2782 (1993).

[70] T. Hammerschmidt, PhD dissertation, Der Technischen Universität Berlin, 2006.

[71] K. Alchalabi, D. Zimin, G. Kostorz, and H. Zogg, Phys. Rev. Lett. **90**, 026104 (2003).

[72] F. Patella, A. Sgarlata, F. Arciprete, S. Nufris, P. D. Szkutnik, E. Placidi, M. Fanfoni, N. Motta, and A. Balzarotti, Journal of Physics Condensed Matter **16**, 1503 (2004).

[73] G. Costantini, C. Manzano, R. Songmuang, O. G. Schmidt, and K. Kern, Applied Physics Letters **82**, 3194 (2003).

[74] G. Costantini, A. Rastelli, C. Manzano, R. Songmuang, O. G. Schmidt, K. Kern, and H. von Känel, Applied Physics Letters **85**, 5673 (2004).

[75] Investigation of the Shape of InGaAs/GaAs Quantum Dots, Mat. Res. Soc. Symp. Proc. Vol. 737,2003, E13.40.1.

[76] S. Adachi, *Physical Properties of III-V Semiconductor Compounds: InP, InAs, GaAs, GaP, InGaAs, and InGaAsP* (Wiley-Interscience, Chichester, 1992).

[77] Bruce A. Joyce and Dimitri D. Vvedensky, Materials science and engineering. R, Reports **46**, 127 (2004).

[78] V. LaBella, H. Yang, D. Bullock, and P. Thibado, Phys. Rev. Lett. **83**, 2989 (1999).

[79] L. Daweritz and R. Hey, Surface Science **236**, 15 (1990).

[80] M. Takahasi, P. Kratzer, Penev E., and J. Mizuki, Surface Science **600**, 4099 (2006).

[81] A. Ohtake, P. Kocán, J. Nakamura, A. Natori, and N. Koguchi, Phys. Rev. Lett. **92**, 236105 (2004).

[82] E. Penev, P. Kratzer, and Scheffler M., Phys. Rev. Lett. **93**, 146102 (2004).

[83] P. Kratzer, E. Penev, and M. Scheffler, Applied Surface Science **216**, 436 (2003).

[84] O. Dehaese, X. Wallart, and F. Mollot, Applied Physics Letters **66**, 52 (1995).

[85] E. Penev, S. Stojković, P. Kratzer, and M. Scheffler, Phys. Rev. B **69**, 115335 (2004).

[86] M. C. Xu, Y. Temko, T. Suzuki, and K. Jacobi, Journal of Applied Physics **98**, 083525 (2005).

[87] J.G. Belk, C.F. Mcconville, J.L. Sudijono, T.S. Jones, and B.A. Joyce, Surface Science **387**, 213 (1997).

[88] M. Sauvage-Simkin, Y. Garreau, R. Pinchaux, M. B. Véron, J. P. Landesman, and J. Nagle, Phys. Rev. Lett. **75**, 3485 (1995).

[89] T. Kita, O. Wada, T. Nakayama, and M. Murayama, Phys. Rev. B **66**, 195312 (2002).

[90] M.C. Xu, Y. Temko, T. Suzuki, and K. Jacobi, Surface Science **580**, 30 (2005).

[91] J. M. Moison, C. Guille, F. Houzay, F. Barthe, and M. Van Rompay, Phys. Rev. B **40**, 6149 (1989).

[92] T Krzyzewski, P. B. Joyce, G.R. Bell, and T.S. Jones, Surface Science **517**, 8 (2002).

[93] O. Brandt, K. Ploog, L. Tapfer, M. Hohenstein, R. Bierwolf, and F. Phillipp, Phys. Rev. B **45**, 8443 (1992).

[94] A Ishii, Physica. E, Low-dimensional systems and nanostructures **21**, 578 (2004).

[95] K. Muraki, S. Fukatsu, Y. Shiraki, and R. Ito, Applied Physics Letters **61**, 557 (1992).

[96] J. M. García, J. P. Silveira, and F. Briones, Applied Physics Letters **77**, 409 (2000).

[97] A.G. Cullis, D.J. Norris, T. Walther, M.A. Migliorato, and M. Hopkinson, Phys. Rev. B **66**, 081305 (2002).

[98] T. Walther, A. G. Cullis, D. J. Norris, and M. Hopkinson, Phys. Rev. Lett. **86**, 2381 (2001).

[99] Y.Tu and J. Tersoff, Phys. Rev. Lett. **98**, 096103 (2007).

[100] S. Tsukamoto, T. Honma, G.ăR. Bell, A.Ishii, and Y. Arakawa, Small **2**, 386 (2006).

[101] M. Itoh, G. R. Bell, A. R. Avery, T. S. Jones, B. A. Joyce, and D. D. Vvedensky, Phys. Rev. Lett. **81**, 633 (1998).

[102] G. Costantini, A. Rastelli, C. Manzano, P. Acosta-Diaz, G. Katsaros, R. Songmuang, O.G. Schmidt, H. v. Kanel, and K. Kern, Journal of Crystal Growth **278**, 38 (2005).

[103] P. Kratzer, Q. K. K. Liu, P. Acosta-Diaz, C. Manzano, G. Costantini, R. Songmuang, A. Rastelli, O. G. Schmidt, and K. Kern, Phys. Rev. B **73**, 205347 (2006).

[104] R.Songmuang, S. Kiravittaya, and O.G. Schmidt, Journal of Crystal Growth **249**, 416 (March 2003).

[105] K. Jacobi, Progress in Surface Science **71**, 185 (2003).

[106] Y. Nakata, K. Mukai, M. Sugawara, K. Ohtsubo, H. Ishikawa, and N. Yokoyama, Journal of Crystal Growth **208**, 93 (2000).

[107] A. Madhukar, Q. Xie, P. Chen, and A. Konkar, Applied Physics Letters **64**, 2727 (1994).

[108] P. B. Joyce, T. J. Krzyzewski, G. R. Bell, T. S. Jones, S. Malik, D. Childs, and R. Murray, Phys. Rev. B **62**, 10891 (2000).

[109] V. A. Shchukin, T. P. Munt, D. E. Jesson, and D. Bimberg, Phys. Rev. B **71**, 113407 (2005).

[110] I. Daruka, J. Tersoff, and A.-L. Barabási, Phys. Rev. Lett. **82**, 2753 (1999).

[111] F. M. Ross, M. Kammler, M. C. Reuter, and R. Hull, Philosophical magazine **84**, 2687 (2004).

[112] I. Mukhametzhanov, Z. Wei, R. Heitz, and A. Madhukar, Applied Physics Letters **75**, 85 (1999).

[113] J. Marquez, L. Geelhaar, and K. Jacobi, Applied Physics Letters **78**, 2309 (2001).

[114] F. M. Ross, R. M. Tromp, and M. C. Reuter, Science **286**, 1931 (1999).

[115] F. Montalenti, P. Raiteri, D. B. Migas, H. von Kanel, A. Rastelli, and C. Manzano, Phys. Rev. Lett. **93**, 216102 (2004).

[116] Gilberto Medeiros-Ribeiro, Alexander M. Bratkovski, Theodore I. Kamins, Douglas A. A. Ohlberg, and R. Stanley Williams, Science **279**, 353 (1998).

[117] H. Saito, K. Nishi, and S. Sugou, Applied Physics Letters **74**, 1224 (1999).

[118] K. Zhang, C. Heyn, W. Hansen, T. Schmidt, and J. Falta, Applied Physics Letters **175**, 606 (2001).

[119] I. Mukhametzhanov, Z. Wei, R. Heitz, and A. Madhukar, Applied Physics Letters **75**, 85 (1999).

[120] G. Costantini, C. Manzano, R. Songmuang, O. G. Schmidt, and K. Kern, Applied Physics Letters **82**, 3194 (2003).

[121] Y. Hasegawa, H. Kiyama, Q. K. Xue, and T. Sakurai, Applied Physics Letters **72**, 2265 (1998).

[122] T. Kaizu and K. Yamaguchi, Jpn. J. Appl. Phys. **42**, 4166 (2003).

[123] P. Sutter, C. Schwarz, E. Muller, V. Zelezny, S. Goncalvesconto, and H. von Kanel, Applied Physics Letters **65**, 2220 (1994).

[124] A. Rastelli and H. von Kanel, Surface Science **515**, L493 (2002).

[125] S. Anders, C. S. Kim, B. Klein, M. W. Keller, R. P Mirin, and A. G. Norman, Phys. Rev. B **66**, 125309 (2002).

[126] T. J. Krzyzewski, P. B. Joyce, G. R. Bell, and T. S. Jones, Phys. Rev. B **66**, 121307 (2002).

[127] F. Montalenti, P. Raiteri, D. B. Migas, H. von Känel, A. Rastelli, C. Manzano, G. Costantini, U. Denker, O. G. Schmidt, K. Kern, and Leo Miglio, Phys. Rev. Lett. **93**, 216102 (2004).

[128] M. A. Lutz, R. M. Feenstra, P. M. Mooney, J. Tersoff, and J. O. Chu, Surface Science **316**, L1075 (1994).

[129] C. Priester and M. Lannoo, Phys. Rev. Lett. **75**, 93 (1995).

[130] N. Moll, M. Scheffler, and E. Pehlke, Phys. Rev. B **58**, 4566 (1998).

[131] E Pehlke, N Moll, A Kley, and M Scheffler, Applied Physics A, Materials science and processing **65**, 525 (1997).

[132] Q. K. K. Liu, N. Moll, M. Scheffler, and E. Pehlke, Phys. Rev. B **60**, 17008 (1999).

[133] L. G. Wang, P. Kratzer, N. Moll, and M. Scheffler, Phys. Rev. B **62**, 1897 (2000).

[134] E. Penev, P. Kratzer, and M. Scheffler, Phys. Rev. Lett. **93**, 146102 (2004).

[135] E. Penev, P. Kratzer, and M. Scheffler, unpublished .

[136] N. Moll, M. Scheffler, and E. Pehlke, Phys. Rev. B **58**, 4566 (1998).

[137] L. Geelhaar, J. Marquez, P. Kratzer, and K. Jacobi, Phys. Rev. Lett. **86**, 3815 (2001).

[138] D. B. Migas, S. Cereda, F. Montalenti, and L. Miglio, Surface Science **556**, 121 (2004).

[139] O. E. Shklyaev, M. J. Beck, M. Asta, M. J. Miksis, and P. W. Voorhees, Phys. Rev. Lett. **94**, 176102 (2005).

[140] G. H. Lu and F. Liu, Phys. Rev. Lett. **94**, 176103 (2005).

[141] G. H. Lu, M. Cuma, and F. Liu, Phys. Rev. B **72**, 125415 (2005).

[142] I. Daruka and J. Tersoff, Phys. Rev. B **66**, 132104 (2002).

[143] M. C. Xu, Y. Temko, T. Suzuki, and K. Jacobi, Journal of Applied Physics **98**, 083525 (2005).

[144] N. Liu, J. Tersoff, O. Baklenov, A. L. Holmes, and C. K. Shih, Phys. Rev. Lett. **84**, 334 (2000).

[145] D. M. Bruls, J. W. A. M. Vugs, P. M. Koenraad, H. W. M. Salemink, J. H. Wolter, M. Hopkinson, M. S. Skolnick, Fei Long, and S. P. A. Gill, Applied Physics Letters **81**, 1708 (2002).

[146] E. Placidi, F. Arciprete, V. Sessi, M. Fanfoni, F. Patella, and A. Balzarotti, Applied Physics Letters **86**, 241913 (2005).

[147] D. E. Jesson, G. Chen, K. M. Chen, and S. J. Pennycook, Phys. Rev. Lett. **80**, 5156 (1998).

[148] F. M. Ross, J. Tersoff, and R. M .Tromp, Phys. Rev. Lett. **80**, 984 (1999).

[149] A. Rastelli, M. Stoffel, J. Tersoff, G. S. Kar, and O. G. Schmidt, Phys. Rev. Lett. **95**, 026103 (2005).

[150] P. Sutter and M. G. Lagally, Phys. Rev. Lett. **81**, 3471 (1998).

[151] A. Rastelli, M. Kummer, and H. von Känel, Phys. Rev. Lett. **87**, 256101 (2001).

[152] J. M. Garca, G. Medeiros-Ribeiro, K. Schmidt, T. Ngo, J. L. Feng, A. Lorke, J. Kotthaus, and P. M. Petroff, Applied Physics Letters **71**, 2014 (1997).

[153] Q. Gong, P. Offermans, R. Nötzel, P. M. Koenraad, and J. H. Wolter, Applied Physics Letters **85**, 5697 (2004).

[154] Y. W. F. Ferdos, S. W., A. Larsson, M. Sadeghi, and Qingxiang Zhao, Applied Physics Letters **81**, 1195 (2002).

[155] G. Costantini, A. Rastelli, C. Manzano, P. Acosta-Diaz, R. Songmuang, G. Katsaros, O. G. Schmidt, and K. Kern, Phys. Rev. Lett. **96**, 226106 (2006).

[156] Ralf Blossey and Axel Lorke, Phys. Rev. E **65**, 021603 (2002).

[157] L.G. Wang, P. Kratzer, M. Scheffler, and Q.K.K. Liu, Applied Physics A: Materials Science and Processing **73**, 161 (2001).

[158] Qianghua Xie, P. Chen, and A. Madhukar, Applied Physics Letters **65**, 2051 (1994).

[159] B. Krause, T. H. Metzger, A. Rastelli, R. Songmuang, S. Kiravittaya, and O. G. Schmidt, Physical Review B **72**, 085339 (2005).

[160] G. Costantini, A. Rastelli, C. Manzano, P. Acosta-Diaz, G. Katsaros, R. Songmuang, O.G. Schmidt, H. v. Kanel, and K. Kern, Journal of Applied Physics **278**, 38 (2005).

[161] J. G. Belk, C. F. McConville, J. L. Sudijono, T. S. Jones, and B. A. Joyce, Surface Science **73**, 213 (1997).

[162] Zh. M. Wang, H. Churchill, C. E. George, and G. J. Salamo, Journal of Applied Physics **96**, 6908 (2004).

[163] I. Kegel, T. H. Metzger, A. Lorke, J. Peisl, J. Stangl, G. Bauer, K. Nordlund, W. V. Schoenfeld, and P. M. Petroff, Phys. Rev. B **63**, 035318 (2001).

[164] A. Lenz, R. Timm, H. Eisele, Ch. Hennig, S. K. Becker, R. L. Sellin, U. W. Pohl, D. Bimberg, and M. Dähne, Applied Physics Letters **81**, 5150 (2002).

[165] D. M. Bruls, J. W. A. M. Vugs, P. M. Koenraad, H. W. M. Salemink, J. H. Wolter, M. Hopkinson, M. S. Skolnick, Fei Long, and S. P. A. Gill, Applied Physics Letters **81**, 1708 (2002).

[166] Daniel Granados and Jorge M García, Applied Physics Letters **82**, 2401 (2003).

[167] B. Grandidier, Y. M. Niquet, B. Legrand, J. P. Nys, C. Priester, D. Stiévenard, J. M. Gérard, and V. Thierry-Mieg, Phys. Rev. Lett. **85**, 1068 (2000).

[168] Theophilos Maltezopoulos, Arne Bolz, Christian Meyer, Christian Heyn, Wolfgang Hansen, Markus Morgenstern, and Roland Wiesendanger, Phys. Rev. Lett. **91**, 196804 (2003).

[169] G. Katsaros, PhD dissertation, Univertität Konstanz, 200.

[170] G. Katsaros, M. Stoffel, A. Rastelli, O. G. Schmidt, K. Kern, and J. Tersoff, Applied Physics Letters **91**, 013112 (2007).

Publications

- G. Katsaros, J. Tersoff, M. Stoffel, A. Rastelli, P. Acosta-Diaz, G. S. Kar, G. Costantini, O. G. Schmidt, and K. Kern, *Positioning of strained islands by interaction with surface nanogrooves*", Phys. Rev. Lett. **101**, 096103 (2008).
- G.Costantini, A.Rastelli, C.Manzano, P.Acosta-Diaz, G.Katsaros, R.Songmuang, O.G.Schmidt, and K.Kern, "*Interplay between thermodynamics and kinetics in the capping of InAs/GaAs(001) quantum dots*", Phys. Rev. Lett. **96**, 226106 (2006).
- P.Kratzer, Q.K.K.Liu, P.Acosta-Diaz, C.Manzano, G.Costantini, R.Songmuang, A.Rastelli, O.G.Schmidt, and K.Kern, "*Shape Transition during Epitaxial Growth of InAs Quantum Dots on GaAs(001): Theory and Experiment*", Phys. Rev. B **73**, 205347 (2006).
- G. Costantini, R. Rastelli, C. Manzano, P. Acosta-Diaz, G. Katsaros, R. Songmuang, O.G. Schmidt, H. von Känel, and K. Kern, "*Pyramids and domes in the InAs/GaAs(001) and Ge/Si(001) systems*", Journal of Crystal Growth **278**, 38 (2005).

Acknowledgments

I'm delighted that at the end of this chapter of my life, I have so many people for so many different reasons to be thankful for. Now I know that it is good not needing anyone but is better to need someone and have so many reliable friends :D

First of all, my deepest appreciation to Prof. Dr. Klaus Kern, not only for welcoming me in his group but also for his guidance, advices and his enduring efforts to guide me always into the right track. It was my pleasure to be a member of your team.

To my direct supervisor, Dr. Giovanni Costantini for the good times we shared together. I always appreciated the freedom I had to speak my mind and I believe that the bad moments were a catalyst to transform a professional relationship into a friendship. For all your support muchas gracias jefe!

Thanks to Prof. Dr. Güter Schatz and Prof Dr. Peter Nielaba for the revision of this thesis and their participation in the jury.

To Dr. Lucia Vitali for being many times my non-official mentor. I'm deeply thankful for all the time you spent teaching me, for answering my multiples and never-ending questions and sometimes simply for listening to the frustrations of a PhD student. For your wit and disposition you always will be Luci-pedia for me.

To all the members of the MBE group for their assistance. Specially I thank Lijuan Wang and Armando Rastelli for providing me with the necessary samples for doing my work. I also thank Armando for his introduction to IDL and sharing willingly his experience.

To all Kern's group, especially Alpan Bek, Gero Wittich, Frank Stadler, Ignacio Paredes, Alicia Moroto, Eugenio Lunedei, Diego Repetto, Carlos Manzano, Michael Vogegelsang, Oguzhan Gürlü, Dietmar Payer, Axel Enders, Alexander Schneider, Nikola Malinowski, Sebastian Stepanow, Jens Bröttcher, Alexander Bittner, Ralf Vogegelsang, Wai Y. Lee and Laura

Valiente for making my stay in Stuttgart a pleasant stay and many good memories.

I'm deeply thankful to Frau King for all her assistance with the paperwork, specially with the visa issues and for always having such a good vibe around her.

I thank Sabine Birtel, for her kind disposition to assist me since the beginning until the very last moment and even when I'm not there anymore.

Thanks to Dr. Federico Rosei for the invitation to visit Elettra, it was a very refreshing experience. Thanks also to Dr. Ernesto Placidi for always answering my questions.

To Stephan Rauschenbach for his all his help and the German translation of the abstract.

To my beloved crew, Thomas Classen, Tilman Assmus, Ruben Esteban, Kannan Balasubramanian, Maximilan Assig, Ivan Brihuega, Jens Dorfmüller, Cristina Gomez-Navarro, Liza Herrera, Jan Honolka, Tetiana Kurkina, Robin Ohmann, Vivek Pachauri, Adarsh Sagar, Violetta Sessi, Ravi Shankar Sundaram, Takayuki Suzuki, Alexis Vlandas, for all their care, help, meals and fun we had together.

To Eduardo Lee for his diligence and good will, for all the tea breaks and long talks but mainly for being always such a good and dearest friend.

To Maggie Lingenfelder for her support not only inside the lab but also outside. I'm very grateful to you for giving me shelter during the very last days in Stuttgart but above all for your thoughtful friendship and help during my toughest moments.

To Giorgios Katsaros for sharing with me the darkest moments of our Lab work and for the twenty thousand 'moments of truth'. I will forever be in debt with you for your generosity and unconditional response when I needed you most. Thanks a lot Giorgios.

Special thanks to Ruth Jenz for her warmth and hospitality. I appreciated a lot finding always her door open when I needed it but I'm more thankful for finding always her heart open to me. Many thanks for the birthday cakes, the good wishes and the shared laughter.

To my dearest and beautiful friend Ulli Waizmann. I'm very grateful for her trust and affection. I cherish all our trips and rendezvous and all the great time we spent together. In your company not only we discovered nice places and tasted new flavors but we also discovered that

great hearts have no nationality.

I'm deeply thankful to Alicia Forment for her hearty support, I would have been lost with out her. You not only comforted and encouraged me but with you and in Pepe and Neus company I felt back at home. For having me in your house, for all the dinners, the jokes, the stress, the laughter and the tears, for enduring my bad moods and for loving me just as I am, many thanks. Gracias por todo compadres.

I've always being grateful for the full support and never-ending love of my family. You are my constant reminder of the true valuable things in life. Because of you, no matter where I am, the stars are always laughing. Dad this one is for you.

My deepest thanks go to Gerardo Gamez. We come a long way. Together we have grown and transformed and through it all you have always offered me your love and affection. At the end of this journey I realized that I could have made less mistakes, I could have walked safer paths, I could have listened more, I could have taken better choices but I couldn't have chosen a better companion and for that I'm truly grateful.